

Summer 2014

Micro and nano technology platforms: From cell viability monitoring to FET based biosensing

Pushparaj D. Pathak

Follow this and additional works at: <https://digitalcommons.latech.edu/dissertations>

 Part of the [Nanoscience and Nanotechnology Commons](#)

**MICRO AND NANO TECHNOLOGY PLATFORMS:
FROM CELL VIABILITY MONITORING
TO FET BASED BIOSENSING**

by

Pushparaj D. Pathak, B.E., M.S.

A Dissertation Presented in Partial Fulfillment
of the Requirements of the Degree
Doctor of Philosophy

COLLEGE OF ENGINEERING AND SCIENCE
LOUISIANA TECH UNIVERSITY

August 2014

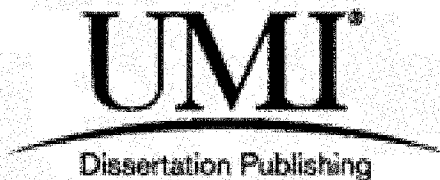
UMI Number: 3662467

All rights reserved

INFORMATION TO ALL USERS

The quality of this reproduction is dependent upon the quality of the copy submitted.

In the unlikely event that the author did not send a complete manuscript and there are missing pages, these will be noted. Also, if material had to be removed, a note will indicate the deletion.

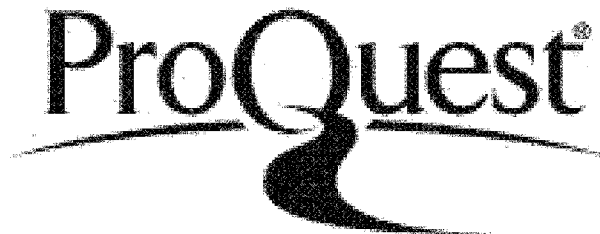


UMI 3662467

Published by ProQuest LLC 2015. Copyright in the Dissertation held by the Author.

Microform Edition © ProQuest LLC.

All rights reserved. This work is protected against unauthorized copying under Title 17, United States Code.



ProQuest LLC
789 East Eisenhower Parkway
P.O. Box 1346
Ann Arbor, MI 48106-1346

LOUISIANA TECH UNIVERSITY

THE GRADUATE SCHOOL

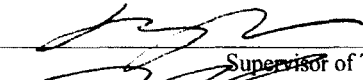
JANUARY 28, 2014


Date

We hereby recommend that the thesis prepared under our supervision
by PUSHPARAJ D. PATHAK, B.E., M.S.

entitled MICRO AND NANO TECHNOLOGY PLATFORMS:
FROM CELL VIABILITY MONITORING
TO FET BASED BIOSENSING

be accepted in partial fulfillment of the requirements for the Degree of
DOCTOR OF PHILOSOPHY IN ENGINEERING

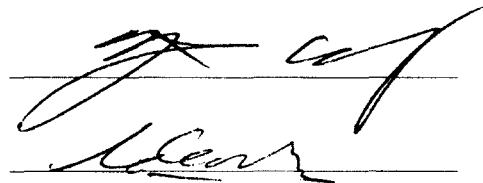


Supervisor of Thesis Research


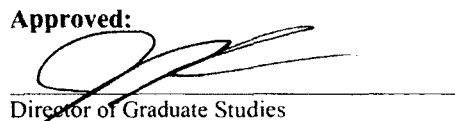
Head of Department
ENGINEERING
Department

Recommendation concurred in:
Yuri Lvov

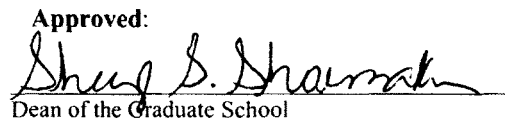
Sandra Zivanovic



Advisory Committee

Approved:


Director of Graduate Studies

Approved:


Dean of the Graduate School



Dean of the College

ABSTRACT

Nanotechnology is a multidisciplinary field that combines science and engineering to design, synthesize, characterize and explore applications for materials and devices whose smallest functional organization in at least one dimension is on the nanometer scale. Nanotechnology is undergoing an explosive development and the extent of potential application is vast and widely diverse. In the field of human health care, nanotechnology is helping to develop novel materials and structures, which have made it possible to miniaturize many of the tools used in conventional assays. Smart biochips constructed out of these novel materials and structures are now capable of performing limited *in vitro* diagnostic tests involved in immunoassays. In this work, we report two devices that make use of micro scale and/or nano scale structures to contribute to the ever-expanding use of biochips in human health care.

The first device is a Patch-Clamp microchip that is capable of monitoring cell viability in real-time. It is critical to monitor the health of cells in biological life science and medical research. Researchers must know if a new drug is capable of killing cancer cells or in other cases to determine the toxic effects of a drug or a pesticide on healthy cells. Conventional cell viability monitoring techniques that use flow cytometer or fluorescent dyes in conjunction with fluorescence microscope are time consuming and require sample labeling. Alternatively, we have designed a patch-clamp microchip, which allows one to measure the ion-channel currents in real-time. This microchip provides a

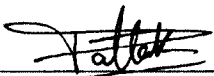
faster and label-free platform to monitor the health of the cell. Simultaneously, viability tests were performed on four different types of cancer cells (MB231, MB231-BR-vector, MB231-BR-HER 2, and MB231-BR) using the conventional fluorescent dye technique and using the patch-clamp microchip technique. For the patch-clamp technique, the seal resistance of the device decreased from $\sim 22 \text{ M}\Omega$ (living cell) to $\sim 4 \text{ M}\Omega$ (dead cell) over a period of 120 minutes. Comparing the seal resistance to the intensity of the fluorescence images over the 120 minute period confirms a correlation between the health of the cell and the ion-channel current, validating our claim that the patch-clamp microchip can be used as an alternate technical platform to the conventional techniques that use fluorescent dyes or a flow cytometer.

The second device is a Field-Effect Transistor (FET) based biosensor used for the detection of biomolecules. The conventional technique, ELISA, is still the gold standard for immunoassays. Most of the modern biosensors have exploited the semi conductive nature of CNT to design a label-free FET based immunosensor (biosensor that exclusively monitors the antibody-antigen interaction). Even though biosensors made out of a single CNT are ideally capable of detecting a single molecule, the fabrication of such devices is challenging. To avoid the fabrication complexity involved with a single CNT based immunosensor, we have developed an FET based biosensor, in which the channel is made out of Carbon Nanotube Thin Film (CNTF). The CNTF channel between the source and drain electrodes is assembled using electrostatic layer-by-layer (LBL) self-assembly. The bio-affinity interaction between Protein A and rabbit IgG is used to model the antibody-antigen interaction, and our initial results show the device is capable of detecting IgG concentrations as low as 1 pg/mL .

APPROVAL FOR SCHOLARLY DISSEMINATION

The author grants to the Prescott Memorial Library of Louisiana Tech University the right to reproduce, by appropriate methods, upon request, any or all portions of this Dissertation. It is understood that “proper request” consists of the agreement, on the part of the requesting party, that said reproduction is for his personal use and that subsequent reproduction will not occur without written approval of the author of this Dissertation. Further, any portions of the Dissertation used in books, papers, and other works must be appropriately referenced to this Dissertation.

Finally, the author of this Dissertation reserves the right to publish freely, in the literature, at any time, any or all portions of this Dissertation.

Author 

Date 05/11/2014

DEDICATION

To my dear parents, Dirgha Raj and Laxmi Devi Pathak, my sisters, Chanda Joshi and Sushila Pant, my brother Suryaprasad Pathak, and my beloved wife Devika.

TABLE OF CONTENTS

ABSTRACT.....	iii
DEDICATION.....	vi
LIST OF TABLES.....	xv
LIST OF FIGURES.....	xvi
ACKNOWLEDGMENTS.....	xx
CHAPTER 1 PATCH-CLAMP MICROCHIP: INTRODUCTION.....	1
1.1 Key Accomplishments of the Project.....	2
1.2 Outline of the Patch-clamp Microchip Project.....	3
CHAPTER 2 PATCH-CLAMP MICROCHIP: RESEARCH BACKGROUND.....	4
2.1 Ion-channels.....	4
2.2 Drug Discovery.....	7
2.2.1 Target Identification and Validation.....	7
2.2.2 Primary Screening.....	7
2.2.3 Secondary Screening.....	8
2.2.4 Safety Screening.....	8
2.2.5 Preclinical Testing.....	8
2.3 Ion-channel Assays.....	8
2.3.1 Patch-clamping.....	9
2.3.2 Fluorescence-based Methods.....	10
2.3.3 Flux Assays.....	10

2.3.4	Binding Assays	10
2.4	Patch-clamp Technique.....	10
2.4.1	Principle of Operation.....	11
2.4.2	Patch-clamp Configurations.....	13
2.4.2.1	Cell-attached Configuration	13
2.4.2.2	Inside-out Configuration.....	13
2.4.2.3	Whole-cell Configuration	14
2.4.2.4	Outside-out Configuration.....	14
2.4.2.5	Perforated Configuration	14
2.5	Planar Patch-clamp	15
2.6	Cell Viability and Cytotoxicity.....	18
CHAPTER 3 PATCH-CLAMP MICROCHIP: DESIGN, MATERIALS, AND EQUIPMENT NEEDED FOR FABRICATION		20
3.1	Patch-clamp Microchip Design	20
3.1.1	Input and Output Wells.....	21
3.1.2	Fluidic Channel Design.....	21
3.1.3	Air-bubble Actuators	21
3.1.4	Micropipette Design.....	22
3.1.5	Pipette Extension	23
3.2	Materials and Equipment.....	24
3.2.1	Materials used for Fabricating the Patch-clamp Microchip.....	24
3.2.1.1	Microscopic Glass Slide	24
3.2.1.2	Silicon Wafer.....	25
3.2.1.3	Ammonium Hydroxide.....	25
3.2.1.4	Hydrogen Peroxide	25
3.2.1.5	Polydimethylsiloxane (PDMS).....	25

3.2.1.6	PDMS Curing Agent	25
3.2.1.7	SU-8 2050.....	26
3.2.1.8	SU-8 Developer	26
3.2.1.9	Shipley S1813.....	26
3.2.1.10	LOR 7B.....	27
3.2.1.11	MF-319	27
3.2.1.12	Remover PG	27
3.2.2	Materials Needed for Monitoring Cell Viability	27
3.2.2.1	Calcein AM.....	27
3.2.2.2	Propidium Iodide	27
3.2.2.3	Cell Lines and Culture.....	27
3.2.3	Equipment Needed for Fabrication.....	28
3.2.3.1	Inductively Coupled Plasma Etcher	28
3.2.3.2	Oxygen Plasma Etcher.....	28
3.2.3.3	Hot Plate	28
3.2.3.4	Spin Coater	28
3.2.3.5	UV Light Source and Mask Aligner.....	28
3.2.3.6	E-beam Evaporator	29
3.2.3.7	Optical Microscope.....	29
3.2.4	Equipment Needed for Monitoring Cell Viability	29
3.2.4.1	Syringe Pump	29
3.2.4.2	Biopsy Punch.....	29
3.2.4.3	Tubes	29
3.2.4.4	Patch-clamp Amplifier	29
3.2.4.5	Digital Oscilloscope	29

3.2.4.6	Fluorescence Microscope	30
CHAPTER 4	PATCH-CLAMP MICROCHIP: FABRICATION.....	31
4.1	Mold Fabrication.....	31
4.1.1	Pipette Mold.....	31
4.1.2	Mold for Actuator Wells, Input and Output Wells, and Fluidic Channel.....	33
4.2	PDMS Replica	35
4.3	Air-Bubble Actuators.....	36
4.4	Binding PDMS Replica with the Air-Bubble Actuators.....	37
CHAPTER 5	PATCH-CLAMP MICROCHIP: EXPERIMENTAL SETUP AND PROTOCOL.....	38
5.1	Experimental Setup.....	38
5.2	Experiment Protocol	39
CHAPTER 6	PATCH-CLAMP MICROCHIP: RESULTS AND DISCUSSION	40
6.1	Ion-channel Current and Seal Resistance of Cell	40
6.2	Fluorescence Images of Cell.....	41
6.3	Comparing the Seal Resistance and Fluorescence Intensity.....	42
6.4	Summary	44
CHAPTER 7	PATCH-CLAMP MICROCHIP: CONCLUSIONS AND FUTURE WORK.....	45
7.1	Conclusions.....	45
7.2	Future Work.....	45
CHAPTER 8	FET BASED BIOSENSOR: INTRODUCTION.....	47
8.1	Key Accomplishments of the Project	48
8.2	Outline of FET Based Biosensor Project.....	49
CHAPTER 9	FET BASED BIOSENSOR: RESEARCH BACKGROUND.....	50
9.1	Diagnostic Targets	51

9.1.1	Nucleic Acids.....	52
9.1.2	Proteins	52
9.2	Biosensors.....	54
9.2.1	Optical Biosensors	56
9.2.2	Gravimetric Biosensors.....	58
9.2.3	Electrochemical Biosensors.....	58
9.2.3.1	Amperometric Electrochemical Biosensors	59
9.2.3.2	Potentiometric Electrochemical Biosensors	59
9.2.3.3	Impedimetric Electrochemical Biosensors	60
9.3	Nanotechnology and Biosensors.....	61
9.3.1	Nanoparticles	62
9.3.2	Nanowires	63
9.3.3	Carbon Derived Nanostructures.....	63
9.4	Carbon Nanotube	65
9.4.1	Structure of Carbon Nanotube	66
9.4.2	Electronic Structure of Carbon Nanotube.....	69
9.5	Carbon Nanotube Based Immunosensor.....	72
9.5.1	Field-Effect Transistor (FET) Based Immunosensor.....	73
9.5.2	Sensing Mechanism in SWCNT-FET Based Immunosensor	77
9.6	Protein Immobilization	80
9.6.1	Physical Immobilization	80
9.6.2	Covalent Immobilization	81
9.6.3	Bio-affinity Immobilization.....	82
9.7	Carbon Nanotube Thin Film.....	83
9.7.1	Fabrication of CNTF	84

9.7.1.1	Direct Growth.....	84
9.7.1.2	Solution-based Deposition.....	85
9.7.1.2.1	Stable CNT Dispersion	85
9.7.1.2.2	Coating Methods	86
9.7.2	Patterning Carbon Nanotube Thin Films	88
9.7.3	Electronic Properties of Carbon Nanotube Thin Films.....	89
9.8	Layer-by-Layer Self-Assembly	90
CHAPTER 10 FET BASED BIOSENSOR: DESIGN, MATERIALS, AND EQUIPMENT NEEDED FOR FABRICATION.....		92
10.1	Design	92
10.2	Materials	94
10.2.1	Materials Used for Fabrication	95
10.2.1.1	Silicon Wafers	95
10.2.1.2	Ammonium Hydroxide.....	95
10.2.1.3	Hydrogen Peroxide	95
10.2.1.4	Shipley S1813.....	95
10.2.1.5	LOR 3B.....	95
10.2.1.6	MF-319	96
10.2.1.7	Remover PG	96
10.2.1.8	Nitric Acid	96
10.2.1.9	Sulphuric Acid.....	96
10.2.1.10	Membrane Filter	96
10.2.1.11	SWCNTs Dispersion in DI Water	96
10.2.1.12	Poly (diallyldimethyl ammonium chloride) solution	97
10.2.1.13	Poly (sodium 4-styrenesulfonate).....	98
10.2.1.14	Sodium Chloride	98

10.2.1.15	Other Chemicals.....	98
10.2.2	Materials Needed for Biomolecule Detection.....	98
10.2.2.1	1-Ethyl-3-[3-dimethylaminopropyl]carbodiimide hydrochloride (EDC).....	98
10.2.2.2	Protein A.....	99
10.2.2.3	Immunoglobulin G (IgG).....	99
10.2.2.4	Sea Block.....	100
10.3	Equipment.....	100
10.3.1	Equipment Needed for Fabrication.....	100
10.3.1.1	Hot Plate.....	100
10.3.1.2	Spin Coater.....	100
10.3.1.3	UV Light Source and Mask Aligner.....	100
10.3.1.4	E-beam Evaporator.....	100
10.3.1.5	Optical Microscope.....	100
10.3.1.6	Vacuum Pump.....	100
10.3.1.7	Ultra-sonic Agitator.....	101
10.3.2	Equipment Needed for Characterization and Protein Detection.....	101
10.3.3	Other Equipment.....	101
CHAPTER 11	FET BASED BIOSENSOR: FABRICATION.....	102
11.1	Fabricating the Source and Drain Contact Electrodes.....	102
11.2	Fabricating the Gate Electrode.....	104
11.3	Fabricating the Channel.....	105
11.4	Passivizing the Source and Drain Contacts.....	110
CHAPTER 12	FET BASED BIOSENSOR: EXPERIMENTAL PROTOCOL, RESULTS AND DISCUSSION.....	113
12.1	Performance of the Device as an FET.....	113

12.2	Experiment Protocol	115
12.3	Performance of the Device as a Biosensor	117
CHAPTER 13 FET BASED BIOSENSOR: CONCLUSIONS AND FUTURE WORK		120
13.1	Conclusions.....	120
13.2	Future Work.....	120
REFERENCES		121

LIST OF TABLES

Table 9-1: Commonly available functional groups in proteins and functional groups required on the substrate surface.	81
--	----

LIST OF FIGURES

Figure 2-1: Structure of a Eukaryotic cell [13].	4
Figure 2-2: Cell membrane with an Ion-Channel [4].	5
Figure 2-3: Types of ion-channel gating mechanisms [16].	6
Figure 2-4: Simple patch-clamp configuration [21].	9
Figure 2-5: Electrical model of a cell. The sodium, calcium and potassium ion-channels are modeled as a variable conductance depending upon whether they are open or closed. The cell membrane is modeled as a capacitor; the reverse potential of each channel is modeled as a voltage source.	12
Figure 2-6: Patch-clamp configurations [28].	15
Figure 2-7: Basic structure of a planar patch-clamp device. A) Top view of the planar aperture on a glass chip. B) Cells are suspended and then suction is applied. C) A cell forming a seal with the aperture [27], [33].	17
Figure 3-1: Schematic of the patch-clamp device used. The chip has actuators for selecting and positioning the cells.	20
Figure 3-2: Close-up view of the cell sorting and positioning actuators [40].	21
Figure 3-3: Cell sorting mechanism. A) The target cell and the target direction is identified B) Applying a voltage pulse to the actuator on the left, deflects the cell into the target direction [40].	22
Figure 3-4: Schematic top-view of the device showing the position of the micropipette.	23
Figure 3-5: 3D model of the device showing the close up view of the micropipette. The length, width, and height of the micropipette are 15 μm , 3 μm , and 3 μm , respectively. The height of the fluidic channel is 50 μm .	24
Figure 4-1: Process flow for fabricating the pipette mold on the silicon wafer.	33

Figure 4-2: Process flow showing the pattern generated in the plane containing the cross-section of the pipette extension and the fluidic channel.....	34
Figure 4-3: 3D model of the SU-8 mold. The mold for input and output well, fluidic channel, air-bubble actuators, and Ag/AgCl electrode is made out of SU-8 (red color). The mold for the micropipette is made out of silicon (blue color).....	35
Figure 4-4: Process flow for fabricating the air-bubble actuators.	37
Figure 5-1: Fabricated microchip with assembled Ag/AgCl electrodes and tube connection at input well for cell flow.	39
Figure 6-1: Close up view of captured cell [12].	41
Figure 6-2: Current through the device over the test period. The current is in response to a 20 mV, 40 Hz square wave pulse [12].	41
Figure 6-3: Fluorescence images of the cell, the green fluorescence is due to Calcein AM and red fluorescence is due to PI [12].	42
Figure 6-4: Representative measured seal resistance of the captured cell and corresponding PI fluorescence intensity. Inset at $T = 0$ is the PI fluorescence image of the live cell (immediately after capture) and inset at $T = 120$ minutes is the PI fluorescence image of the dead cell [12].	43
Figure 6-5: Summary of seal resistance change for four cell lines, a change in the seal resistance shows similar trend. a) cell line 1 MB231; b) cell line 2 MB231-BR-vector; c) cell line 3 MB231-BR-HER 2; d) cell line 4 MB231-BR [12].	44
Figure 9-1: Areas of interest for pathogen detection [48].	51
Figure 9-2: Basic block diagram of a biosensor [55].	55
Figure 9-3: An interdigitated electrode (IDE) array.	61
Figure 9-4: A buckyball structure with carbon atoms at every vertex of an imagined soccer ball. The red lines indicate single bond and yellow lines indicate double bond [102].	65
Figure 9-5: The basic cylindrical structure of a carbon nanotube with both ends closed by semi-hemispherical buckyball [103].	67
Figure 9-6: A carbon nanotube formed by rolling a sheet of graphene. The chiral angle is denoted by θ , a_1 and a_2 are the graphene unit vectors [103].	68

Figure 9-7: Arrangement of carbon atoms in armchair carbon nanotube (left) and zigzag carbon nanotube (right) [104].....	69
Figure 9-8: Possible vectors for chiral nanotubes. Circled dots and dots represent metallic and semiconducting nanotube respectively [103].....	70
Figure 9-9: Density of states for a) zigzag nanotube (10, 0) and b) zigzag nanotube (9, 0). The dotted line shows density of states of 2D graphite [103].....	71
Figure 9-10: Construction of a) conventional MOSFET and b) ISFET proposed by Bergveld [113].....	74
Figure 9-11: a) AFM image of single CNT on top of three Pt electrodes b) schematic side view of the transistor [115].....	75
Figure 9-12: a) Output characteristic and b) transfer characteristic of SWCNT-FET [117].	76
Figure 9-13: Formation of Schottky barrier at metal-semiconductor junction for zero bias [124].....	77
Figure 9-14: The black curve corresponds to device characteristic before protein adsorption and the red curve corresponds to the device characteristic after protein adsorption a) electrostatic gating effect b) Schottky barrier effect [132].	78
Figure 9-15: Schematic representation of electrical double-layer and the antibody adsorbed on the interface [137].....	80
Figure 9-16: Structure of IgG where 1) Fab region, 2) Fc region, 3) heavy chain, 4) light chain, 5) antigen binding sites, 6) hinge regions [140].....	82
Figure 9-17: Schematic representation of electrostatic LBL assembly.	91
Figure 10-1: a) Schematic top view of type I device, blue circle highlights the channel region b) zoom-in view of the channel region highlighted by blue circle c) schematic top view of type II device. The CNTF in the channel is not shown here.	93
Figure 10-2: a) Schematic cross-sectional view of type I device and b) schematic cross-sectional view of type II device. The type I device has three electrodes: source, drain, and gate, while the type II device has only the source and drain electrodes.	94
Figure 10-3: Functionalized SWCNT with carboxyl group [173].....	97
Figure 10-4: Structural formula for PDDA [184].....	97

Figure 10-5: Structural formula for PSS [185].	98
Figure 10-6: Structure of IgG where 1) Fab region, 2) Fc region, 3) heavy chain, 4) light chain, 5) antigen binding sites, 6) hinge regions [140].	99
Figure 11-1: Process flow to fabricate source and drain contacts for type I and type II devices.	103
Figure 11-2: Process flow to assemble the channel in between the source and drain for type II device.	106
Figure 11-3: a) Optical micrograph of type II device before LBL assembly and b) optical image of type II device after LBL assembly. The channel length is 100 μm , the width is 150 μm and the channel overlap on the source and drain electrode is 20 μm , and the source and drain electrodes are made of Au. c) Optical image of type I device after LBL assembly, the source and drain electrodes are made of Au while the gate electrode is made of Al.	109
Figure 11-4: SEM image of the CNTF; the CNTF has 10 layers.	109
Figure 11-5: a) Schematic cross-sectional view of a passivized type II device b) optical top view image of actual fabricated device (bottom) showing the passivized contacts and a window in the middle exposing the microwire channel only.	111
Figure 11-6: a) Picture on the top shows an individual device. The size is $\sim 2\text{ cm} \times \sim 2\text{ cm}$ b) the device with a fluidic channel and tube connection to facilitate IgG flow.	112
Figure 12-1: a) Output characteristic b) transfer characteristic of type I device for drain to source voltage, $V_{ds} = 4\text{V}$. The device gate length is 100 μm and gate width is 100 μm .	114
Figure 12-2: Schematic representation of the protocol a) after Protein A immobilization on CNTF surface b) after blocking unoccupied spaces with sea block c) specific bio-affinity interaction between Protein A and IgG.	117
Figure 12-3: Drain current variation in response to various IgG concentrations.	118
Figure 12-4: Average drain current values for different concentrations of IgG (three devices were used during the experiment).	119

ACKNOWLEDGMENTS

I would like to express my sincere gratitude to my advisor, Dr. Long Que, for giving me an opportunity to work on these projects. He has been a great mentor throughout my doctoral study and has trained me to be capable of doing independent research. The knowledge and personal experiences he has shared are invaluable and have helped me to stay motivated during some tough times while in graduate school.

I would also like to thank the members for my advisory committee, Dr. Adarsh D. Radadia, Dr. Shengnian Wang, Dr. Sandra Zivanovic, and Dr. Yuri Lvov for their valuable advice during the course of the entire research.

I am also grateful to my colleagues Dr. Zhongcheng Gong, Dr. Tianhua Zhang, Mr. Siva Prasad Raju, Mr. Sukrut Karandhikar, Mr. Yuan He, Mr. Shashi Yadav, Mr. Yi-Hsuan Tseng, Mr. Xiang Li, and my friends at IfM Mr. Anupam Joshi, Mr. Gaurav Parekh, Mr. William Clower, and Dr. Praveen Pattekari for their support and useful advice.

It was a pleasure knowing the hardworking and very helpful staff members at IfM, and I would like to thank Ms. Debbie Wood, Mr. Ji Fang, Mr. Alfred Gunasekaran, and Mr. Donald Tatum.

I have been blessed to have a wonderful family who has always been supportive and a source of inspiration to me. I would like to thank my parents, and my brother and sisters who stood behind me and kept their faith in my abilities, my friends, relatives and

well-wishers. Finally, I would like to thank my beloved wife for being patient and offering unyielding support while I have worked toward obtaining my degree.

CHAPTER 1

PATCH-CLAMP MICROCHIP: INTRODUCTION

In biological life science and medical research, it is critical to distinguish between living and dead cells. Specifically, it is important to know if a potential cancer treatment drug has killed the cancerous cells. In order to monitor the cells' viability, the colorimetric or fluorescence technique is usually used [1]–[3]. Typically, these methods require a flow cytometer or the labeling of cells with fluorescent dyes in conjunction with using a fluorescence microscope to evaluate viability, making them time-inefficient and/or cost-ineffective. In addition, these techniques are not convenient for studying the dynamic process of cell death in real-time. For instance, the fluorescence images of the cells have to be processed with image processing tools, which can sometimes render the real-time monitoring unfeasible.

Recently, a technique measuring volume changes in single cells using a microfluidic chip has shown great promise for real time monitoring of treatment drug on the cells' viability [4]–[6]. This type of biosensor utilizes an electrical impedance method to monitor the volume change of a cell. Specifically, the cells to be measured are sent through a micro-chamber via a microfluidic network. When their volumes change, the extra-cellular fluid in the micro-chamber will be pushed out. As a result, the electrical resistance of the chamber will change. Using this microfluidic chip, high throughput drug

screening can be achieved. Therefore, a tagless technique, which offers instantaneous and quantitative information about cell viability, becomes very attractive.

Traditional PC technology is very time consuming and requires laborious effort with a rather low throughput. For the past decade, various types of PC microchips have been developed in several groups to enhance the throughput and efficiency over the conventional glass-pipette based PC technology [7]–[11]. It has been demonstrated that by using a properly designed and fabricated micropipette, some PC microchips show reliable and consistent Gigaseal (resistance in the range of giga ohms) capability, indicating the possibility that the PC microchip can eventually replace the conventional glass-pipette PC technology.

In this work, we offer an alternate viable technical platform for monitoring cell viability in real time using a planar patch-clamp microchip [12] .

1.1 Key Accomplishments of the Project

The significant accomplishments of this project include fabrication of the planar patch-clamp microchip, successful recording of ion-channel currents in four different types of human breast cancer cells including MDA-MB231, MDA- MB231-brain metastatic subline (abbreviated as MB231-BR), MB231-BR over-expressing HER2 gene (MB231-BR-HER2), and MB231-BR-vector control for the HER2 (MB231-BR-vector), and simultaneously validating the results against the change in cell fluorescence intensity to prove the viability of the patch-clamp microchip technical platform. It has been demonstrated that, even though the seal resistance of the PC microchip is in the range of Mega-ohms ($M\Omega$), it is still able to monitor cell viability.

1.2 Outline of the Patch-clamp Microchip Project

In CHAPTER 2 we begin with a discussion on ion-channels, the gating mechanisms in ion-channels, the ion-channel assays and use of patch-clamp technique in these assays. We then explain the basic construction of a patch-clamp device and the various configurations it can be employed. The chapter ends with a discussion on the planar patch-clamp structure, its significance, cell viability and how the planar patch-clamp structure can be used as a technical platform to monitor cell viability.

In CHAPTER 3 we discuss the various components of the microchip. The design aspect of each component including the micropipette, which is the most vital part of the microchip, is explained with different schematics. The chapter concludes with a mention of the various materials and equipment that are required to fabricate the microchip.

A detailed fabrication process for each component of the microchip is discussed in CHAPTER 4.

CHAPTER 5 discusses the build up to the real-time viability monitoring experiments by introducing the experimental setup and the protocol used.

In CHAPTER 6 we discuss the performance of the patch-clamp microchip. The ion-channel currents for 12 cells from 4 different cell lines are recorded over a period of time and simultaneously fluorescence images of the cell are also recorded. The validity of the patch-clamp microchip as a viable technical platform for real-time monitoring of cell viability is discussed after comparing the change in seal resistance and the change in intensity of the fluorescence images.

In CHAPTER 7 we summarize the patch-clamp microchip project and discuss its future direction.

CHAPTER 2

PATCH-CLAMP MICROCHIP: RESEARCH BACKGROUND

2.1 Ion-channels

The structure of a Eukaryotic cell is shown in Figure 2-1. The external membrane of the cell, called the plasma membrane or cell membrane, plays a crucial role in maintaining the balance between the intracellular and extracellular environment.

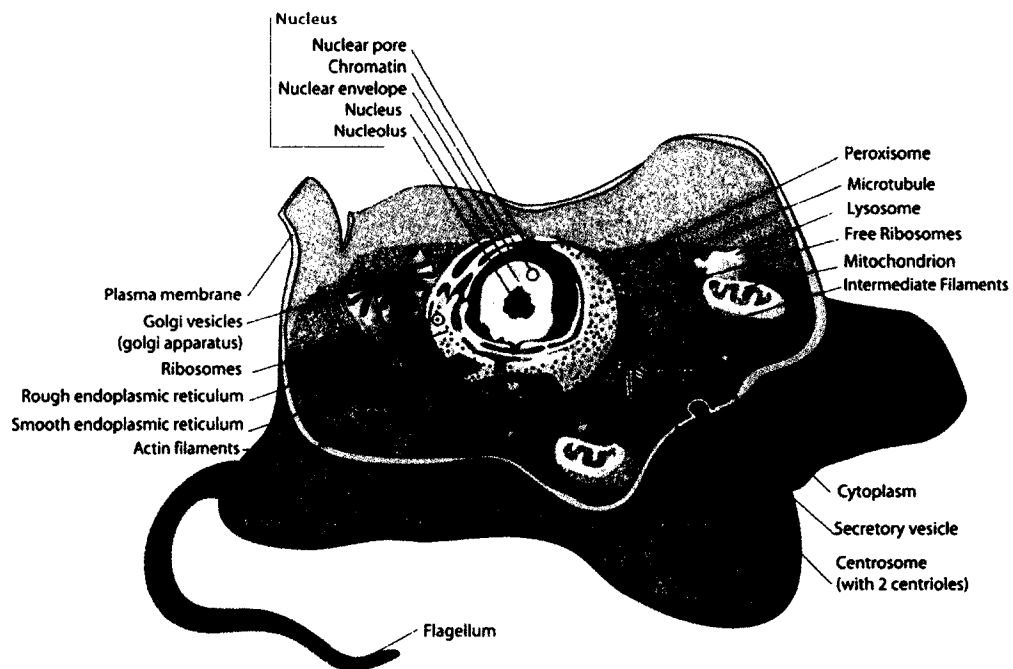


Figure 2-1: Structure of a Eukaryotic cell [13].

The cell membrane is made up of phospholipids and protein molecules, which are held together by non-covalent interactions. Specialized trans membrane proteins create pore like structures on the membrane called ion-channels as shown in Figure 2-2.

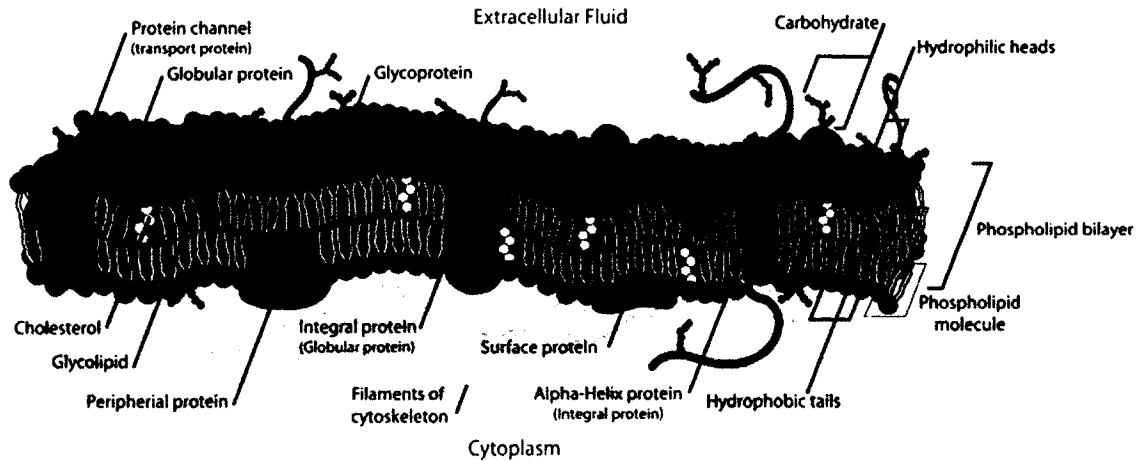


Figure 2-2: Cell membrane with an Ion-Channel [4].

Gating is the process of opening and closing the ion channel; this process facilitates the transport of ions like Na^+ , K^+ , Ca^+ or Cl^- between the cell and the surrounding environment. In 1952, Hodgkin and Huxley established that the movement of Na^+ and K^+ in a giant nerve fiber contributed to ionic currents [14]. Hodgkin and Huxley also established that there were independent ionic pathways for Na^+ and K^+ flow. The definite existence of ion-channels was only demonstrated later, in 1972, by Hladky and Hayden [15]. Hladky and Hayden studied the change in conductance induced by an antibiotic gramicidin A. They also observed these channels were permeable to univalent cations, but completely impermeable to polyvalent anions and cations.

Ion-channels are classified depending on the type of ion they transport. The prominent channels are sodium channels, potassium channels, calcium channel, and chloride channels. The ion-channels open and close in response to a stimulus, the

stimulus could be a change in membrane potential or binding of a ligand (chemical messenger). Depending on the stimulus, ion-channels can be classified into three broad categories: voltage-gated channels, extracellular ligand-gated and intracellular ligand-gated as shown in Figure 2-3. The difference in ion concentration between the intracellular medium (cytoplasm) and the extracellular medium builds up a potential across the cell membrane; this is called the resting membrane potential. Voltage-gated channels conduct when there is a change in the membrane potential. Extracellular ligand-gated channels conduct in response to ligand molecules binding to the extracellular domain. Intracellular ligand-gate channels conduct in response to ligand molecules binding to the intercellular domain.

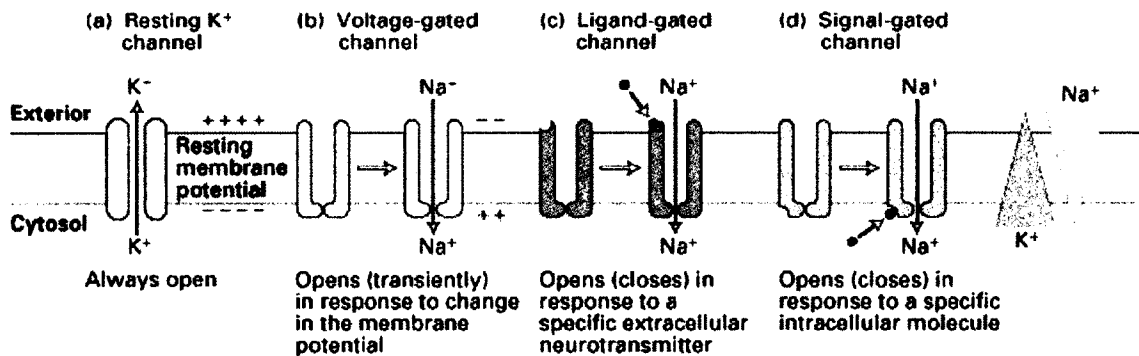


Figure 2-3: Types of ion-channel gating mechanisms [16].

Many diseases have been linked to ion-channels [17]. These diseases are usually caused due to the mutation of genes in the ion-channels. Research has shown that mutations in voltage gated Ca²⁺ channel genes result in migraine headache and some forms of epilepsy, while others like long QT syndrome are caused due to the mutation of genes in either Na⁺ or K⁺ channels. Many of these inherited ion channel diseases caused

due to mutation in Na^+ , K^+ , Ca^{2+} and Cl^- channels are collectively called *channelopathies* [18].

2.2 Drug Discovery

The process of identifying a chemical compound (drug) that has a therapeutic effect is tedious and complicated. To find the cure to a disease, it is important first to understand the disease and the conditions that cause it. Understanding the disease involves understanding how the genes are affected, how the genes affect the proteins they encode, how those proteins interact with each other in living cells, how those affected cells change the specific tissue they are in, and finally how the disease affects the entire patient's health. Modern drug-discovery chain can be divided into five basic segments. They are: target identification and validation, primary screening, secondary screening, safety screening, and preclinical testing [19].

2.2.1 Target Identification and Validation

Once the underlying cause of the disease is understood, a *target* is selected. The target is a single molecule, either a gene or a protein, which is involved in the disease. The selection is such that the target can potentially interact and be affected by a drug molecule. It is important to validate the relevance of the target to the disease. It is possible that the target shows a lot of promise to begin with, but it could eventually lead to a dead end.

2.2.2 Primary Screening

There are thousands of molecules known to pharmaceutical companies today. Primary screening involves exposing the target to different molecules. A specific modulation is expected to occur in the target upon exposure to these molecules. The

screening data is then examined to find the molecules that cause the desired modulation; these molecules are identified as *lead compounds*.

2.2.3 Secondary Screening

Primary screening helps construct focused libraries, which are then optimized during the secondary screening. For example, the structure of a molecule can be changed in a way such that it does not react with any other chemical pathways in the body, thus reducing the potential for side effects.

2.2.4 Safety Screening

Every lead compound is tested for safety. These tests target the pharmacokinetics, or absorption, distribution, metabolism, excretion, and toxicological properties of the lead.

2.2.5 Preclinical Testing

This stage involves a large number of *in vitro* and *in vivo* tests to narrow down the *candidate drugs*, which will be studied in the clinical trials. *In vitro* tests are conducted in the lab and carried out in beakers and test tubes. *In vivo* tests are conducted on animal models and living cells. The data from these tests shows the efficacy of the drug and its safety profile.

2.3 Ion-channel Assays

The process to find candidate drugs that can cure an ion-channel related disease is the same as discussed in Section 1.2. There are several types of popular standard ion-channel assay technologies, and new emerging technologies have been reported every year. The most popular ion-channel assay technologies are: Patch-clamping, Fluorescence-based methods, Flux assays, and Binding assays [20].

2.3.1 Patch-clamping

The patch-clamp technique involves placing a pipette (tip of the pipette is a few microns in diameter) with electrolytic solution against the cell membrane of a living cell and applying a small amount of suction. This suction forms a tight electrical seal between the cell membrane and the pipette usually in the order of giga-ohms. An Ag/AgCl electrode is then inserted into the pipette such that it makes contact with the electrolyte in the pipette. The ionic current between the electrolyte and the cell is sensed by this electrode. The ionic current between the electrolyte and the cell is sensed by this electrode and fed to an amplifier, which analyzes the conductance and kinetics associated with the ion-channels. A simple patch-clamp configuration is shown in Figure 2-4. The patch-clamp technique proves to be a great tool with high potential in the research of neuroscience and electrophysiology for its ability to measure functions directly like gating, permeability, voltage sensing, and selectivity of ion-channels.

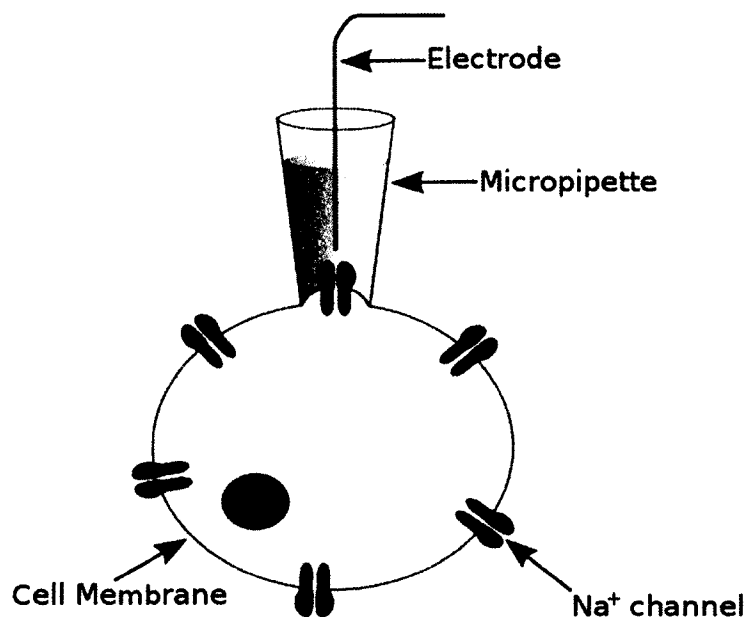


Figure 2-4: Simple patch-clamp configuration [21]

2.3.2 Fluorescence-based Methods

These techniques involve loading fluorescent dyes into the cytosol or cell membrane. The flow of ions between the intracellular and extracellular medium can lead to a change in the membrane potential or can change the ion concentration in one of the mediums. The fluorescent dye loaded in the cell membrane is sensitive to these changes and, instead of measuring the ionic current directly, the change in fluorescence signals is measured. Optical techniques like total internal reflection fluorescence (TIRF) have been used to measure single-channel Ca^{2+} flux [22].

2.3.3 Flux Assays

This assay involves utilizing radioactive isotopes to trace the cellular influx or efflux of specific ions. The cells that contain the ion-channel of interest are incubated in a buffer containing radioactive isotopes for several hours and then washed. The cells are then incubated in a solution of agonist; this allows the efflux of the isotope. Finally, the radioactive counting of the cells and supernatant is performed [23].

2.3.4 Binding Assays

Binding assay detects the binding of a compound (ligand) to an ion-channel. This assay does not examine how the binding will alter the function of the channel; hence, it is not considered a functional assay. A typical binding assay involves using a radioisotope to label a known ligand for the ion-channel.

2.4 **Patch-clamp Technique**

The invention of the patch-clamp technique is accredited to Erwin Neher and Bert Sakmann, who in 1976 reported a technique to record single-channel currents from the membrane of denervated frog muscle fiber [24]. It was the first device that measured the

flow of the current through a single ion-channel. Their technique involved placing a tiny glass pipette against a living cell membrane and applying a small amount of suction to form a tight seal between the pipette and cell membrane. This electrical seal had a resistance of order of 50 M Ω [25]. Neher and Sakmann soon realized the source of noise in the measured single ion-channel current was due to the leak in the seal between the cell membrane and the pipette. In 1981, a group of researchers including Neher and Sakmann reported an improved patch-clamp technique. This technique could achieve a “gigaseal”, an electrical seal in the order of 10^9 - 10^{11} ohms, and thus reduce the noise in the recorded channel current by an order of magnitude [26]. Such was the impact of this discovery, that in 1991, Erwin Neher and Bert Sakmann were jointly awarded the Nobel Prize in Physiology or Medicine for their discoveries concerning the function of single ion-channels in the cells. Today, the patch-clamp is the most widely used technique to study the electrophysiological properties of biological membranes and widely accepted as a gold standard in electrophysiology.

2.4.1 Principle of Operation

An electrical model for a cell is shown in Figure 2-5. The membrane represents a capacitance C_m ; the conductance of each ion-channel (g_{Na} , g_{Ca} , g_{K1} , g_{K2} , g_l) present in the cell is a variable depending on whether the channel is open or closed. The current through a single ion-channel can then be represented by a variable conductance in a series with the reverse potential of the channel. The membrane potential E depends on the ion-channel currents I_j according to [27]

$$C_m \frac{dE}{dt} + \sum_j I_j = 0. \quad \text{Eq. 2-1}$$

The current through an individual ion-channel can then be modeled as

$$I_j = g_j(E - E_j). \quad \text{Eq. 2-2}$$

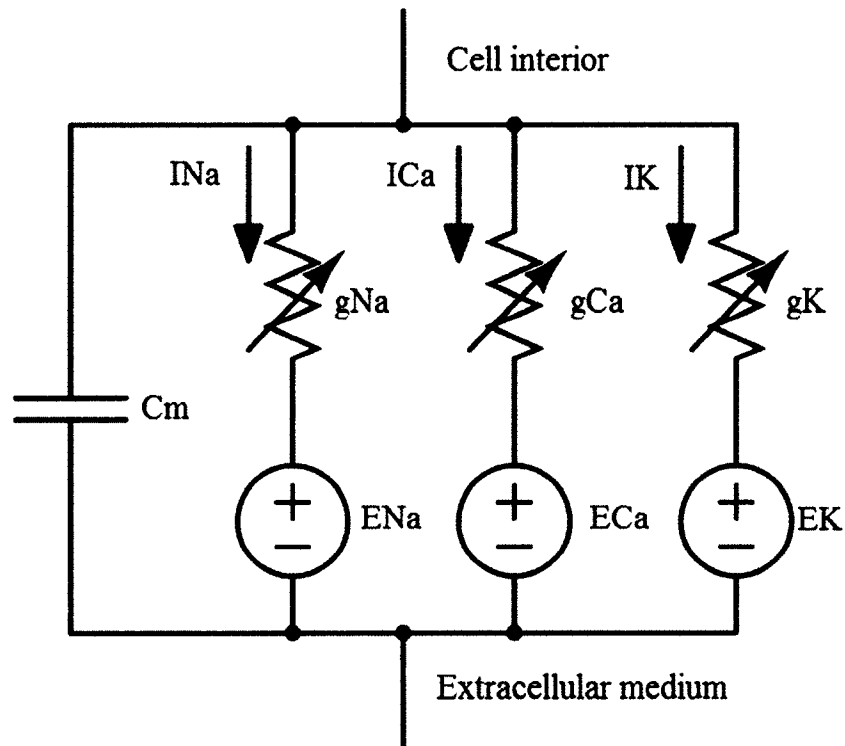


Figure 2-5: Electrical model of a cell. The sodium, calcium and potassium ion-channels are modeled as a variable conductance depending upon whether they are open or closed. The cell membrane is modeled as a capacitor; the reverse potential of each channel is modeled as a voltage source.

The patch-clamp technique involves placing a pipette (tip of the pipette is a few microns in diameter) with an electrolytic solution against a living cell membrane and applying a small amount of suction. This suction forms a tight electrical gigaseal between the cell membrane and the pipette. An Ag/AgCl electrode is then inserted in the pipette such that it makes contact with the electrolyte in the pipette and a voltage pulse is applied. The ion-channel current now balances the injected current I_{inj} due to the pulse.

The relationship between the injected current I_{inj} and the ion-channel current is

$$C_m \frac{dE}{dt} + \sum_j I_j = I_{inj}. \quad \text{Eq. 2-3}$$

If E is constant, the injected current is equal to the ion-channel current, and therefore is a direct measure of the ion-channel current.

2.4.2 Patch-clamp Configurations

Researchers have used different configurations of the basic patch-clamp technique to achieve their goals. The commonly used configurations are: Cell-attached, Inside-out, Whole-cell, Outside-out, and Perforated.

2.4.2.1 Cell-attached Configuration

This is the simplest configuration that is achieved as soon as the pipette is placed against the cell membrane and a small amount of suction is applied to form an electrical seal between the pipette and the cell membrane. The advantage of this configuration is that it can measure the current through a single ion-channel in that patch of the membrane. Since the electrical seal resistance is very high, this method requires very sensitive and low-noise electronics to record the correct current.

2.4.2.2 Inside-out Configuration

This configuration is achieved with a two-step process. First, an electrical seal between the pipette and the cell membrane is achieved by placing the pipette against the cell membrane and a small amount of suction is applied (cell-attached configuration). Step two is to withdraw the pipette quickly so that it tears off the membrane patch. This configuration is preferred when the objective is to study the effect of environmental changes on the inside of the ion channels.

2.4.2.3 Whole-cell Configuration

This configuration is achieved with a two-step process. First, an electrical seal between the pipette and the cell membrane is achieved by placing the pipette against the cell membrane and a small amount of suction is applied (cell-attached configuration). Step two is to apply pulses of suction or voltage to rupture the patch membrane. Unlike the inside-out configuration, the cell is still attached to the pipette in the whole-cell configuration. As compared to the cell-attached configuration, the larger opening at the tip of the pipette is now an advantage since the resistance is lowered and there is better electrical access to the inside of the cell. The disadvantage though is that the soluble content of the cell will be quickly replaced by the solution in the pipette, and hence, the experiment has to be concluded within a shorter time frame.

2.4.2.4 Outside-out Configuration

To achieve the outside-out configuration, first the whole-cell patch is achieved, and then the pipette is withdrawn from the cell so that the patch is torn off the cell. The patch then reforms itself in the form of a ball at the tip of the pipette. This configuration is useful when the aim is to study the ion-channel function when it is not in the living cell environment.

2.4.2.5 Perforated Configuration

The perforated configuration tries to bridge the cell-attached and whole-cell configuration. Starting with the cell-attached configuration, special molecules are introduced in the pipette that is capable of perforating the patch membrane. Therefore, unlike the whole-cell configuration, the content of the cell will not be diluted quickly. The time needed to perforate the patch membrane may vary; hence, this method may not

be helpful if the experiment is to be completed in a limited time frame. Another problem that could arise is the chance that the process of patch perforation might cause rupture, and this will end up as a whole-cell configuration instead. The different patch-clamp configurations are shown in Figure 2-6.

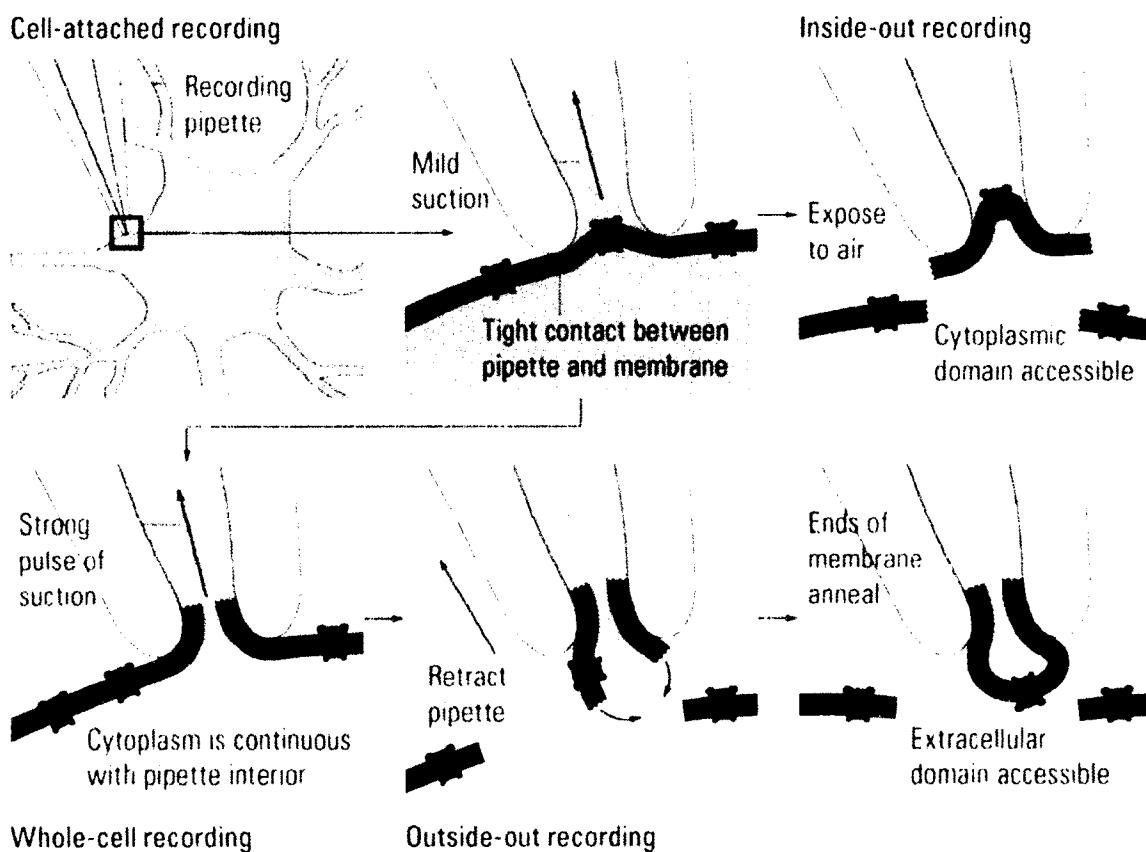


Figure 2-6: Patch-clamp configurations [28].

2.5 Planar Patch-clamp

The patch-clamp configurations are widely popular in research labs because they provide researchers the flexibility to study various ion-channel functions. However, in its simplest form, there are certain aspects of the conventional patch-clamp technique that limit the uses of this technology to research work in the laboratory. It takes a highly

skilled and experienced operator to apply the correct amount of suction to achieve the whole-cell configuration, and to perform simultaneous other activities like replacing the solution inside the pipette and recording the current while observing the cell under a microscope. The labor involved and the very low throughput make the conventional patch-clamp unpopular and unrealistic for wide use in the industry.

There is great interest in developing an automated version of the patch-clamp that can perform recordings of thousands of cells in parallel and facilitate the screening process involved in the drug-discovery cycle. In 2003, a company called Flyion used their existing Flip-the-tip technology and launched a fully automated, robot-controlled system called Flyscreen 8500 to replace the human operator in the conventional patch-clamp technique [29]. However, the technology reported by Flyion still involved using a glass pipette and throughput was still less than what the industry demanded.

The idea of having a chip that can hold several thousand micropipettes and allows parallel recordings is very intriguing, and since the 1990's there have been several attempts to develop such a chip. Where the conventional techniques exclusively made use of a glass pipette, the modern approach makes use of different materials. In the first attempt to fabricate a patch-clamp chip, both optical lithography and low-energy electron-beam lithography were used to define patterns on a silicon wafer. We then etched these patterns using reactive ion etching and wet etching to achieve orifices that were as small as 50 nm in diameter [30]. Even though the processes for fabricating micro and nano-structures out of silicon are well established, silicon does suffer from a few problems. A high-density of charge in the silicon can give rise to a parasitic current, which is undesirable when dealing with very low ionic currents, and it is also difficult to

form a gigaseal when using a silicon-based pipette [31]. Glass offers a good alternative to silicon, especially when optical methods utilizing fluorescence are used to study ion-channel functions. The seal quality is also much better between a glass pipette and a cell membrane. The conventional wet etching process on glass yields structures that are not perfectly circular and produce poor seal quality. Fertig *et al.* reported an ion-track etching technique that could produce a smooth aperture with a diameter of 1 μm or smaller [32], [33]. The basic structure of the planar patch-clamp device is shown in Figure 2-7.

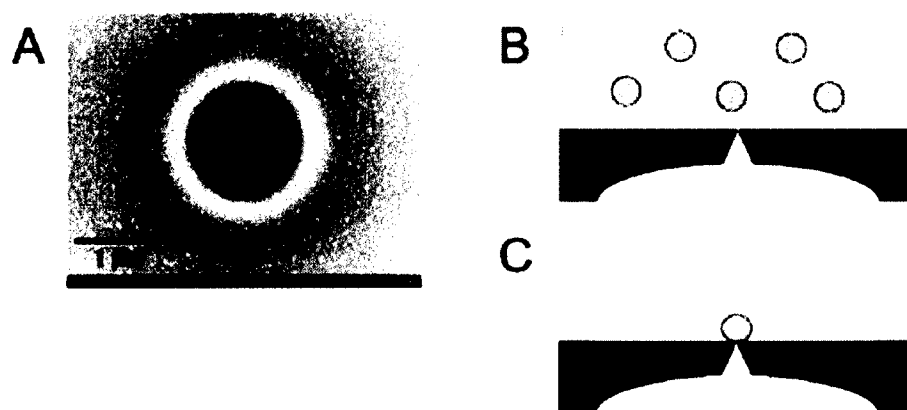


Figure 2-7: Basic structure of a planar patch-clamp device. A) Top view of the planar aperture on a glass chip. B) Cells are suspended and then suction is applied. C) A cell forming a seal with the aperture [27], [33].

One of the challenges faced when using conventional or modern day planar patch-clamp devices is the ability to reuse the micropipette. Experiments have confirmed that once the initial gigaseal between the pipette and the cell membrane is achieved, it is very difficult to reproduce another gigaseal for the subsequent capture of cells. The problem is attributed to the debris left over by the initial gigaseal which is very difficult to remove, thus hindering the subsequent formation of another gigaseal [27]. The idea of a

disposable pipette is very attractive in scenarios where thousands of precision recordings are needed.

Photolithography has been a dominant technology in fabricating micro patterns and structures, but one has little to no control over the chemistry of these structures, especially when these patterns and structures are to be fabricated out of materials made of complex functional groups. A lot of non-lithographic techniques have been used to fabricate micro and nano scale structures that can be specifically used in the field of chemistry, biochemistry and biology. A technique that involves the use of a patterned elastomer as a mask, stamp, or mold is called Soft Lithography [34]. Soft lithography produces a micro or nano scale structure by replica molding, embossing or using self-assembly as contact printing. Polydimethylsiloxane (PDMS) is a very attractive material for soft lithography; it can be easily molded and hence offers great flexibility to make complex micro and nano scale patterns. Patch-clamp devices with micrometer scale apertures have been fabricated using PDMS [35], [36]. PDMS has also become one of the most preferred materials for fabricating microfluidic channels on patch-clamp chips. Integrating microfluidic channels on the chip helps facilitate the transport of cells to the pipette site.

2.6 Cell Viability and Cytotoxicity

Cell viability deals with determining whether a cell is living or dead. As mentioned in Section 2.2.4, the toxicological property of the lead compound is important for successful drug discovery. The cytotoxicity assays performed during safety screening involves exposing a known number of sample cells to the lead compound, and then counting the surviving cells. The cell viability and cytotoxicity assays are based on

various cell functions such as: enzyme activity, cell membrane permeability, cell adherence, ATP production, co-enzyme production, and nucleotide uptake activity [37]. The commonly used techniques are colorimetric or fluorometric. The colorimetric method uses salts that change color depending on a particular cell function. For example, the salt MTT (3-(4,5-dimethylthiazol-2-yl)-2,5-diphenyl tetrazolium bromide) measures the activity of dehydrogenase enzymes. MTT is a pale yellow substrate, but when added to living cells, the tetrazolium ring of MTT is cleaved in the mitochondria of the living cells that produce a dark blue formazan. It is then easy to read the living cells with a scanning multiwell spectrophotometer [38]. The fluorometric method uses dyes and the intensity of these dyes changes according to some particular cell function. For example, Calcein-AM can pass through the cell membrane and gets hydrolyzed by the esterase in the cell to be converted to calcein, a fluorescence dye. The total esterase activity depends on the total number of viable cells; hence, the fluorescence intensity is directly correlated to the number of living cells [39].

CHAPTER 3

PATCH-CLAMP MICROCHIP: DESIGN, MATERIALS, AND EQUIPMENT NEEDED FOR FABRICATION

3.1 Patch-clamp Microchip Design

A schematic of the patch-clamp microchip used for this research is shown in Figure 3-1. This microchip comprises of a micropipette, a pipette extension, and a fluidic channel. Air bubble (AB) actuators are incorporated to guide the cell to the site of the pipette.

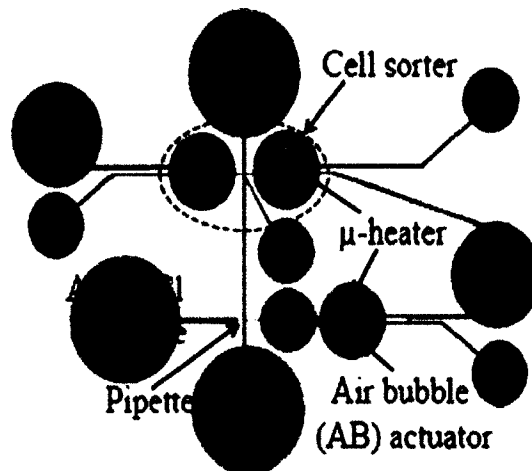


Figure 3-1: Schematic of the patch-clamp device used. The chip has actuators for selecting and positioning the cells.

3.1.1 Input and Output Wells

The cells to be tested are flown into the device via the input well. The input well is the interface between the device and the syringe containing the cells to be tested. The cells flow through the fluidic channel and the unused cells are collected at the output well.

3.1.2 Fluidic Channel Design

The fluidic channel between the input and output wells is designed to carry the cells from the input well to the site of the pipette for recording the currents.

3.1.3 Air-bubble Actuators

The air-bubble actuators allow for selecting the cell and guiding it to the pipette site. To achieve cell selection and guidance, the device makes use of integrated air-bubble actuators as shown in Figure 3-2 and Figure 3-3 [40]. These actuators consist of chromium micro heaters enclosed inside the actuator well. An external voltage creates joule heating in the micro heaters that heats the air inside the chamber to generate the air-bubbles. The air bubbles then change the path of the cell and guide it to the pipette site. A combination of actuators is used to achieve cell selection and guidance.

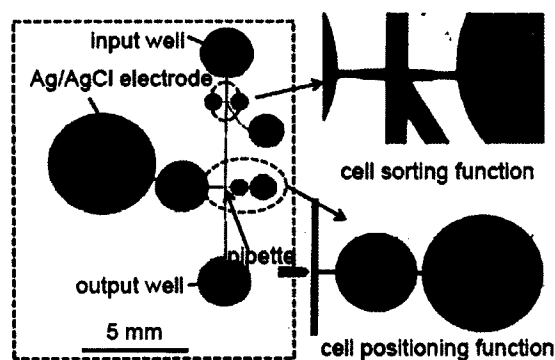


Figure 3-2: Close-up view of the cell sorting and positioning actuators [40].

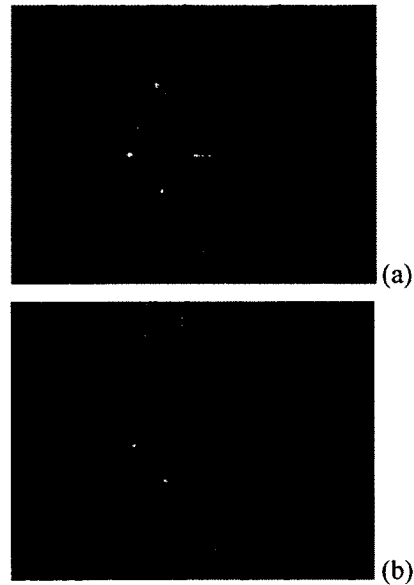


Figure 3-3: Cell sorting mechanism. A) The target cell and the target direction is identified B) Applying a voltage pulse to the actuator on the left, deflects the cell into the target direction [40].

3.1.4 Micropipette Design

The micropipette is the most important feature of the device as the aperture defines the quality of the electrical seal. The micropipette orientation and dimension are the two most important design elements. The desired length of the micropipette was 15 μm , but the mask for the micropipette was designed to have a length of 35 μm to eliminate alignment issues when the mask for the pattern containing the fluidic channel and the micropipette extension are used. Figure 3-4 shows the micropipette's position with respect to the fluidic channel and pipette.

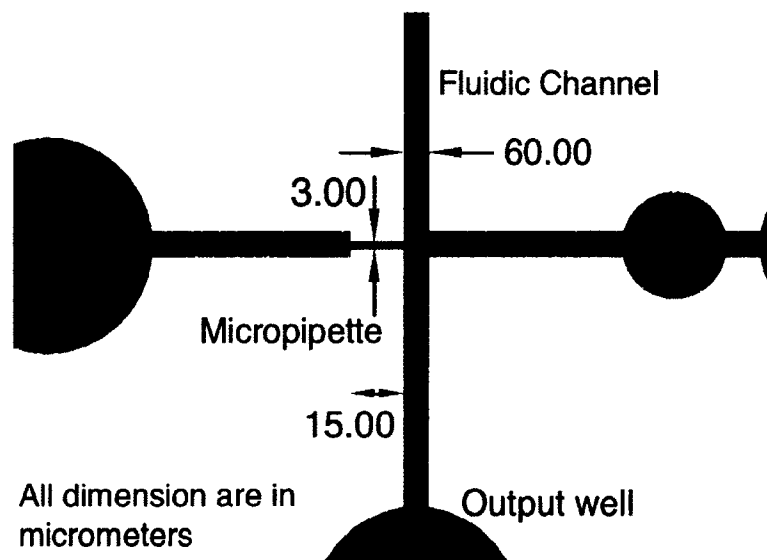


Figure 3-4: Schematic top-view of the device showing the position of the micropipette.

3.1.5 Pipette Extension

The micropipette is connected to a well via a channel as shown in Figure 3-4; this combination is called the pipette extension. To form an electrical seal, the well is connected to a device that can generate negative pressure. Once the electrical seal is achieved, the well holds an Ag/AgCl electrode to record the currents. The typical size of the MDA-MB-231 cell is between 10 and 20 μm in diameter. Hence, the width and height of the channel has to be greater than the size of the cells. Except for the micropipette (height 3 μm), the height of all the other parts is 50 μm . A 3D model of the device showing the close up view of the micropipette is shown in Figure 3-5.

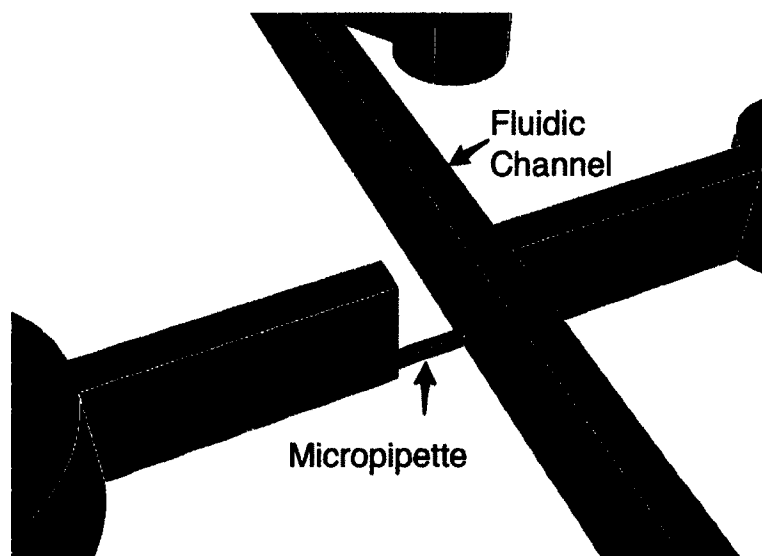


Figure 3-5: 3D model of the device showing the close up view of the micropipette. The length, width, and height of the micropipette are 15 μm , 3 μm , and 3 μm , respectively. The height of the fluidic channel is 50 μm .

3.2 Materials and Equipment

The materials and equipment needed for this project are divided based on the research cycle: fabrication of the patch-clamp microchip, and using the patch-clamp microchip to monitor cell viability.

3.2.1 Materials used for Fabricating the Patch-clamp Microchip

The patch-clamp microchip was fabricated using photolithography techniques. The following is a list of wafer cleaning chemicals, photoresists, photoresist developer, and other chemicals used to fabricate the device.

3.2.1.1 Microscopic Glass Slide

Microscopic glass slides were purchased from Fisher Scientific.

3.2.1.2 Silicon Wafer

The silicon wafers were purchased from Silicon Valley Microelectronics, Inc. Some important wafer specifications are: diameter: 100 \pm 0.5 mm, orientation: <1-0-0> \pm 1 $^\circ$, type/dopant: N/As, resistivity: 0.002-0.004 ohm-cm, and film: 2000 Å \pm 5% thermal oxide.

3.2.1.3 Ammonium Hydroxide

Ammonium hydroxide, assay 28-30 w/w% was purchased from Fisher Scientific.

3.2.1.4 Hydrogen Peroxide

Hydrogen peroxide, 30% solution, was purchased from EMD Millipore.

Ammonium hydroxide and hydrogen peroxide were used to clean the organic impurities on the silicon wafer.

3.2.1.5 Polydimethylsiloxane (PDMS)

PDMS was the material of choice to transfer the device pattern containing pipette, actuator wells and the fluidic channel. As discussed in Section 2.5, PDMS is a very attractive material to fabricate chips that are disposable and cost effective. Micro and nano scale patterns can be easily transferred to PDMS using techniques like replica molding, embossing, or by using self-assembly as contact printing. We purchased PDMS (Sylgard® 184 Silicon Elastomer Kit) from DOW Corning Corporation.

3.2.1.6 PDMS Curing Agent

PDMS curing agent (Sylgard® 184 Silicon Elastomer Curing Agent) was purchased from DOW Corning Corporation.

3.2.1.7 SU-8 2050

SU-8 2050 is a high contrast, epoxy-based photoresist designed for micromachining and other microelectronic applications where a thick, chemically and thermally stable image is desired. SU-8 2050 has excellent imaging characteristics and is capable of producing very high aspect ratio structures. SU-8 2050 has very high optical transmission above 360 nm, which makes it ideally suited for imaging near vertical sidewalls in very thick films. SU-8 2050 is best suited for permanent applications where it is imaged, cured and left on the device. There are several patterns (pipette, actuator wells, input and output wells, and fluidic channel) required on the mold and it is critical to appreciate the different dimensions needed for them. Figure 3-5 highlights the height variation needed for the pipette and the rest of the pattern. SU-8 (negative photoresist) is a common material used to fabricate molds, but in this case, using SU-8 to fabricate the pipette mold complicates the process because SU8 has to be coated on the silicon wafer with two different thicknesses. To simplify the process, the pipette mold was fabricated out of silicon, while the rest of the patterns on the mold were fabricated out of SU-8.

3.2.1.8 SU-8 Developer

The SU-8 developer is used to develop patterns exposed on the SU-8 photoresist.

3.2.1.9 Shibley S1813

Shibley S1813 is a positive photoresist; upon exposure to light, the photoresist depolymerizes which makes it easy to selectively dissolve the exposed resist faster with the help of a developer.

3.2.1.10 LOR 7B

Lift-off resist, LOR 7B, was purchased from MicroChem. LOR 7B, when used in conjunction with a photoresist to create a bilayer, can facilitate a high-yield metal lift-off process.

3.2.1.11 MF-319

MF-319 was purchased from DOW Chemical. MF-319 is used to develop patterns exposed on Shipley 1813 photoresist; it is also capable of developing LOR 7B.

3.2.1.12 Remover PG

Remover PG was purchased from MicroChem. Remover PG is a solvent stripper designed to remove photoresists efficiently and completely. It was also used in the lift-off process as a lift-off solvent.

3.2.2 Materials Needed for Monitoring Cell Viability

3.2.2.1 Calcein AM

Calcein is a fluorescent dye and Calcein AM is the acetomethoxy derivate of calcein. Calcein AM can be transported into live cells through the cellular membrane, which makes it useful for testing the cells' viability and for short-term labeling of cells.

3.2.2.2 Propidium Iodide

Propidium iodide is a fluorescent molecule, which cannot permeate into living cells and is generally used for identifying dead cells in a population.

3.2.2.3 Cell Lines and Culture

Four human breast cancer cell lines have been used for these studies, which includes MDA-MB231, MDA- MB231-brain metastatic subline (abbreviated as MB231-BR), MB231-BR over-expressing HER2 gene (MB231-BR-HER2), and MB231-BR-

vector control for the HER2 (MB231-BR-vector). The cells were transfected to overexpress HER2 as described by Palmieri *et al.* [41]. The MB231-BR, MB231-BR-HER2, and MB231- BR-vector cell lines were kindly provided by Dr. Patricia Steeg (Women's Cancers Section, Laboratory of Molecular Pharmacology, National Cancer Institute, National Institutes of Health, Bethesda, MD). The cells were maintained in Dulbecco's modified Eagle Medium (DMEM, Invitrogen) supplemented with 10% fetal bovine serum (FBS, Invitrogen) and 1% penicillin treptomycin solution (Invitrogen).

3.2.3 Equipment Needed for Fabrication

3.2.3.1 Inductively Coupled Plasma Etcher

Inductively coupled plasma etcher (Alcatel 601E) was used to etch the micropipette pattern in the silicon wafer.

3.2.3.2 Oxygen Plasma Etcher

A low powered reactive ion etcher (Technics Micro-RIE, Series 800) was used to generate oxygen plasma to bind the PDMS mold on the silicon wafer.

3.2.3.3 Hot Plate

The hot plate was used to dry the wafer after the initial cleaning step. The soft-bake required for the photoresist and LOR 7B was also done on the hot plate.

3.2.3.4 Spin Coater

The spin coater, manufactured by Cost Effective Equipment, was used to coat the uniform thickness of the photoresist and LOR 7B on the wafer.

3.2.3.5 UV Light Source and Mask Aligner

SUSS MicroTec mask aligner was used to align the mask and the wafer; the wafer was then exposed to a UV light source.

3.2.3.6 E-beam Evaporator

The E-beam evaporator from CHA industry was used to deposit chromium (Cr) on the micro heaters' pattern.

3.2.3.7 Optical Microscope

An optical microscope (Olympus Vannox AHMT3) was used during various stages of fabrication to inspect the patterns on the wafer.

3.2.4 Equipment Needed for Monitoring Cell Viability

3.2.4.1 Syringe Pump

A syringe pump (kd Scientific) was used to pump the cells into the fluidic channel.

3.2.4.2 Biopsy Punch

We used 1.5 mm Biopsy punch (Miltex, Inc) to punch holes into the PDMS mold at the sites of input and output wells.

3.2.4.3 Tubes

Tubes were used to connect the syringe pump to the input well to allow the transport of cells.

3.2.4.4 Patch-clamp Amplifier

To measure the ion-channel currents, we utilized a patch-clamp amplifier (Dagan Corporation, PC-ONE).

3.2.4.5 Digital Oscilloscope

We record the ion-channel currents using a digital oscilloscope (Tektronix TDS 1012B).

3.2.4.6 Fluorescence Microscope

A fluorescence microscope (Olympus 1X51) was used to capture the fluorescent signals from the Calcein AM and Propidium Iodide.

CHAPTER 4

PATCH-CLAMP MICROCHIP: FABRICATION

The entire microchip fabrication can be divided in four major steps: 1) Fabricating the mold on a silicon wafer; the mold contains the patterns for the pipette, actuator wells, input and output wells, and the fluidic channel 2) Transferring the patterns on the mold to PDMS 3) Fabricating air-bubble actuators on a glass substrate 4) Binding the PDMS replica with the air-bubble actuators on the glass substrate.

4.1 Mold Fabrication

The mold contains the patterns for the pipette, actuator wells, input and output wells, and the fluidic channel.

4.1.1 Pipette Mold

As mentioned earlier, the pipette is the most critical part of the device due to the specific dimensions needed. The traditional top-down approach was used to fabricate the pipette out of silicon. First, the p-type silicon wafer (<100>) was cleaned using 1:1:5 solutions of the ammonium hydroxide, hydrogen peroxide and deionized water at 80° C for 15 minutes. The wafer was then dried on a hot plate at 100° C for 10 minutes. A one micron thick layer of Shipley 1813 photo resist was uniformly coated on the wafer using a spin coater (Brewer Science, Model 100). The wafer was then baked on a hot plate at 100° C for 90 s and cooled at room temperature for five minutes. The pipette mask was

mounted on a SUSS MicroTec mask aligner, and the wafer was loaded in the machine and exposed. The data sheet for photo resist 1813 specifies the exposure time and the energy required for a good transfer of pattern. In most cases, the exposure time and energy required varies according to the life of the light source. For this machine, the exposure time between 6-10 s and a power of 1000 watts has always proved sufficient to successfully transfer the pattern onto the wafer. The exposed wafer was developed in MF319 for around 90 s, rinsed with DI water, and baked on a hot plate at 100° C for 60 s. To etch the pattern, the wafer was loaded in an inductively coupled plasma etcher (Alcatel 601E). The deep reactive ion etching (DRIE) process was used; each cycle is composed of the etching step followed by the passivation step. First, the silicon was etched by flowing SF₆ gas at a rate of 100 sccm (standard cubic centimeter per minute) for 4 s and then C₄F₈ was flown at a rate of 70 sccm for 6 s to protect the sidewalls. The RF power was maintained at 800 W and the plate voltage was maintained at 35 V for the etching step. It took around 15 cycles to etch 3 μm of silicon pipette pattern. After the etching process, the photoresist on the wafer was cleaned with acetone followed by an IPA and DI water rinse. The final pipette dimensions are: 35 μm, 3 μm, and 3 μm for length, width, and height, respectively. Figure 4-1 shows the pattern generated in the plane containing the cross-section of the pipette extension (input well and the channel connecting the pipette), and the fluidic channel.

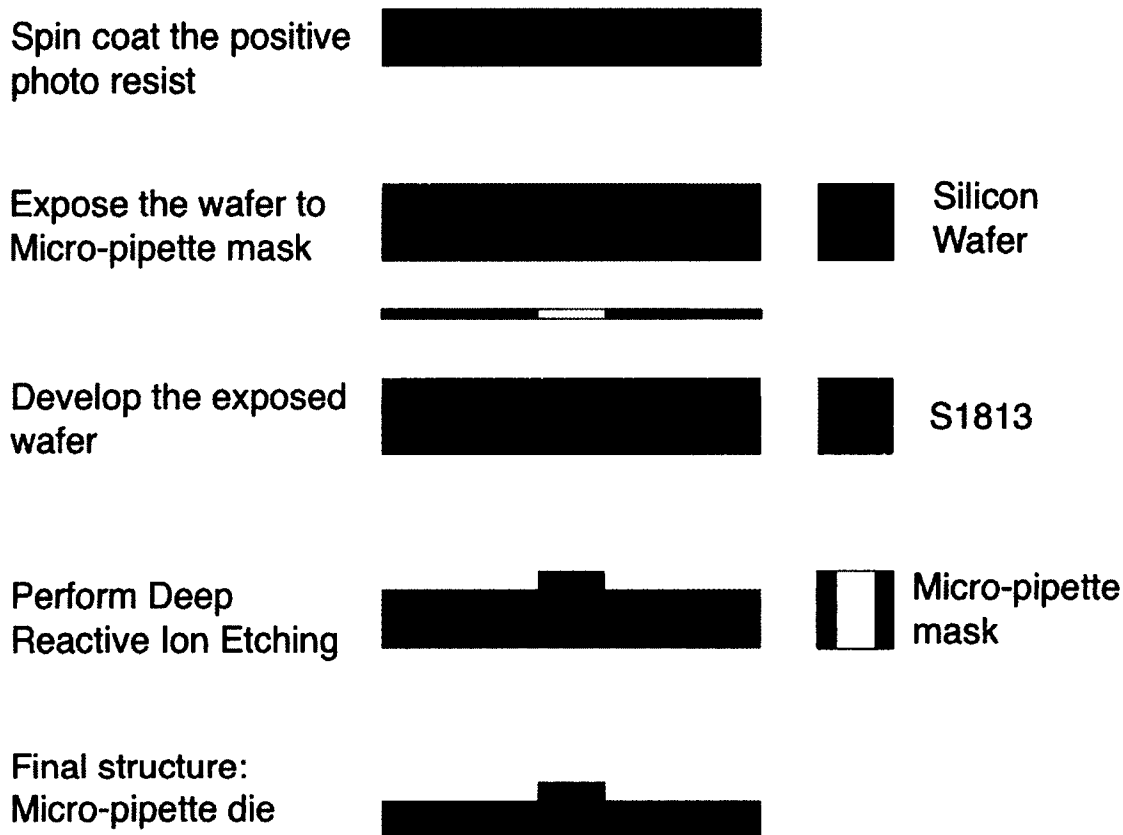


Figure 4-1: Process flow for fabricating the pipette mold on the silicon wafer.

4.1.2 Mold for Actuator Wells, Input and Output Wells, and Fluidic Channel

A standard clean was performed on the silicon wafer with the pipette mold to remove organic waste deposited during the etching step. The required thickness for this mold is 50 μm as discussed in Section 3.1. The data sheet for SU-8 2050 specifies the resist to be spun at 3000 rpm to achieve 50 μm thickness [42]. The deposition was followed by a soft bake at 95° C for 6 minutes and then the wafer was cooled at room temperature for 10 minutes to remove any unwanted wrinkles. The wafer was then aligned with the mask mounted on the mask aligner and exposed to a light source of 350-400 nm and energy of 150-215 mJ/cm^2 . A post exposure bake at 95° C for six minutes was performed before immersing the wafer in the SU-8 developer for 5-7 minutes to

develop the patterns on the wafer. Finally, the wafer was rinsed with IPA and DI water and dried with nitrogen. The process flow shown in Figure 4-2 shows the patterns generated in the plane containing the cross-section of the pipette extension (input well and the channel connecting the pipette), and the fluidic channel. It is now easy to appreciate why the length of the pipette in the pipette mask is 35 μm and not 15 μm , which is what is desired. For a pipette length of 15- μm , any alignment error due to the machine or the operator can create a scenario where the pipette is either not connected to the pipette extension or the fluidic channel. The longer length of the pipette ensures there is no break along the path containing the pipette extension, pipette and the fluidic channel. A 3D model of the SU-8 mold is shown in Figure 4-3.

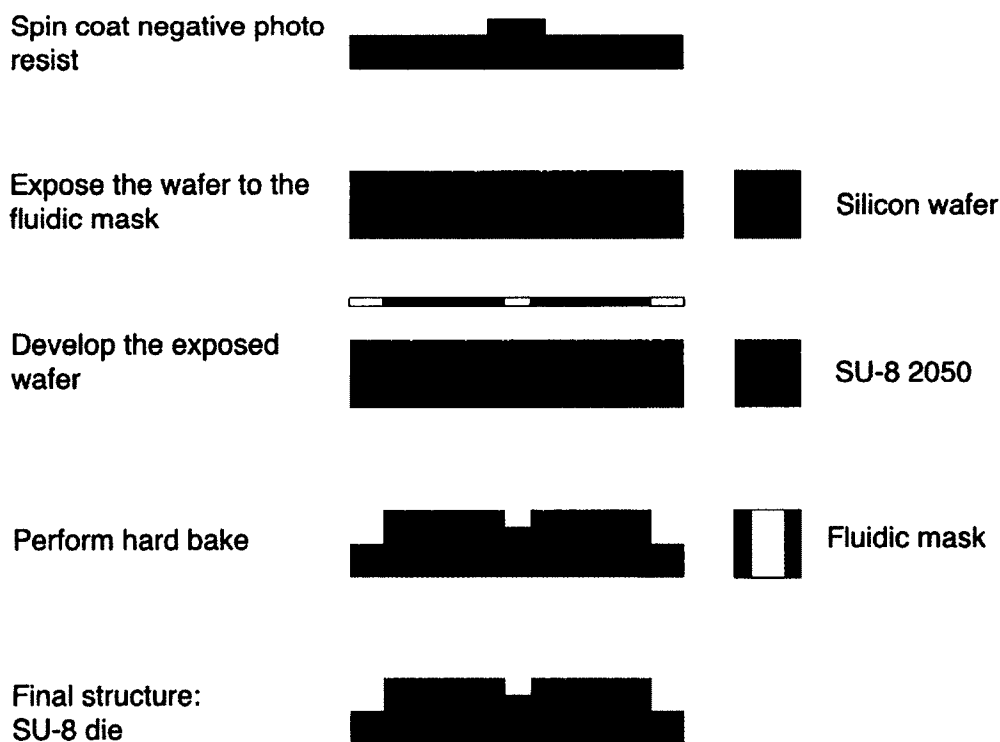


Figure 4-2: Process flow showing the pattern generated in the plane containing the cross-section of the pipette extension and the fluidic channel.

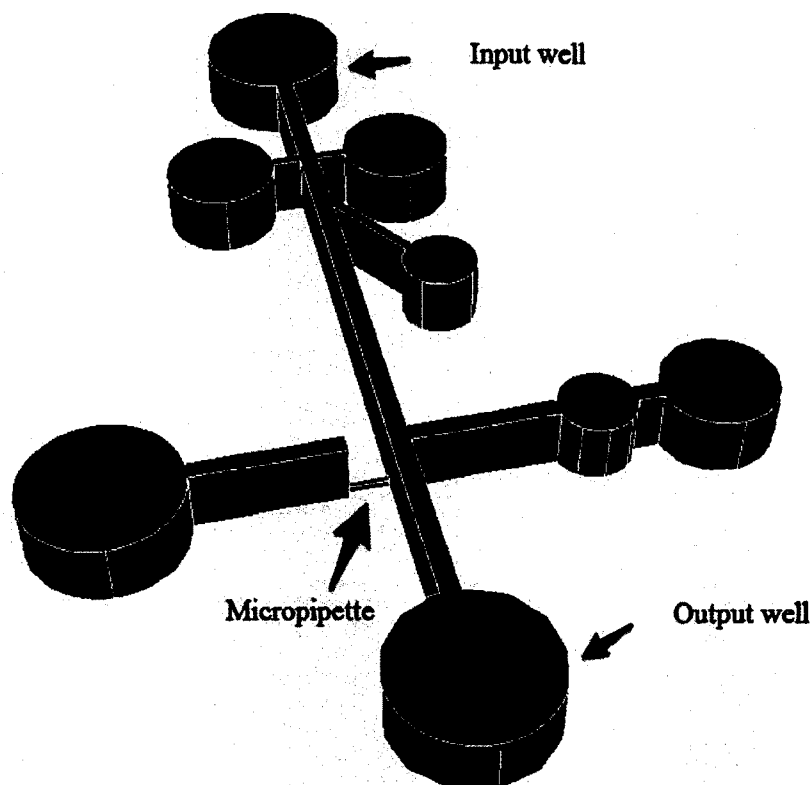


Figure 4-3: 3D model of the SU-8 mold. The mold for input and output well, fluidic channel, air-bubble actuators, and Ag/AgCl electrode is made out of SU-8 (red color). The mold for the micropipette is made out of silicon (blue color)

4.2 PDMS Replica

The curing agent was added to the PDMS base 1:10 ratio and stirred well, which caused air, visible as air bubbles, to be trapped in the mixture. The mixture was then placed in a degassing chamber and the pressure was gradually reduced to less than 200 Torr for 30 minutes. This mixture was then poured over the mold and baked in a conventional oven for three hours at 70° C. After removing the mold from the oven, the PDMS was carefully peeled off the mold and the replica was obtained.

4.3 Air-Bubble Actuators

The glass slide was first cleaned in a solution containing 1:1:5 of ammonium hydroxide, hydrogen peroxide and DI water, respectively, at 80° C for 15 minutes. A 700 nm thick layer of LOR 7B was deposited on the glass slide by spinning the slide in the coater at 3000 rpm for 45 s. The glass slide was soft baked on the hot plate at 180° C for three minutes and subsequently cooled at room temperature for five minutes. The soft bake temperature and time are critical as they have a direct effect on the undercut rate [43].

Next, a one-micron thick layer of S1813 resist was deposited on the glass slide using a spin-coater spinning at 3000 rpm for 50 s. The glass slide was then soft baked on a hot plate at 100° C for 90 s followed by cooling it at room temperature for five minutes. The micro heater pattern was then transferred on the glass slide using the mask aligner and immersed in MF319 solution for 60 s to develop the pattern. Following a DI water rinse, the undercut pattern was investigated under the microscope continuously. A good undercut ensures easy lift off; if the undercut was not prominent, the slide was immersed back into the developer solution and reinvestigated for the undercut.

After achieving a good undercut, a 200 nm thick layer of chrome was evaporated on the slide. The slide was then immersed in a bath of Remover PG solution maintained at 60° C for three hours. After three hours, if the resist stack was not lifted off completely, the Remover PG bath was changed and the slide was re-immersed for additional time until the entire resist stack was completely removed. Finally, the glass slide was cleaned with IPA and DI water. The complete fabrication process for the air-bubble actuator is shown in Figure 4-4.

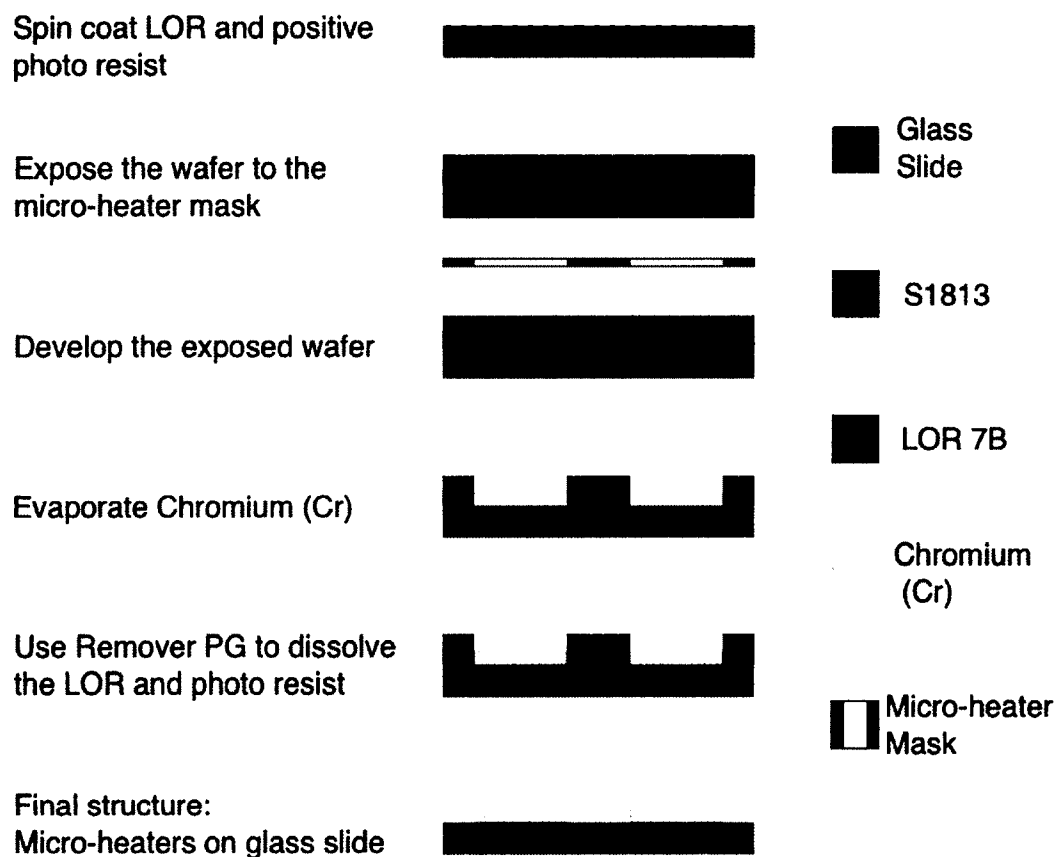


Figure 4-4: Process flow for fabricating the air-bubble actuators.

4.4 Binding PDMS Replica with the Air-Bubble Actuators

To bond the PDMS replica with the glass slide, the PDMS replica was treated with oxygen plasma (35 sccm, 60 W, 10 s) and aligned on the glass slide containing the micro-heaters.

CHAPTER 5

PATCH-CLAMP MICROCHIP: EXPERIMENTAL SETUP AND PROTOCOL

5.1 Experimental Setup

The objective of the experiment is to establish that the fabricated planar patch-clamp microchip is a capable alternative to measure cell viability. The experiments are set up in a manner such that both fluorescence imaging and ion-channel currents can be recorded simultaneously. The fluorescence images are recorded with an Olympus inverted fluorescent microscope (Olympus, Inc.), while the ion-channel current is recorded by a combination of a patch-clamp amplifier (Dagan Corporation, PC-ONE) and a digital oscilloscope (Tektronix TDS 1012B). It is very important to note this in order to minimize or even eliminate the EM interference. Ideally, patch-clamp recordings are performed in a Faraday cage to minimize or even eliminate the electromagnetic (EM) interference. Proper electrical shielding and grounding practice is observed to reduce or eliminate the noise. The cells are pumped into the input well of the device using a syringe pump. The microchip with assembled Ag/AgCl electrodes and tube connections is shown in Figure 5-1.

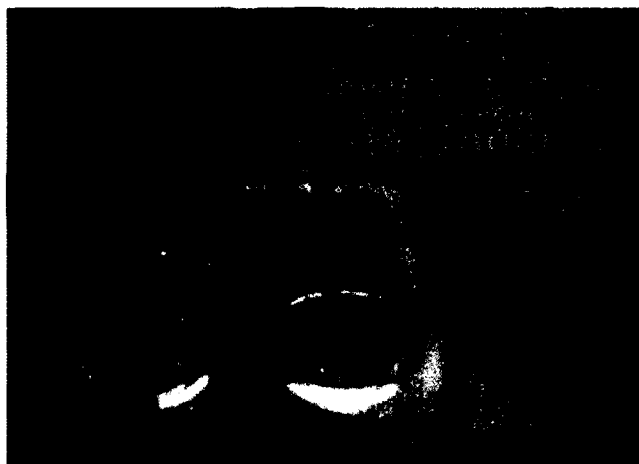


Figure 5-1: Fabricated microchip with assembled Ag/AgCl electrodes and tube connection at input well for cell flow.

5.2 Experiment Protocol

The cells were stored in the DMEM buffer; hence, it was important to record the resistance of the device with only the buffer flowing through it. The first step of the experiment was to measure the open pipette resistance. To measure this resistance, the DMEM buffer without the cells was flown in the device and then 20 mV, 40 Hz square wave pulse was applied, and the recorded ion-channel current was used to calculate the seal resistance. Next, the DMEM buffer containing cells was pumped into the input well of the device using the syringe pump. The flow of the cells was observed under the microscope and the cell sorting and positioning mechanism was used to guide the cell to the site of the pipette. Negative pressure was then applied to form the electrical seal between the cell and the pipette. Following the cell capture, a 20 mV, 40 Hz square wave pulse was applied to the Ag/AgCl electrode. The ion-channel current and the fluorescence image of the captured cell were recorded simultaneously.

CHAPTER 6

PATCH-CLAMP MICROCHIP: RESULTS AND DISCUSSION

6.1 Ion-channel Current and Seal Resistance of Cell

An optical image of a captured cell by the micropipette is shown in Figure 6-1. To record the ion-channel current, a square-wave voltage pulse of 20 mV, 40 Hz is applied. The recorded ion-channel current through the device over a period of time is shown in Figure 6-2. As expected, under the open pipette condition, the current through the device is higher, and the calculated seal resistance is $\sim 4 \text{ M}\Omega$. Once the cell is captured, the seal between the cell membrane and the pipette offers a high-resistance. The current through the device is now a combination of the ion-channel current and the leakage current through the seal, with the ion-channel current being the dominant source. The curve $T = 0$ minute corresponds to the first ion-channel current recorded after the cell is captured. At this instance the cell has the highest viability, and hence, the lowest ion-channel current of $\sim 280 \text{ pA}$ and largest seal resistance of $\sim 22.0 \text{ M}\Omega$. As mentioned in Section 2.6, the cell membrane permeability is an indicator of cell viability. Even though the buffer surrounds the cell, over a period of time, the cell will lose its viability and, as the cell starts to die, the ion-channel current increases. The recording at $T = 30$ minutes shows that the ion-channel current has increased and the corresponding seal resistance has decreased from

22.0 M Ω to 6.5 M Ω . Eventually after 2 hours the cell is dead and the current is back to the level of open pipette and seal resistance is ~ 4 M Ω .

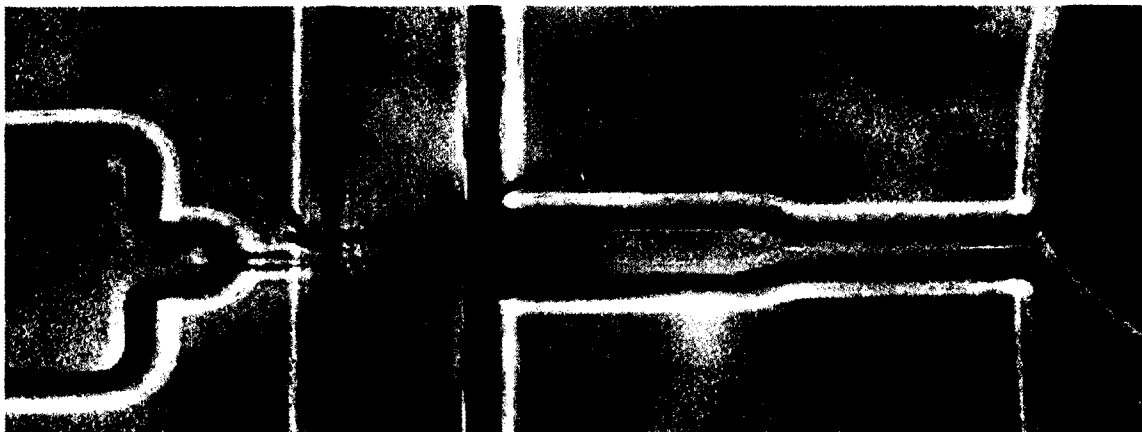


Figure 6-1: Close up view of captured cell [12].

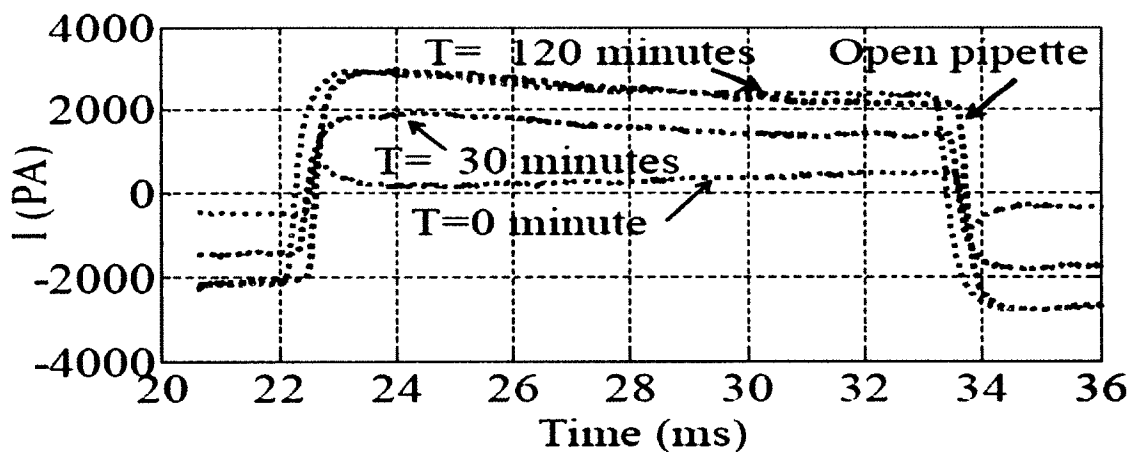


Figure 6-2: Current through the device over the test period. The current is in response to a 20 mV, 40 Hz square wave pulse [12].

6.2 Fluorescence Images of Cell

As mentioned earlier, the ion-channel currents and the fluorescence images of the cell were simultaneously recorded. Figure 6-3 shows the representative fluorescence images of the captured cell. As expected, immediately after its capture, the living cell has

brighter green fluorescence due to the fact that calcein AM can permeate into living cells through the cellular membrane. Propidium iodide (PI), however, cannot permeate into living cells and hence the cell image shows a dimmer red fluorescence. After 120 minutes the cell loses its viability, which reverses the intensity of the fluorescence. PI now permeates into the dead cell and therefore the cell image shows brighter red fluorescence, while the green fluorescence, due to Calcein AM, grows significantly dimmer.

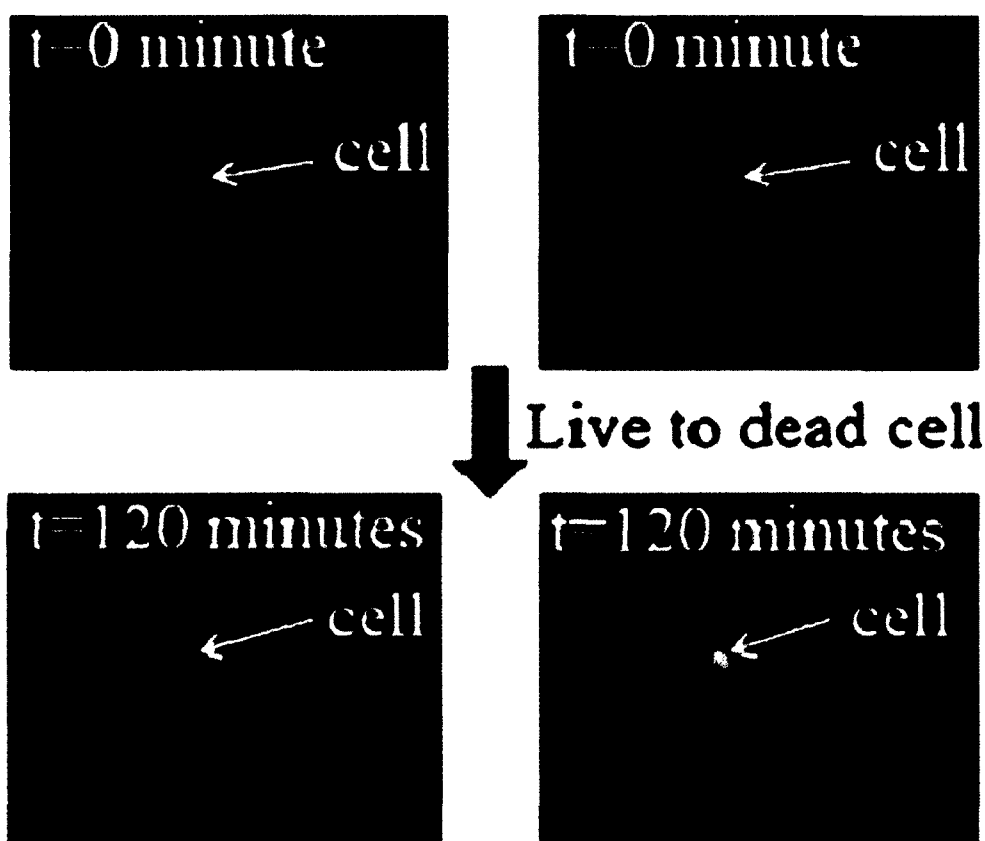


Figure 6-3: Fluorescence images of the cell, the green fluorescence is due to Calcein AM and red fluorescence is due to PI [12].

6.3 Comparing the Seal Resistance and Fluorescence Intensity

To validate the viability of this platform, the seal resistance of the device was compared with the recorded PI fluorescence images of the cell. In Figure 6-4, the blue

curve represents the variation in seal resistance of the device over a period of time while the red curve represents the variation in PI fluorescence intensity. At $T = 0$, the cell is alive and the recorded seal resistance is $\sim 22 \text{ M}\Omega$, while the recorded intensity of the PI fluorescence is low. At $T = 120$ minutes, the cell is dead and the recorded seal resistance has decreased to $\sim 4 \text{ M}\Omega$, while the recorded intensity of PI fluorescence has increased significantly.

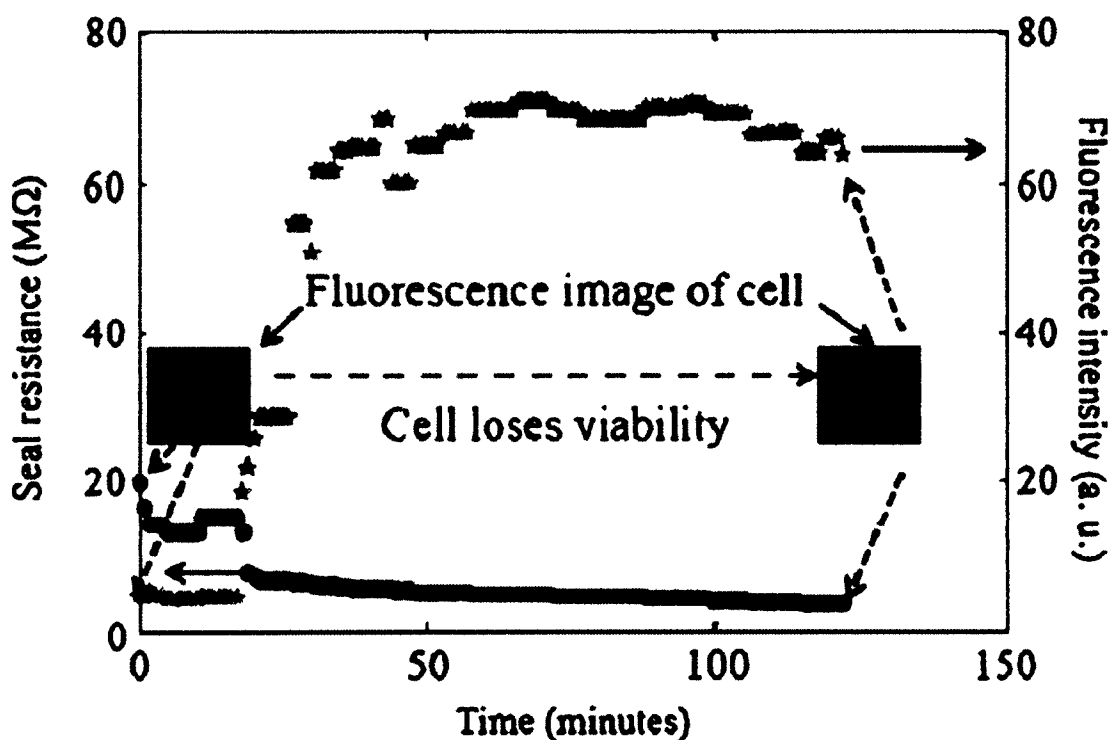


Figure 6-4: Representative measured seal resistance of the captured cell and corresponding PI fluorescence intensity. Inset at $T = 0$ is the PI fluorescence image of the live cell (immediately after capture) and inset at $T = 120$ minutes is the PI fluorescence image of the dead cell [12].

In order to obtain systematic experimental results, about 12 cells from each cell line (cell line 1 MB231; cell line 2 MB231-BR-vector; cell line 3 MB231-BR-HER 2; cell line 4 MB231-BR) were tested. It took about two to four hours to complete the experiments for each cell. Representative experimental results for five cells from each

cell line are plotted in Figure 6-5. The recorded ion-current values show a consistent decrease in the seal resistance as the cell loses its viability, until finally the seal resistance reaches the value of open pipette. Based on these results, it is very clear that the change in seal resistance correlates very well with the health (alive or dead) of the cell.

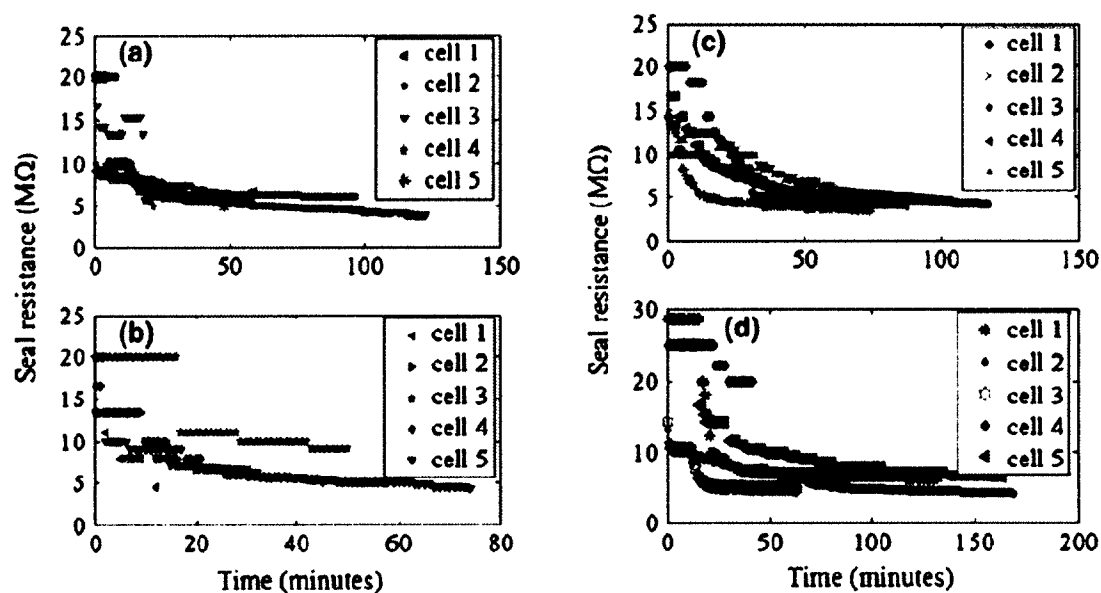


Figure 6-5: Summary of seal resistance change for four cell lines, a change in the seal resistance shows similar trend. a) cell line 1 MB231; b) cell line 2 MB231-BR-vector; c) cell line 3 MB231-BR-HER 2; d) cell line 4 MB231-BR [12].

6.4 Summary

In this chapter we discussed the performance of the patch-clamp microchip. The ion-channel currents for 12 cells from each cell line (cell line 1 MB231; cell line 2 MB231-BR-vector; cell line 3 MB231-BR-HER 2; cell line 4 MB231-BR) were recorded over a period of time and simultaneously fluorescence images of the cell were also recorded. The validity of the patch-clamp microchip as a viable technical platform for real-time monitoring of cell viability was established after comparing the change in seal resistance and the change in intensity of fluorescence images.

CHAPTER 7

PATCH-CLAMP MICROCHIP: CONCLUSIONS AND FUTURE WORK

7.1 Conclusions

Systematic measurements of the cell's electrical properties (e.g., ion channel current and seal resistance) were performed using PC microchips. All of the experimental results indicate that PC microchips provide a viable technical platform for monitoring cell viability in real time. This was confirmed by simultaneously carrying out the experiments using the conventional technology i.e. monitoring the changes of the fluorescence images of cells. Therefore, given its simplicity of direct electrical measurement of cells without fluorescence labeling, the technical platform based on PC microchips may pave a way for high efficiency drug effect analysis on cancer cells given their direct electrical measurements on cells and the fluorescence dye labeling of the cells can be completely avoided.

7.2 Future Work

This technique can quantify the ion current and seal resistance of single cells, thereby providing the quantified information for specific types of cells, which would greatly benefit ion-channel based drug discovery [44], [45].

Future work will focus on the real-time monitoring of controlled drug effects on cells using this platform. This will be achieved by integrating a controlled drug release microfluidic platform with PC microchips.

CHAPTER 8

FET BASED BIOSENSOR: INTRODUCTION

Proteins, including enzymes, antibodies and some hormones, are common targets in clinical diagnosis. The ability of an antibody to identify and form complexes with corresponding antigen is highly specific and forms the basis of immunoassay techniques. ELISA is the most commonly used conventional enzyme immunoassay technique but has several limitations. To begin with, these techniques require a laboratory setup with a highly qualified technician who can execute the complex multistage process while analyzing the results. The analysis can take several hours, making it unsuitable for applications where quick determination of analyte is required. Smart biochips made of novel materials and structures are now capable of performing some of the basic *in vitro* diagnostic tests involved in immunoassays. The discovery of novel materials like carbon nanotube (CNT) has opened up new opportunities to engineer biosensors made from individual CNT that are ideally capable of detecting biomolecules on a molecular level.

Since every atom in a CNT is a surface atom, they form an ideal class of 1D nanostructures that could exhibit ideal sensitivity at a single molecular level [46]. The transfer of charge from one electrode to another is a very important aspect in any electrochemical reaction, and it has been shown that CNTs promote electron-transfer reactions of proteins [47]. Most of the modern biosensors have exploited the

semiconducting nature of CNT to design a label-free field-effect transistor (FET) based immunosensor (biosensor that exclusively monitors the antibody-antigen interaction). Even though biosensors made out of a single CNT are ideally capable of detecting a single molecule, the biggest hurdle in using CNT for biosensors is the process involved in assembling this nanostructure into the sensor. For sensors based on 1D structure like CNT, there are huge variations in the device's characteristics. Due to these variations, it is very important to calibrate each sensor before use. It is a major challenge to develop a reusable CNT based sensor that can be calibrated easily before deployment in a real-life scenario.

To avoid the fabrication complexity involved with a single CNT immunosensor, we have developed an FET based biosensor, in which the channel is fabricated out of carbon nanotubes thin film (CNTF). The CNTF channel between the source and drain electrodes was assembled using electrostatic layer-by-layer assembly (LBL). To investigate the potential of the device as an immunosensor, we used the bio-affinity interaction between Protein A and rabbit IgG to model the antibody-antigen interaction.

8.1 Key Accomplishments of the Project

The key accomplishments of the project include the fabrication of the FET device using LBL assembly and the verification of the behavior of the device as a p-type transistor. To study the antibody-antigen interaction, the bio-affinity interaction between Protein A and rabbit IgG was used as a model and initial results suggest that the device can detect IgG concentrations as low as 1 pg/mL.

8.2 Outline of FET Based Biosensor Project

In CHAPTER 9 we begin with a discussion on conventional techniques used in immunoassays, their disadvantages, and make a case for the use of biosensors. The various types of biosensors and the impacts of nanotechnology on these sensors are discussed. A detailed study of carbon nanotube and its application as an electrochemical sensor is presented, along with a brief discussion on protein immobilization and its significance. Next, a discussion on the challenges involved in fabricating a sensor made out of single CNT and a case for carbon nanotubes thin film (CNTF) is made. Finally, the fabrication techniques, with a focus on layer-by-layer self-assembly and electrical properties of CNTF, are discussed.

In CHAPTER 10 the design aspects of the device are presented, as well as a mention of the various materials and equipment required to fabricate the biosensor.

A detailed fabrication process for each component of the biosensor is discussed in CHAPTER 11.

CHAPTER 12 begins with an introduction to the experimental setup and the protocol used, continues with a discussion on the behavior of the device as a transistor, and ends with a discussion on the performance of the device as a biosensor to detect the bio-affinity interaction between Protein A and rabbit IgG.

In CHAPTER 13 we summarize the FET based biosensor project and discuss its future direction.

CHAPTER 9

FET BASED BIOSENSOR: RESEARCH BACKGROUND

The immune system in our body protects us from microorganisms and other chemical agents. This system is made up of special cells, proteins, tissues and organs and is continuously monitoring the body for the presence of pathogens (foreign substance like bacteria, virus, or other microorganisms). More specifically, the immune system looks for the presence of an antigen; which is a molecule (mostly protein) attached to a pathogen. The presence of an antigen triggers the immune system to produce a specialized protein called an antibody that locks onto the specific antigen and eventually destroys the pathogen. The world we live in today is a complex place, where we consume more processed foods, commonly travel across continents, produce industrial waste that contaminates water sources, and face the possibility of biological and/or chemical warfare. Advancement in science and diagnosis of diseases over the last century has improved human health significantly, but there are a growing number of factors, including food and water, that could have an adverse effect on our health or could prove to be fatal. It is a never-ending quest to develop technologies that can detect biological and chemical pathogens, contaminants or other agents that can cause the spread of a disease and infection. The field of pathogen detection is expansive, and as shown in

Figure 9-1, research areas like water and environmental control, food industry and clinical diagnosis account for more than two-thirds of all the research in this field [48].

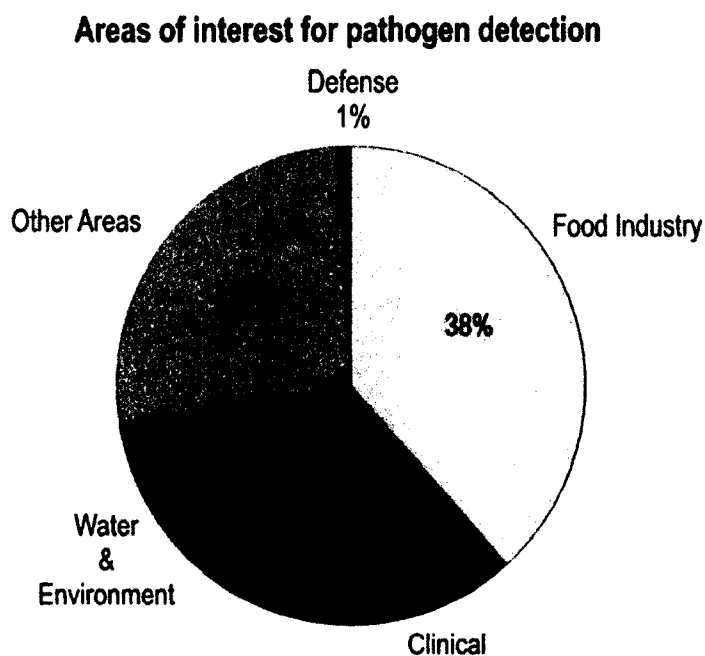


Figure 9-1: Areas of interest for pathogen detection [48].

9.1 Diagnostic Targets

In conventional diagnosis, the sample taken from the patient travels to a laboratory where a skilled technician runs various diagnostics tests to confirm whether the patient tests positive or negative for a particular disease. Any clinical diagnostic test is designed to detect a specific analytical 'target' in the patient's sample. The target list includes proteins, nucleic acids, metabolites, drugs, dissolved ions, human cells, and microbes. The sample can be a patient's blood, saliva, urine, or other bodily fluids or semi-fluids. When it comes to detecting pathogens, there are two popular diagnostic targets: nucleic acids and proteins.

9.1.1 Nucleic Acids

The diagnosis based on nucleic acids is often referred to as “molecular diagnostics”. There are two approaches to molecular diagnosis to measure the DNA or various types of RNA to assay particular genomic or genetic details of a patient, or to assay the nucleic acid sequence unique to the invading pathogens. The assay is based on the isolation, amplification, and quantification of the target nucleic acid sequence. Techniques like Polymerase Chain Reaction (PCR) are very common in molecular diagnostics. Kary B. Mullis developed the PCR technique in 1983 and in 1994 he and Micheal Smith were awarded the Nobel Prize in chemistry for their work. These techniques are highly selective and sensitive, but they are also more expensive, cumbersome and time consuming than other assay techniques [49].

9.1.2 Proteins

Proteins, including enzymes, antibodies and some hormones, are common targets in clinical diagnosis. The ability of an antibody to identify and form complexes with the corresponding antigen is highly specific and forms the basis of immunoassay techniques. This extremely specific affinity of antigen-antibody lends immunoassays with a very high level of sensitivity. There are multiple ways to detect this specific antibody-antigen (immunoagents) interaction (immunointeraction), and the most common approach involves immobilizing one of the immunoagents on a substrate and then exposing the immobilized immunoagent with its corresponding immunoagent solution. The exposure leads to interaction and eventual formation of an antibody-antigen complex on the substrate. The detection process quantifies the complex formed on the substrate. To

simplify the quantification process, one of the immunoagents is attached with commonly used labels like radioactive markers, enzymes or fluorescent dyes.

The use of radioactive markers dates back to 1960 when Solomon Berson and Rosalyn Yalow successfully measured endogenous plasma insulin using radioisotope [50]. Even though the radioimmunoassay (RIA) technique was hugely popular, and earned Yalow the Nobel Prize in physiology and medicine in 1977, this technique required special facilities and there was great concern regarding the safety of laboratory personnel when handling radioactive waste. Alternatives were explored, and in the early 1970s, the idea of using enzymes was put forth at ERIAC (European RadioImmunoAssay Club). Peter Perlmann and Eva Engvall conceptualized and later developed the enzyme-linked immunosorbent assay (ELISA) technique, publishing their first paper in 1971 that demonstrated the quantitative measurement of IgG in rabbit serum with alkali phosphatase [51]. Today, ELISA is the most commonly used enzyme immunoassay technique with different schemes. The direct ELISA technique is the simplest of schemes, whereas the ‘sandwich’ method and competitive binding method are the most widely used.

These conventional techniques however have several limitations. To begin, they require a laboratory setup with a highly qualified technician who can execute the complex multistage process and analyze the results. The analysis can take several hours, making it unsuitable for applications where quick determination of analyte is required. Finally, equipment miniaturizing and measurement automation is difficult or impossible.

Progress in nanotechnology has made it possible to miniaturize many of the tools used in conventional immunoassay tools. There is immense interest and progress in

point-of-care diagnosis (POC). POC diagnostic tools employ *in vitro* diagnostic tests, which are tests that do not require any sample pre-preparation, a well-equipped laboratory setup or a skilled technician. At the heart of any POC system is a biosensor. The term ‘biosensor’ or ‘immunosensor’ is used for alternative immunoassay systems that overcome the limitations of conventional immunoassay techniques. These alternative systems are still based on the same basic principles of antigen-antibody interaction used in conventional assays, but as they are automated, they are more efficient, sensitive, and also faster than their conventional counterparts and have the ability to acquire data directly [52]. The biggest advantage of POC diagnosis is the short amount of time required to get an “answer”, as the result is available in seconds compared to hours [53].

9.2 Biosensors

Leland Clark was a pioneer in the development of the heart-lung machine. Clark was an experienced physiologist who, during a surgery, could correctly adjust the oxygen levels by visually judging the redness of the blood. In his attempt to automate the process of oxygenating blood circulation, he developed the oxygen sensor, or more commonly known as the Clark electrode. Later, while he was trying to calibrate the electrode (deoxygenating it) by adding small amounts of enzyme glucose oxidase, he realized he could use his device as a glucose sensor. In doing so, Clark had built the first ever biosensor. In 1992, at the World Congress on Biosensors in Geneva, Switzerland, he was honored with a special recognition of “Father of Biosensors” [54].

Lazcka *et al.* have managed to quote a source that defines a biosensor [48]. According to their source, “*Biosensors are analytical devices incorporating a biological*

material (e.g., tissue, microorganisms, organelles, cell receptors, enzymes, antibodies, nucleic acids, natural products, etc.), a biologically derived material (e.g., recombinant antibodies, engineered proteins, aptamers, etc.) or biomimic (e.g., synthetic catalysts, combinatorial ligands and imprinted polymers) intimately associated with or integrated within a physicochemical transducer or transducing microsystem, which may be optical, electrochemical, thermometric, piezoelectric, magnetic or micromechanical.” The basic block diagram of a biosensor is shown in Figure 9-2. In general, a biosensor is composed of two parts: a) a sensor system that allows interaction between biological elements, and b) a transducer that generates a signal employing principles of biological molecular recognition.. Most of the biosensors use three main biological elements for recognition, namely enzymes, antibodies and nucleic acids.

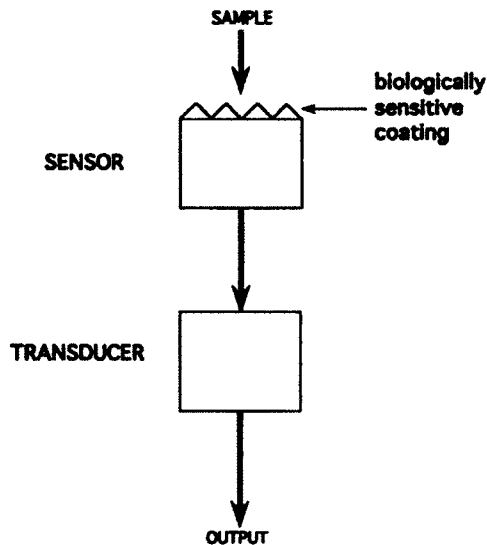


Figure 9-2: Basic block diagram of a biosensor [55].

Based on the transducing mechanism, biosensors can be classified as optical biosensors, gravimetric biosensors and electrochemical biosensors.

9.2.1 Optical Biosensors

The good selectivity and sensitivity of optical biosensors make them the most popular types of biosensors. While fluorescence detection is the most commonly used technique in optical biosensors, there are increasing numbers of optical biosensors based on other smart techniques such as surface plasmon resonance (SPR), and photonic crystal nanostructures.

Fluorescence detection has been used in conventional techniques like ELISA and PCR in which immunoagents are conjugated with fluorescent compounds. In fluorescent compounds, a valence electron can absorb light from an external excitation source and make a transition to an excited singlet state. When this electron returns to its ground state, it emits a photon (light) with lower energy (longer wavelength). There are many types of fluorescent markers, but the most commonly used is fluorescein isothiocyanate (FITC) and quantum dots that are increasing in popularity due to the fact that they produce stronger fluorescent signals and increased sensitivity. A technique based on the transfer of energy from donor fluorophore to an acceptor fluorophore, also called fluorescence resonance energy transfer (FRET), has been used to detect listeria and salmonella contamination in food [56]. Quantum dots are now being used in FRET since they make excellent donors [57].

When light (photon) is incident upon a solid or liquid, the electrons at the surface are set into oscillations, and Surface Plasmon occurs when the frequency of electron oscillation is equal to the frequency of incident photon. Under specific conditions, the incident photon couples with the surface plasmon to generate electromagnetic waves called Surface Plasmon Polaritons (SPP). The boundary of a metal-dielectric interface

can guide these electromagnetic waves over a very short distance ($< 100\text{-}200\text{ nm}$) before they lose their energy due to absorption in the metal or radiation into free space. These SPP are very sensitive to changes in thickness or refractive index along the path they travel near the boundary of the metal-dielectric interface. An SPR based biosensor measures this change in refractive index due to the adsorption of antigen-antibody [58].

It was Lord Rayleigh who first studied the propagation of electromagnetic waves in periodic media. In early 1887, he studied crystal structures that could prohibit light propagation through their planes. In 1987, researcher Eli Yablonovitch published a paper on his attempts to achieve threshold-less LASER by increasing reflective feedback levels into the light-emitting medium [59]. In the same year, researcher Sanjeev John published a paper where he was trying to localize light by using a periodically varying refractive index [60]. Later, they both realized that they were investigating the same type of structure, and Eli Yablonovitch coined the term *Photonic Crystals*. According to Eli Yablonovitch, to be called a photonic crystal, the crystal must satisfy two important criteria: *the structure has to have 2D or 3D periodic structure and the photonic band structures should have a high index of contrast (≥ 2)* [61]. Photons behave similarly to electrons in photonic crystals due to the presence of photonic band gap (PBG). Photonic crystals can block a range of photons; photonic band gap is the range of photon energy or frequency that cannot propagate through the photonic crystal. The fabrication of photonic crystals is complicated, but simpler techniques like using nano porous hydrogel to fabricate photonic crystal have been used to detect immunoglobulin G (IgG) antibody [62].

9.2.2 Gravimetric Biosensors

Gravimetric biosensors detect the change in mass following the antigen-antibody complex formation, and the most common approach to detect the change in mass is to use piezoelectric detectors. For a piezoelectric material, the resonance frequency changes when mass is added to the material. The relationship between resonance frequency change and the mass is given by Sauerbrey equation:

$$\Delta F = \frac{-2.3 \times 10^6 F_o^2 \Delta m}{A} \quad \text{Eq. 9-1}$$

Where ΔF is the change in resonant frequency in Hertz, F_o is the resonant frequency of the crystal in MHz, Δm is the mass deposited in grams and A is the area over which the mass is deposited [63].

These types of biosensors have been used to detect bacteria using probes modified with immobilized antibodies [64], [65]. The resonant frequency of the probe is then measured using a quartz crystal microbalance (QCM).

9.2.3 Electrochemical Biosensors

As mentioned earlier, optical biosensors are the most commonly used biosensors due to the fact that they have good sensitivity and selectivity; even conventional techniques like ELISA are based on optical detection and still remain very popular. Optical biosensors do suffer from several drawbacks, however, including bulky monochromators, light sources and detectors. The most important limiting factors are the minimum sample volume and the path length requirements that are set by the Lambert-Beer law to achieve certain performances [66].

Electrochemical biosensors come across as the most promising alternatives to these optical biosensors and are more common in monitoring and the diagnostic test in

clinical analysis. Advancements in micro and nano scale fabrication make it possible to miniaturize the electronics involved in electrochemical biosensors, leading to lower-cost, better multiplexing, and to the possibility of high-throughput analysis while using very small volumes of samples. The biggest advantage that electrochemical sensors have over optical counterparts is the fact that the volume of the sample does not affect the sensitivity of the electrochemical sensors.

Any electrochemical biosensor is designed to detect the changes in electron (charge) transfer (either voltage or current changes) when immunoagents interact. Depending on the parameter detected, these sensors are classified as: amperometric (current), potentiometric (constant voltage), or impedimetric (alternating voltage/impedance).

9.2.3.1 Amperometric Electrochemical Biosensors

Detecting the current is the most commonly used technique in electrochemical sensors. The sensors are biased such that the immunointeraction produces a current directly or indirectly, and usually the linear relationship between the current and the analyte concentration is known. Based on the known linear relationship, the concentration can be directly evaluated from the measured current. There are certain situations where the immunointeraction will not produce any charge transfer. In such cases, redox mediators are introduced that are able to reversibly exchange charge between the sensor and immunoagents [67], [68].

9.2.3.2 Potentiometric Electrochemical Biosensors

These sensors monitor the change in potential at the working electrode with respect to a reference electrode. The field-effect is the dominant technique used in these

sensors. Traditionally, an ion-sensitive field effect transistor (ISFET) involved using a reference electrode to detect biological elements, but there is a very useful variation of ISFET utilizing the semiconductor field-effect for detection [69]. The application of these types of electrochemical biosensors was not very common in the past and there are certain problems associated with these devices that limit the growth. The biggest challenges involved in using these sensors are a) fabrication and packaging, b) poor reproducibility, c) poor detection limits, and d) poor device stability.

9.2.3.3 Impedimetric Electrochemical Biosensors

Impedimetric technique is more commonly known as electrochemical impedance spectroscopy (EIS). The commonly used structure makes use of interdigitated electrode array structure as shown in Figure 9-3. The detection technique involves applying a small voltage across two electrodes and sweeping the frequency while simultaneously recording the impedance (conductance). Since the impedance is a complex function of frequency, it is easier to detect any change in dielectric constant due to the formation of complexes after the immunointeraction. The main advantage of these sensors is they do not need any kind of labels as compared to other electrochemical sensors that need labels. The label free approach makes these sensors suitable for rapid detection of foodborne pathogenic bacteria [70], [71]. However, the detection limits for these sensors are poor when compared to other traditional techniques [48].

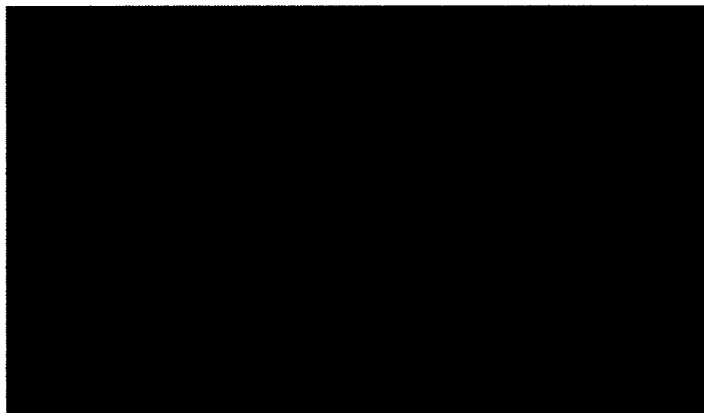


Figure 9-3: An interdigitated electrode (IDE) array.

9.3 Nanotechnology and Biosensors

Nanotechnology is a multidisciplinary field that involves studying, creating and manipulating materials to develop devices and systems. Typically, at least one dimension of the nanomaterial and nanostructure is in the range of 1-100 nm. These novel nanomaterials and nanostructures display unique physical and chemical properties due to quantum size effect, surface effect, and quantum-tunnel effect. Fundamental concepts in condensed matter physics drive the developments in artificial inorganic nanostructures. It was Leo Esaki who first introduced the concept of ‘artificial solid’ when he developed novel semiconductor quantum devices, in which the tunneling of electrons could be systematically controlled [72]. In 1973, Esaki was awarded the Nobel Prize in Physics. The quantum mechanical scattering of the valence electrons by the atoms is responsible for the electronic and optical properties of a semiconductor. In the first artificial solids, the semiconductor atoms were arranged in a specific way to create artificial ‘quantum wells’; electrons passing through this potential were then scattered along the designed path. The quantum wells make it possible to control the spacing between the electronic

energy levels systematically by adjusting the length scale over which the potential varies, compared to the electron wavelength [73].

The use of nanomaterials and/or nanostructures in biosensors is opening up new ways for signal transduction, and allowing for rapid analysis of multiple substances. In one-dimensional nanostructures, every atom in the structure is a surface atom, which offers maximum surface-to-volume ratio. This is a major advantage, and when these 1D nanostructures are used in the biosensors, the high surface-to-volume ratio contributes to an increase in sensitivity [74]. Another key advantage of using nanostructures is the possibility to integrate a large number of devices on a single small chip [75]. Here is a brief review of the different kinds of nanostructures used in the biosensors.

9.3.1 Nanoparticles

As discussed in Section 9.2.1, quantum dots have been used as replacements for conventional fluorophores in optical biosensors because they can produce stronger fluorescent signal and increase the sensitivity. Quantum dots are also a good choice for newer optical techniques like FRET. A thin layer of gold nanoparticles coated on the nano pore structure of a Fabry-Perot interferometer significantly enhances the optical signal due to the localized surface plasmon resonance effect [58]. Gold nanoparticles can also be used as fluorescence quenchers (energy acceptor) in an optical biosensor to detect specific DNA sequences [76]. Colloidal gold has more surface area, and when used in an electrochemical DNA biosensor, it enhances the amount of immobilized DNA, which in turn lowers the detection limit of the biosensor [77]. Cell separation techniques use magnetic nanoparticles to label the cells, and then by applying magnetic field gradients, cells can be isolated and manipulated [78]. Paramagnetic particles make an interesting

choice in immunoassay techniques. These particles do not require chemical or electromagnetic stimulations, and they can cause perturbation in the applied magnetic field that can be easily detected with suitable electronics [79].

9.3.2 Nanowires

Nanowires can be classified as metallic or semiconducting. Nanowires exhibit highly reproducible electrical [80], [81] and optical properties [73], and hence, provide unique opportunities to develop novel biosensors. Metallic nanowires can be grown in porous alumina templates [82], [83]. Semiconducting nanowires can be grown either using the top-down approach or the bottom-up approach [84]–[86]. Among semiconducting nanowires, silicon nanowires are more commonly used since they are easier to fabricate. Existing technologies used to fabricate microelectronics are all based on silicon and can be easily applied in the fabrication of silicon nanowires. Other semiconducting nanowires made out of ZnO also show the ability to detect bio molecular interactions [87]. The high surface-to-volume ratio of silicon nanowires has helped to achieve very low detection limits [88], [89]. Another advantage of using nanowire is the label-free nature of the electrical detection. In most cases, the analyte molecule is directly detected on the surface of the nanowire through sensitive molecular interaction and no label is required [90], [91].

9.3.3 Carbon Derived Nanostructures

Carbon nanotube (CNT) and diamond are two widely employed carbon polymorphs in fabricating electrodes for electrochemical sensors [92]. Depending on the structure, CNTs can be classified as single-wall carbon-nanotubes (SWNTs) and multi-wall carbon-nanotubes (MWNTs). Since every atom in a CNT is a surface atom, they

form an ideal class of 1D nanostructures that could exhibit ideal sensitivity at the single molecule level [46]. Transfer of charge from one electrode to another is a very important aspect in any electrochemical reaction, and it has been shown that CNTs promote electron-transfer reactions of proteins [47].

The biggest hurdle in using CNT for biosensors is the process involved in assembling the nanostructure into the sensor. The commonly used technique involves dispersing nanotubes in an aqueous or organic solution and then depositing them on a substrate. The contact electrodes are then created using electron-beam lithography. Even though this assembly technique is simple, the process of creating contacts is very random and yields a very low throughput. One of the strategies used to tackle this problem is based on AC dielectrophoresis. Single CNT or a bundle of CNTs can be aligned between a pair of contact electrodes by controlling the time, voltage, and frequency of the applied AC voltage [93]. Another alternative is to use catalyst seeds at predefined locations [94]. However, there is still no established standard process to the assembly of single CNT. Instead, it is easier to produce a network of carbon nanotubes (thin film) that involves the use of chemical vapor deposition (CVD) and does not require any catalyst seed. A network of CNT has been used in label-free detection of DNA hybridization [95]. The sensitivity of these devices is lower due to an increased number of CNTs, but it is possible to produce devices on a large scale [46].

The excellent biocompatibility, low background current, wide potential window, and good chemical stability make the diamond the best known electrochemical transducer [96]–[98]. A diamond is chemically inert and shows the strongest bonding stability to DNA [99]. Even though a diamond possesses all these excellent properties, it has

struggled to expand its applications in life sciences, the primary reason being the high costs of production and refinement [92].

9.4 Carbon Nanotube

Polymorphism, or allotropy, is a characteristic of a material that can have more than one crystal structure. Carbon has three important crystalline allotropes: diamond, graphite and buckminsterfullerene. Diamond and graphite were the best-known allotropes of carbon until 1985 when buckminsterfullerene (called the ‘buckyball’) was discovered by Robert F. Curl, Harold W. Kroto and Richard E. Smalley [100]. They were awarded The Nobel Prize in Chemistry in 1996. The buckminsterfullerene molecule has a total of 60 carbon atoms (also known as C_{60}) and can be imagined as a soccer ball, with each vertex on the seam replaced by a carbon atom as shown in Figure 9-4.

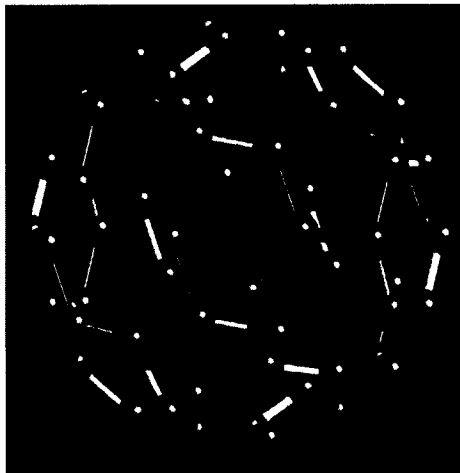


Figure 9-4: A buckyball structure with carbon atoms at every vertex of an imagined soccer ball. The red lines indicate single bond and yellow lines indicate double bond [102].

The buckminsterfullerene crystal is a semiconductor and it exhibits superconductivity when it forms a compound with alkali metals at low temperatures.

Along with diamond, graphite and fullerene crystals, carbon also exists in other crystalline forms and structure. Amorphous carbon has no crystal structure, but it is defined as a structural allotrope. Carbon nanotube is another such structural allotrope of carbon that was discovered in 1991 by Iijima [101]. The structural allotropy in carbon is related directly to the different hybridization that carbon atoms can assume. A diamond is formed when the four valence electrons are shared equally (sp^3 hybridization).

In graphite, three electrons are equally shared (sp^2 hybridization) and the fourth electron is allowed to remain delocalized among all atoms. The sp^2 hybridization results in a structure that has strong in-plane bonds and weak out-of-plane bonds; this is the reason why graphite can slide along the planes and is considered a soft material.

Fullerenes and nanotube structures of carbon are also formed due to sp^2 hybridization. Under normal ranges of pressure, bulk graphite is thermodynamically stable even at high temperatures, but its behavior changes when the size of the crystal is very small. For a very small size, the number of carbon atoms is finite and the density of dangling bond atoms is high. To become energetically stable, these atoms close onto each other to remove the dangling bonds. When the number of carbon atoms is less than a few hundred, the structures formed correspond to linear chain, rings and closed shells (fullerenes) [100].

9.4.1 Structure of Carbon Nanotube

According to Euler's principle, one needs exactly 12 pentagons to close a hexagonal lattice completely with a topological curvature; hence, for a buckminsterfullerene (C_{60}) molecule, there are always 12 pentagons and many hexagons (C_{2n} has $n-10$ hexagons). Carbon nanotubes are greatly elongated fullerenes and can be

produced with 12 pentagons and millions of hexagons. As shown in Figure 9-5, a carbon nanotube (CNT) is a long cylinder made of the hexagonal lattice of carbon bound by two half-hemispherical fullerenes at the ends. The diameter of the tube will depend on the size of the half-hemispherical fullerene. The cylindrical open-ended structure of the tube can be conceptualized as rolling a sheet of graphene (single layer of graphite) to form a seamless match between the open edges. On the curved surface of the tube, the hexagonal arrays of carbon atoms wind around in a helical fashion introducing helicity to the structure. To close the ends of the tube, pentagons are nucleated at some stage in the growth process.

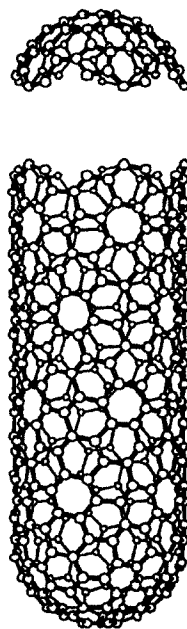


Figure 9-5: The basic cylindrical structure of a carbon nanotube with both ends closed by semi-hemispherical buckyball [103].

There are two structural variations found in nanotubes. The first, called the multi-walled carbon nanotube (MWNT) were discovered first and are made of concentric cylinders placed around a common central hollow. The diameters of these tubes vary

from 2 to 25 nm, and the distance between each cylinder is 0.34 nm. The second, called the single-walled carbon nanotube (SWNT), are single-layer cylinders extending from end to end with diameters from 1-2 nm [92]. Rolling a graphene sheet into a carbon nanotube can be done in several ways as long as the dangling bonds on both edges are matched. This process introduces chirality in carbon nanotubes, and a lattice vector C_h uniquely specifies the fiber diameter and chirality

$$C_h = n_1 a_1 + n_2 a_2 \equiv (n_1, n_2). \quad \text{Eq. 9-2}$$

Where n_1, n_2 are integers and a_1, a_2 are the unit vectors. To understand chirality, let us consider the scenario depicted in Figure 9-6.

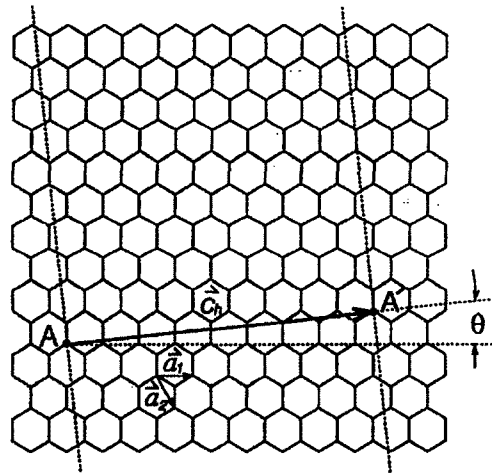


Figure 9-6: A carbon nanotube formed by rolling a sheet of graphene. The chiral angle is denoted by θ , a_1 and a_2 are the graphene unit vectors [103].

The chiral vector C_h connects two sites A and A' on the one-dimensional graphene crystal. Connecting together points A and A' form the nanotube and the lightly dotted lines that are perpendicular to C_h show the cylinder joint. If $a = 1.42 \times \sqrt{3} \text{ \AA}$ is the lattice constant, the fiber diameter d is then defined by

$$d = \frac{|C_h|}{\pi} = \frac{a\sqrt{n_1^2 + n_1n_2 + n_2^2}}{\pi}, \quad \text{Eq. 9-3}$$

therefore the chiral angle that defines the direction of the lattice vector is given by

$$\theta = \arctan \left[\frac{-\sqrt{3}n_2}{(2n_1 + n_2)} \right]. \quad \text{Eq. 9-4}$$

The lattice vector C_h offers a range of orientation for carbon nanotubes ranging from zigzag direction [$\theta = 0^\circ$ or $(n, 0)$] to armchair direction [$\theta = \pm 30^\circ$ or (n, n)] and hence these nanotubes are called zigzag nanotubes and armchair nanotubes, respectively, in Figure 9-7. All the other types of nanotubes are simply referred to as chiral nanotubes.

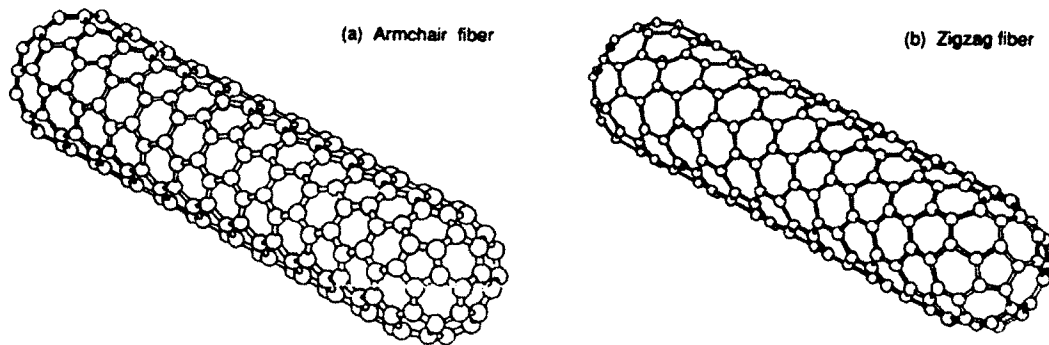


Figure 9-7: Arrangement of carbon atoms in armchair carbon nanotube (left) and zigzag carbon nanotube (right) [104].

9.4.2 Electronic Structure of Carbon Nanotube

CNTs have unique electrical properties due to their chirality. Armchair nanotubes are metallic, whereas the zigzag and chiral nanotubes are either metallic or semiconducting [103]–[105]. Figure 9-8 shows how the unit vectors can be configured to create a metallic or semiconducting nanotube.

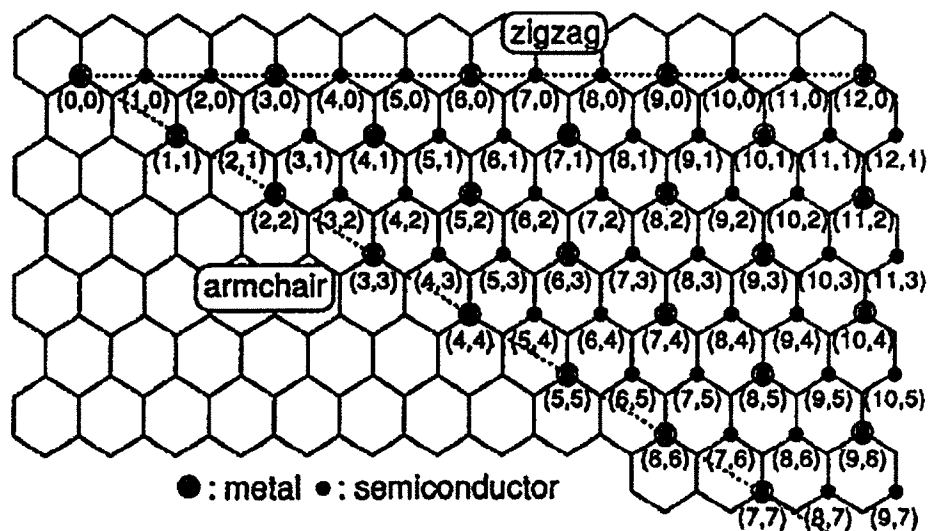


Figure 9-8: Possible vectors for chiral nanotubes. Circled dots and dots represent metallic and semiconducting nanotube respectively [103].

The interesting properties of CNTs are associated to their 1D shape along with sp^2 and π bonding between the carbon atoms. In graphite, the electronic bands are formed because the π electrons between two adjacent layers are free to move between the bonds. The finite tube circumference of carbon nanotubes restricts the number of possible electron states and a band gap opens up at the Fermi energy. The density of states represented as unit of states per unit cell of 2D graphite for two different zigzag nanotubes $(n_1, n_2) = (10, 0)$ and $(9, 0)$ is shown in Figure 9-9.

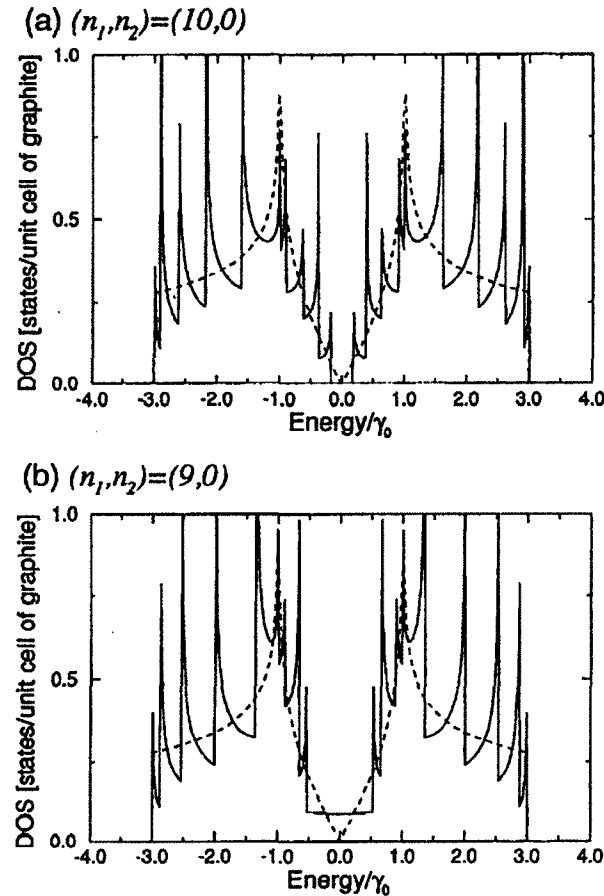


Figure 9-9: Density of states for a) zigzag nanotube (10, 0) and b) zigzag nanotube (9, 0). The dotted line shows density of states of 2D graphite [103].

The singularity arising due to 1D structure is apparent at the edge of every energy level. For the nanotube with $n_1 = 10$, there is an energy gap at the Fermi Level ($E=0$), but for the nanotube with $n_1 = 9$ there are finite density of states. This shows that metallic and semiconducting nanotubes can be fabricated by just changing the diameter of the tube.

The condition for the nanotube to be metallic is

$$2n_1 + n_2 = 3q, \quad \text{Eq. 9-5}$$

where q is an integer.

The relationship between the band gap (E_g) and the diameter of a semiconducting CNT is given by

$$E_g = \frac{1}{R}. \quad \text{Eq. 9-6}$$

For metallic CNTs ($n_1 \neq n_2$) there exists a second band gap. This band gap is related to the diameter of the tube as follows [106]:

$$E_g = \frac{1}{R^2}. \quad \text{Eq. 9-7}$$

The resistivity of a material depends on the number of charge carriers and the scattering these charge carriers experience inside the crystal. In well-fabricated carbon nanotubes, the electrons can travel over distances of up to several micrometers without getting scattered (ballistic transport) [107], [108]. When carbon nanotubes are integrated into the devices, the contact resistance between the tube and the metal electrode becomes very important. The work function variation from one metal to another is very large; depending on the type of metal used, the contact resistance shows different behavior. Metals like Ti and Pd lead to p-type conducting behavior, while Mg contact electrodes show ambipolar characteristics. Contacts made out of Ca mostly show n-type conduction behavior. The values of contact resistance can be calculated theoretically using the first principle; these calculations show that contacts made out of Ti have the lowest resistance with CNTs followed by Pd, Pt, Cu, and Au.

9.5 Carbon Nanotube Based Immunosensor

An immunosensor is a special type of biosensor that exclusively monitors the antibody-antigen interaction [109]. An immunosensor can be a direct or an indirect type of sensor. In a direct immunosensor, there is a direct detection of the antibody-antigen

reaction with or without the use of labels. For an indirect immunosensor, the biological reaction takes place in a reaction tube and a sensor measures the product of that reaction. Carbon based biosensors are commonly used because of their low cost, good electron transfer kinetics and biocompatibility. Carbon nanotubes display high mechanical strength, chemical stability and electrical conductivity, which make them ideal for use in the sensors.

The electrochemical signal generated from an antigen-antibody interaction in a CNT based immunosensor can be detected in two ways [110]. The first strategy is based on building a CNT based field-effect transistor (FET). The typical procedure involves binding the antibody to the CNT and then allowing the antigen to interact with the antibody. The electrochemical signal generated due to the antigen-antibody interaction changes the electric field, which in turn modulates the drain current of the transistor. The second approach is an indirect detection method where, just like the first strategy, an antibody is attached to the CNT and the antigen, then binds to the antibody. The CNT is then exposed to a second antibody that has a tag that is either redox active or can facilitate electrochemiluminescence. The label-free approach of the first strategy is more appealing and extensively utilized in modern biosensors.

9.5.1 Field-Effect Transistor (FET) Based Immunosensor

The use of silicon as a substrate in electrophysiological measurements was started in the late sixties at Stanford University [111]. In 1970, Bergveld introduced the idea of a solid-state device that could measure ion-concentrations in electrochemical and biological environments [112]. Besides measuring the electrical potential, this device could measure the ion concentrations, and it was called an ion sensitive field effect

transistor (ISFET). The ISFET is a special type of MOSFET. As shown in Figure 9-10 instead of a conventional gate found in a MOSFET, the gate in an ISFET is a reference electrode that is inserted in an aqueous solution that is in contact with the gate oxide.

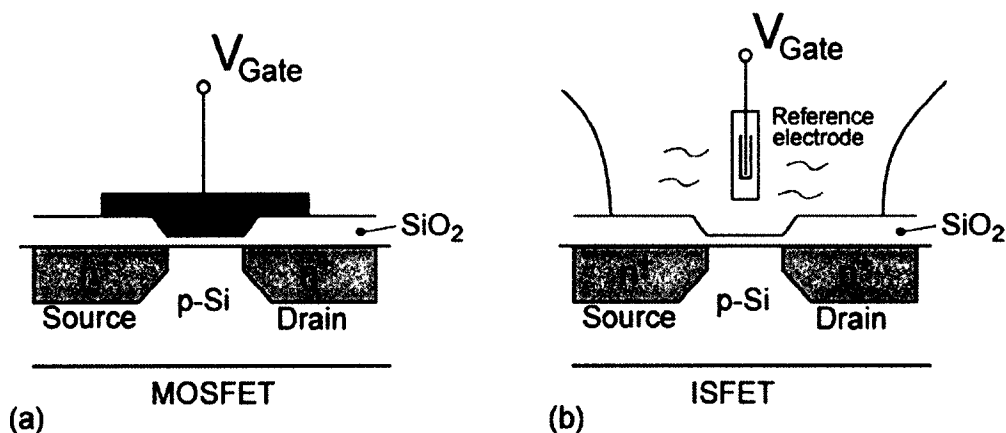


Figure 9-10: Construction of a) conventional MOSFET and b) ISFET proposed by Bergveld [113].

The ISFET became popular after its invention in 1970, so much so that in the next thirty years it accounted for more than 600 papers on the subject and inspired the development of many other devices, such as EnzymeFET (ENFETs), ImmunoFETs (IMFETs), etc. [113].

After the discovery of CNT in 1991, the semiconducting and metallic nature of CNT was extensively studied in the early 90s. The field-effect behavior in CNT was first reported from a metallic CNT operated at very low temperatures [114], whereas the first transistor fabricated with a single semiconducting CNT operating at room temperature was reported later in 1998 [115]. The ability of this transistor to operate at room temperature opened the door for various applications in the following years. The first CNT based transistor reported by Tans *et al.* is shown in Figure 9-11. The gate is a silicon wafer with a 300 nm thick layer of silicon oxide. The single semiconducting CNT

between the two Pt electrodes was produced by condensation of laser-vaporized carbon-nickel-cobalt mixture at 1200° C [116].

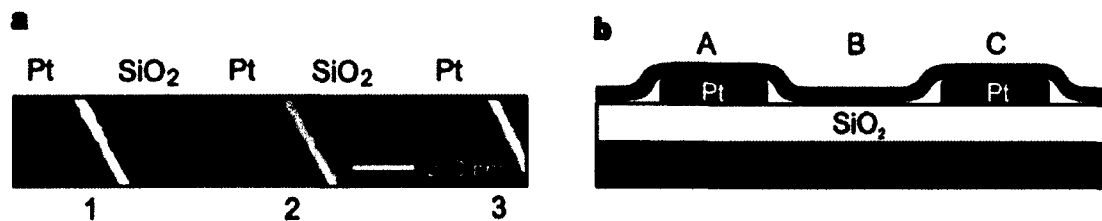


Figure 9-11: a) AFM image of single CNT on top of three Pt electrodes b) schematic side view of the transistor [115].

A detailed study of CNT based FET revealed the transport in CNTs is dominated by holes at room temperature and the transistor exhibits p-type behavior [117]. To get the output characteristic, the source-drain voltage was swept from -200 mV to +200 mV with gate voltages of $V_g = -6, 0, 1, 2, 3, 4, 5,$ and 6 V. The output characteristic is shown in Figure 9-12a. The transfer characteristic was obtained by sweeping the gate voltage and incrementing the drain-source voltage from 10-100 mV in the steps of 10 mV. As shown in Figure 9-12b, the conductance of the transistor can be modulated with the gate electrode. This study suggested that the SWNCT-FET behaved liked an ordinary FET, but it was later proven that it is the Schottky barriers at the CNT-metal contacts that play a central role in modulating the conductance of the transistor [118]–[120].

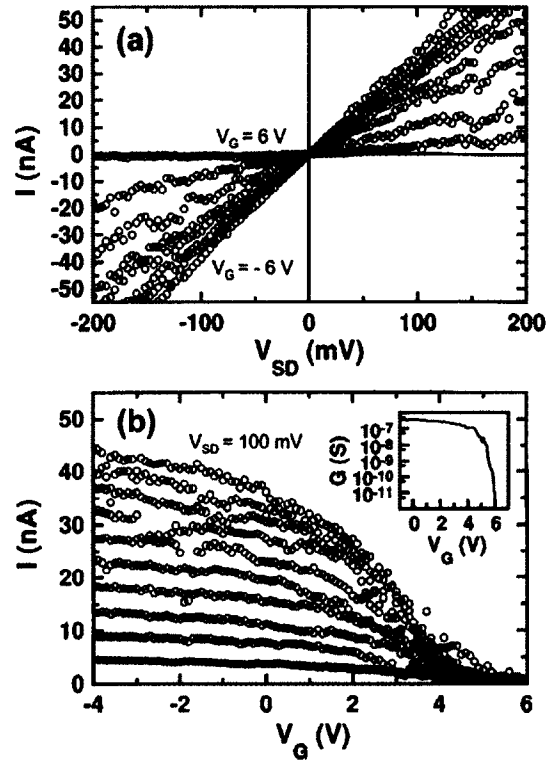


Figure 9-12: a) Output characteristic and b) transfer characteristic of SWCNT-FET [117].

A Schottky barrier, as shown in Figure 9-13, is a potential energy barrier created when a metal and semiconductor are brought in contact. The Schottky barrier height, Φ_B , is the difference between the interfacial conduction band edge E_C and Fermi level E_F . The metal-semiconductor contact can behave as a rectifier (electrons flow only in one direction) or as a resistor (electrons can flow in both directions) depending on the barrier's height. If the barrier is high enough, a depletion region is formed and the contact is a rectifying type, whereas if the barrier is low, the contact is ohmic (acts as a resistor). At the start of the century, it was demonstrated that the surface adsorption of various molecules and the change in their electrostatic charges vary the conductance of a

nanotube significantly [121]–[123]. This opened up the avenue for using SWCNT-FET for biomolecule detection.

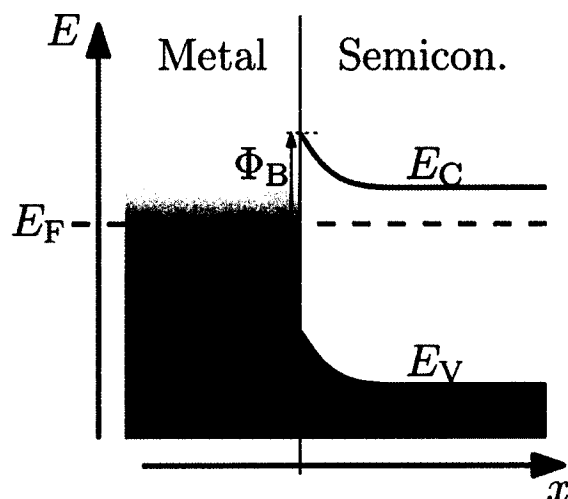


Figure 9-13: Formation of Schottky barrier at metal-semiconductor junction for zero bias [124].

9.5.2 Sensing Mechanism in SWCNT-FET Based Immunosensor

The exact sensing mechanism in SWCNT-FET based immunosensor was a topic of debate [125]. The initial work on SWCNT-FET as an immunosensor included detection of protein A and biotin-streptavidin [126], [127], and it suggested the conductance of the CNT transistor changed due to the electrostatic gating. The various functional groups present in proteins lend them surface charges, and these charges exert electrostatic gating to alter the carrier density in the nanotubes [126]. A more detailed study later suggested that the region near the edge of the nanotube-metal contact (Schottky Barrier effect) was the dominant sensing region and was more sensitive to charge on the absorbed protein [128]. An ultrasensitive immunosensor fabricated by modifying the geometry of CNT-metal contact is capable of detecting proteins as low as 1 pM [129].

Work done on DNA sensors also suggests that the modulation of the Schottky barrier at the metal-CNT contact by efficient hybridization is the dominant sensing mechanism [130], [131]. However, Dekker *et al.* has concluded that the sensing in an SWNT-FET based immunosensor is dominated by a combination of electrostatic gating effect and Schottky barrier effect, where the electrostatic gating is more reliable along the bulk of the SWCNT [132]. To prove the electrostatic gating was more reproducible, they carried out experiments with two types of devices: one with the passivized CNT-metal contacts to eliminate the chance of Schottky barrier effect, and the other with non-passivized CNT-metal contacts, which allowed the Schottky barrier effect. The behavior of the device with non-passivized metal-SWCNT contact before and after the protein adsorption is shown in Figure 9-14. The electrostatic gating shifts the semiconducting bands downwards after protein adsorption (indicated by the red curve). The Schottky barrier effect alters the difference between the metal and SWCNT workfunctions.

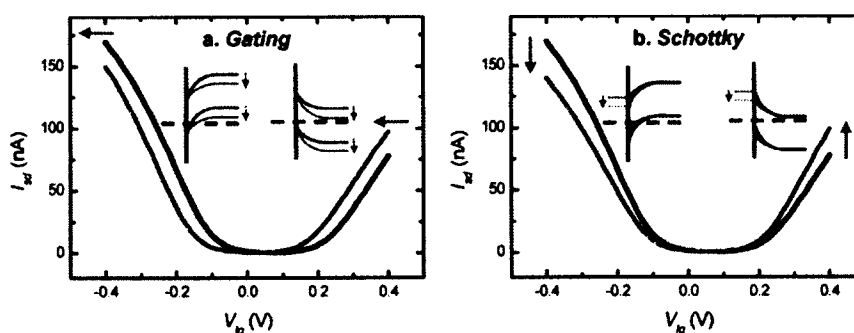


Figure 9-14: The black curve corresponds to device characteristic before protein adsorption and the red curve corresponds to the device characteristic after protein adsorption a) electrostatic gating effect b) Schottky barrier effect [132].

Since most of the biomolecules, including proteins, are suspended in physiological buffer solutions, the interface between the solution and the charged surface

of a sensor plays a vital role in detection [133], [134]. When a charged surface comes in contact with an ionic solution (electrolyte), the oppositely charged ions in the solution are attracted towards the surface-electrolyte interface and form an electrical double layer (EDL) as shown in Figure 9-15. The distance from the interface where the electrostatic field strength has dropped to $1/e$ of its initial value defines the thickness of this electrical double layer. This distance is also called the Debye screening length, κ^{-1} , and its value is

$$\kappa^{-1} = \sqrt{\frac{\epsilon_0 \epsilon k T}{2 q^2 I}}, \quad \text{Eq. 9-8}$$

where q is the elementary charge, k is the Boltzmann's constant, T is absolute temperature, ϵ_0 is the permittivity of vacuum, ϵ is the dielectric constant, and I represents the ionic strength. For 1-1 salt I can be replaced with the concentration of ion (c). For most of the physiologically relevant buffer solutions with ionic strength of ~ 100 mM, the Debye length κ^{-1} is around 1 nm and the surface potential is completely screened at a distance of a few nanometers away from the interface. So to successfully detect a protein adsorbed on the SWCNT surface, the dimensions of the protein have to be less than 1 nm. Normally, the dimensions of the proteins are much larger (around 10 nm), so to tackle this problem, most of the sensors based on SWCNT or nanowires are operated in buffers with low ionic strength (~ 1 nM to 10 mM) [80], [132], [135], [136].

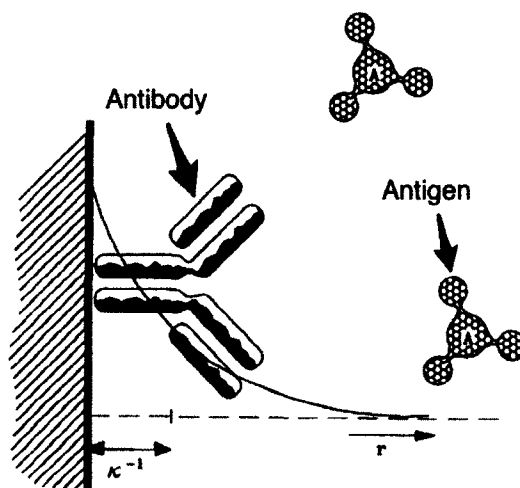


Figure 9-15: Schematic representation of electrical double-layer and the antibody adsorbed on the interface [137].

9.6 Protein Immobilization

Immobilization can be defined as the attachment of bio molecules to a surface, which results in the reduction or complete loss of mobility. To achieve good reproducible selectivity and sensitivity in an immunosensor, it is crucial that the antibody molecule is bound to the transducer surface in a highly controllable way and is oriented in a way that is optimal for the specific antigen binding without affecting its activity [138]. The orientation of the antibody should be such that the binding site of the protein is optimally accessible for the target antigen. The immobilization techniques are mainly based on the following three mechanisms: physical, covalent, and bio-affinity immobilization [139].

9.6.1 Physical Immobilization

Physical adsorption is the simplest and most inexpensive method to immobilize proteins. The adsorption occurs due to the weak interactions between a protein and the surface; factors like hydrogen bonds, electrostatic interactions, hydrophobic interactions, and Van der Waals interactions are responsible for adsorption. This technique is simple

and involves incubating the substrate in a protein solution followed by the rinsing off of the non-adsorbed protein. The drawbacks of this technique include random orientation and weak attachment as some buffers or detergents may wash off the protein during the assay.

9.6.2 Covalent Immobilization

A more robust way to immobilize proteins on the surface is by means of covalent bonds. This technique requires the presence of two mutually reactive chemical groups on the surface of the substrate and the protein. The functional group on the surface of the substrate is generated by chemical treatment and the covalent bonds are formed between the exposed side-chain functional groups of the protein and the modified surface substrate. Table 9-1 shows the required functional groups on the surface of the substrate corresponding to the available groups on the protein [139].

Table 9-1: Commonly available functional groups in proteins and functional groups required on the substrate surface.

Side groups	Amino acids	Functional groups required on the substrate surface
- NH ₂	Lys, hydroxyl-Lys	Carboxylic acid Active Ester (NHS) Epoxy Aldehyde
-SH	Cys	Maleimide Pyridyl disulfide Vinyl sulfone
-COOH	Asp, Glu	Amine
-OH	Ser, Thr	Epoxy

9.6.3 Bio-affinity Immobilization

This technique is based on complementary affinity interactions between biomolecules and generates a well-oriented and homogenous attachment of the antibody. It is also possible to detach proteins and make repeated use of the same surface. The commonly used techniques include Avidin-Biotin system, His-Tag system, DNA-directed immobilization, and Protein A/Protein G-mediated immobilization. The Protein A/Protein G-mediated immobilization relies on the specific interaction of the Protein A/Protein G with the Fc constant region of the Immunoglobulin G (IgG) molecule. The basic structure of IgG is shown in Figure 9-16. The first step in this technique is to immobilize the Protein A/Protein G covalently on the surface of the substrate. Next, the antibody (IgG) is introduced; the specific bio-affinity of Protein A/Protein G to the Fc region orients the IgG such that the binding sites of the IgG remain easily accessible for binding with the antigen.

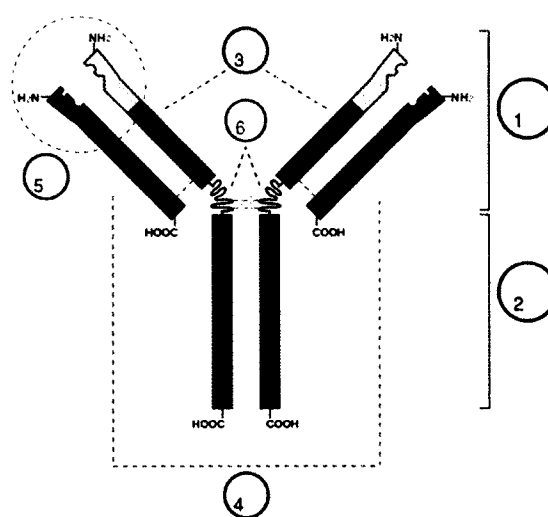


Figure 9-16: Structure of IgG where 1) Fab region, 2) Fc region, 3) heavy chain, 4) light chain, 5) antigen binding sites, 6) hinge regions [140].

9.7 Carbon Nanotube Thin Film

As discussed in Section 9.3.3, individual carbon nanotubes have a very large surface-to-volume ratio and can act as an ideal sensor. Every atom in the nanotube is on the surface acting as an individual sensing site; hence, it is possible to achieve single molecule detection. However, there are many challenges that prevent a carbon nanotube based sensor from operating at ideal levels [46]. One major challenge is to passivize the contacts of a sensor based on a single carbon nanotube. Contact passivation is critical for sensors to detect an analyte directly in a liquid. Sensing can be achieved without contact passivation, but then the response will be dominated by the receptors immobilized on the contacts [130], [131].

In most of the CNT based sensor prototypes, the contacts are passivized using E-beam lithography, but alternate techniques must be used to be competitive with conventional sensors. The length of a carbon nanotube becomes a limiting factor when techniques like photolithography or nano imprint are used. The high sensitivity of CNT based sensors is established on the fact that every atom of the single CNT acts as an individual sensing site. Normally, CNTs tend to form bundles, or networks, and the sensitivity can drop drastically if the sensor cannot be built out of a single CNT. Sensors based on a single CNT should be reusable to remain competitive.

Repeated use leads to accumulation of analyte species on the surface and produces drifts that affect the reproducibility of the sensor. One way to tackle this problem is to have some kind of on-site cleaning mechanism on the chip; the other easier approach is to use disposable chips. For sensors based on 1D structure like CNT, there are notable variations in device characteristics. Due to these variations, it is very

important to calibrate each sensor before use. It is thus a major challenge to develop a reusable CNT based sensor that can be calibrated easily before deployment in a real-life scenario. A thin film made out of carbon nanotubes can be a good alternative to overcoming most of these challenges while sacrificing only some of the sensitivity.

A carbon nanotube thin film (CNTF) can be regarded as a novel material that has a 2D network of randomly distributed CNTs [141]. This thin film can either be a 2D network of vertically oriented carbon nanotubes [142] or of a horizontally laid network of nanotubes. A CNTF is usually a mixture of metallic and semiconducting CNTs, which makes CNTFs exhibit semiconductor-metal transition with increasing film thickness [143], [144]. The semiconducting behavior of CNTF in thin film transistor and sensor applications is observed when the density of CNTs is closer to the percolation threshold [145], [146], [147]. Porosity in thicker CNTF (usually micrometer thick) is an advantage in fuel cells and battery applications [148], [149]. CNTF with intermediate thickness, ranging from 10-100 nm, shows high optical transparency and electrical conductivity [150].

9.7.1 Fabrication of CNTF

There are two broad categories of CNTF fabrication: Direct growth methods and solution-based coating methods.

9.7.1.1 Direct Growth

The three major methods to fabricate CNTs are: arc-discharge, laser ablation, and chemical vapor deposition (CVD). CVD is the most widely used method to grow CNTF with randomly distributed or aligned nanotubes. Aligned nanotubes are central in devices exhibiting high mobility, and they also make it possible to realize molecular electronics,

but these devices suffer from poor statistical reproducibility [141]. As compared to films made out of aligned nanotubes, CNTF made out of randomly distributed CNTs are more reproducible and hence can be used in more practical applications [151]. The high vacuum and high temperature involved in direct methods like CVD may not be compatible with many substrates that are being used in the emerging plastic electronics field. Direct methods like CVD are, however, able to produce tubes with fewer defects and better CNT-CNT contacts that can lead to highly conductive films.

9.7.1.2 Solution-based Deposition

Solution-based deposition methods offer several advantages over direct growth methods. These methods are carried out at low temperatures, do not require a high vacuum, and are compatible with a wide range of substrates. The quality of the thin film depends on several factors including CNT material quality, stability of CNT dispersion, adhesion quality, and stability on the substrate. Solution-based deposition is a two-step process: a) preparing a stable CNT dispersion and b) coating the dispersion on the substrate.

9.7.1.2.1 Stable CNT Dispersion

The biggest challenge in fabricating CNTF is to prepare a stable dispersion of CNTs. The large aspect ratio of CNTs results in strong Van der Waals forces, which cause them to stick together and form large bundles. There are four major dispersion methods used in CNTF production: a) use of surfactant, b) use of polymers, c) use of organic solvents and water to functionalize CNTs, and d) use of DNA, protein, and starch.

Using surfactant to disperse CNTs is the most commonly used dispersion method [152]. Any surfactant works by attaching its hydrophobic end to the CNT and pulling the CNT into a water-like solvent with its hydrophilic tail. A surfactant can be anionic (produce negative charge in water), cationic (produce positive charge in water) or nonionic (neutral in water). Triton X-100, sodium dodecyl sulfate (SDS), and sodium dodecylbenzene sulfonate (NaDDBS) are the most widely used surfactants [153].

Polymers are commonly used in applications which make use of CNT- polymer composites [154], [155]. They interact nondestructively with pristine CNTs and maintain their intrinsic properties. Polymers are not preferred in thin film applications due to their large size and difficulty to remove them after fabrication.

The biggest advantage of using organic solvents to disperse CNTs is the minimal amount of residue found in the final film. The Hansen solubility parameters define the dispersion state. There are two forces involved when using organic solvents: a) the attractive Van der Waals forces between CNTs and b) the interactions between the CNTs and the solvent. *Tour et al.* have found that the best solvents for dispersing CNTs are 1,2-dichlorobenzene, chloroform and N-methylpyrrolidinone [156].

Using DNA and proteins to disperse CNTs are common in biological applications. Dispersion of CNTs in water is highly desirable as it is environmentally friendly and biocompatible. One way to functionalize CNTs is to treat them with extreme acids that makes it possible to disperse CNTs in water [157].

9.7.1.2.2 Coating Methods

Once the stable CNT dispersion is made, the next significant challenge is to uniformly lay down the CNT dispersion on the substrate and dry the solution without

causing agglomeration. There are many methods that are used to achieve the uniform coating of CNTs on the substrate.

The Langmuir-Blodgett (LB) method, also known as “logs-on-a-river” concept is based on the hydrophobic nature of CNTs [158]. The first step in this method is to disperse the CNTs over the surface of the water; next, the substrate is dipped in the dispersion and withdrawn horizontally or vertically. This method requires a precise control over the process, or else the film is easily broken. The other disadvantage is the time required to achieve more than a monolayer.

The self-assembly (SA) method depends on the interaction between the CNTs and the substrate. CNTs will adhere to the surface depending on the chemical groups available on the surface of the substrate. The surface can be modified with chemicals or by creating local charges [159], [160]. The chemical functionalization can make use of either polar groups such as amino ($-\text{NH}_2$) or carboxyl ($-\text{COOH}$), or nonpolar groups like methyl ($-\text{CH}_3$) to modify the substrate. When such a functionalized pre-patterned substrate is immersed in the dispersion, the CNTs are attracted to the exposed groups on the patterns and self-assemble to produce the final pattern. One can also scale up the process by using this in conjunction with photolithography.

The electrophoretic deposition (EPD) method uses a DC electric field to deposit CNTs. In this method, a low DC electric field is applied to a conductive substrate that helps the CNTs to align themselves linearly and deposit on the electrode [161]. Another method that employs an electric field to deposit CNTs is Dielectrophoresis (DEP). DEP uses an AC electric field to deposit and separate CNTs at the same time [162].

The deposition methods used in the industry involve depositing the dispersion on the substrate, followed by controlled drying. There are several methods to deposit the solution on the substrate, which include Mayer Rod, Slot Die, and Gravure [163], [164].

9.7.2 Patterning Carbon Nanotube Thin Films

Most of the applications using CNTF require some kind of patterning on the films to get the desired geometry. For direct growth methods like CVD, a CNT film will grow only where the catalyst is deposited [165], [166]. So to get a patterned CNTF using direct growth, the catalyst must be strategically deposited at the patterned sites. Other methods including photolithography, inkjet printing, and micro contact printing can also be utilized to pattern the catalyst.

There are two types of solution-based pattern deposition methods: additive and subtractive. The additive methods are bottom-up approaches that use techniques like inkjet printing, patterned filtration, and microfluidic channel guided coating [167]–[169]. Subtractive methods are top-down approaches that use techniques like photolithography, or E-beam lithography, to print a pattern on the thin film, followed by plasma etching or laser ablation to remove the CNTs from the unprotected part of the film [170], [171]. Plasma of Ar, O₂, CF₄ or CF₆ can effectively etch carbon nanotubes. Another interesting technique to grow patterned thin films combines photolithography and layer-by-layer self-assembly [172]–[174]. The patterns are generated using the conventional photolithography approach; the substrate is then sequentially dipped into a solution containing charged CNTs, followed by a solution that has an opposite charge of the CNT solution.

The choice of patterning methods depends on the type of substrate, the desired resolution, and the cost. Subtractive methods, like plasma etching or laser ablation, yield higher throughput for large-scale device application. High-speed inkjet printing is a very promising additive technique for large area patterning.

9.7.3 Electronic Properties of Carbon Nanotube Thin Films

The CNT's are not aligned for most of the fabrication techniques used to create single-walled carbon nanotube thin film (SWCNTF). Due to the interconnected nature of CNT's within the film, a Schottky barrier is created at the junction between two CNTs. This lack of alignment and existence of a Schottky barrier can produce SWCNTF with a wide range of electrical conductivity. The electrical conductivity of pure (not functionalized) SWCNTF ranges from 12.5 S/cm [175] to ~10000 S/cm [176].

The conductivity of SWCNTF shows a strong dependence on the film's thickness and there is a sharp increase in conductivity beyond a certain thickness. This type of behavior is a characteristic of percolating network. The percolation threshold (p_c), the conductivity (σ), the critical exponent (β), and the concentration of conducting channels (p) are related as

$$\sigma \propto (p - p_c)^\beta. \quad \text{Eq. 9-9}$$

Bekyarova *et al.* demonstrated that, at room temperature, the conductivity data for their films fits directly to the film thickness (t) according to Eq. 9-9 [144]

$$\sigma_{RT} \approx (t - t_c)^\beta, \quad \text{Eq. 9-10}$$

where t and t_c are the film thickness and critical thickness (percolation thickness), respectively, and β is a critical exponent. They also found that for non-functionalized films, the conductivity saturates beyond a certain thickness. In their case, this thickness

was $t \approx 50$ nm. For non-covalently functionalized films, the conductivity was an order of magnitude lower than the non-functionalized films, whereas the conductivity of covalently functionalized films was two orders of magnitude lower than the non-functionalized films. They also observed the percolation threshold for functionalized films (both covalent and non-covalent) were higher compared to non-functionalized films. Functionalization introduces increased tunneling barriers between the SWCNTs, and according to percolation theory, the introduction of insulating substituents dilutes the concentration of the conducting pathways. This is the reason why the conductivity decreases and the percolation threshold increases for functionalized SWCNTF.

9.8 Layer-by-Layer Self-Assembly

The layer-by-layer (LBL) technique is a self-assembly process introduced in the early part of the 19th century to prepare polyelectrolyte multilayers [177], [178]. This bottom-up technique is based on the electrostatic adsorption of charged molecules or nanoparticles and can be used to achieve some unique geometries and functionalities [179]–[182]. The solution based molecules or nanoparticles can be assembled on any substrate, and the entire assembly process can be carried out in a normal laboratory setup.

A thin film of inorganic nanoparticles assembled by LBL technique is basically formed by alternate adsorption of a polyelectrolyte and the inorganic nanoparticle on the substrate. Every cycle in the assembly process to create one layer consists of two steps: incubation and rinse. As shown in Figure 9-17, the charged substrate is immersed into an oppositely charged polyelectrolyte solution and incubated for a certain time. The incubation is then followed by a deionized (DI) water rinse, and sometimes an additional drying step may be added. During the incubation step, the oppositely charged

polyelectrolyte electrostatically adsorbs on the substrate and modifies the original charge on the substrate, and the subsequent rinse removes the excess polyelectrolyte from the substrate. Often, to facilitate the production of thin film assembly, a precursor layer is assembled prior to the deposition of the inorganic nanoparticle. This precursor layer is composed of one or two bilayer of polyelectrolyte and plays a very vital role in the efficiency of the assembly and the time required to assemble the film with a desired thickness [183].

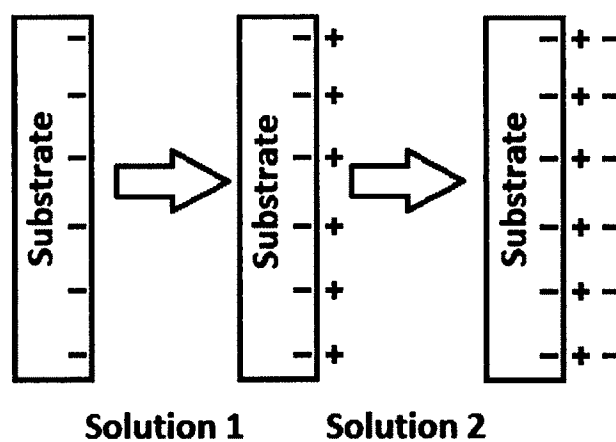


Figure 9-17: Schematic representation of electrostatic LBL assembly.

CHAPTER 10

FET BASED BIOSENSOR: DESIGN, MATERIALS, AND EQUIPMENT NEEDED FOR FABRICATION

10.1 Design

Two types of devices were fabricated as shown in Figure 10-1 and Figure 10-2. The type I device has three electrodes: source, drain, and gate, while the type II device has only two electrodes: source and drain. The type I device was fabricated to verify that the device exhibited a FET-like behavior, while the type II device was used to detect the biomolecules. Two masks are required to fabricate the type I device. The first mask is to pattern the source and drain contact electrodes on the silicon wafer, and the second mask is to pattern the channel between the two electrodes. The type II device utilizes both of the masks used in the fabrication of the type I device and requires an additional mask to fabricate the gate electrode. All three masks were first designed in AutoCAD and then converted to the proper GDSII format to feed into the mask writer.

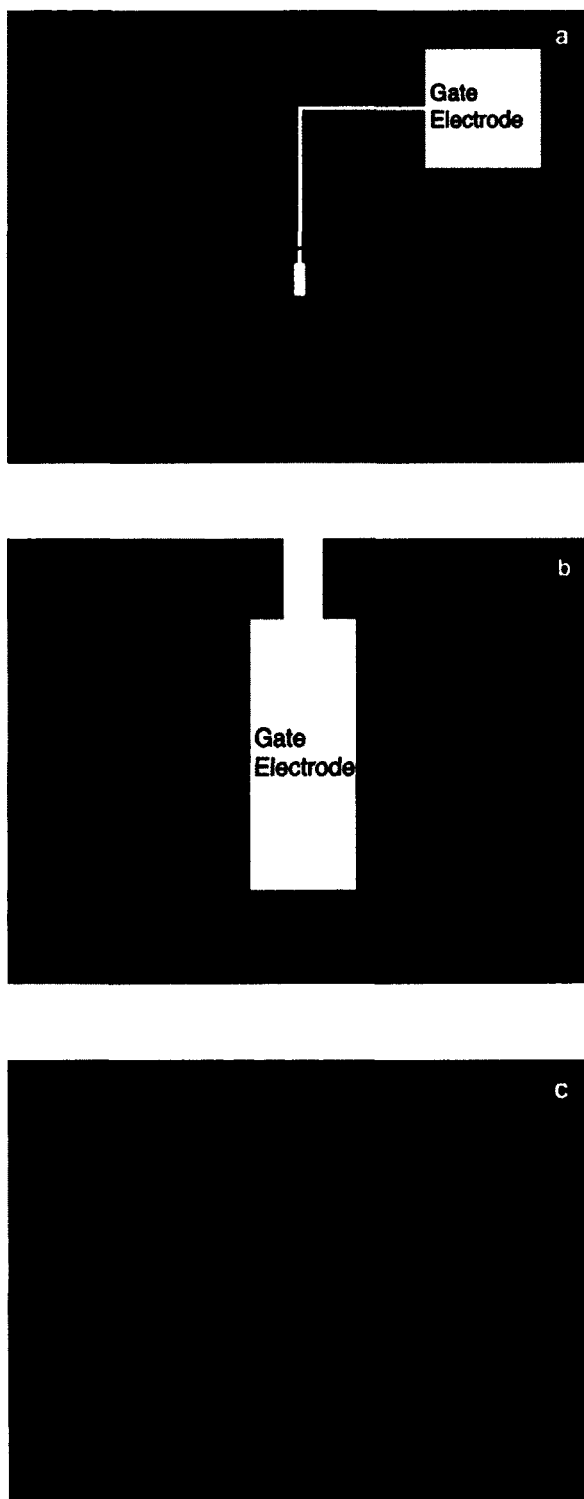


Figure 10-1: a) Schematic top view of type I device, blue circle highlights the channel region b) zoom-in view of the channel region highlighted by blue circle c) schematic top view of type II device. The CNTF in the channel is not shown here.

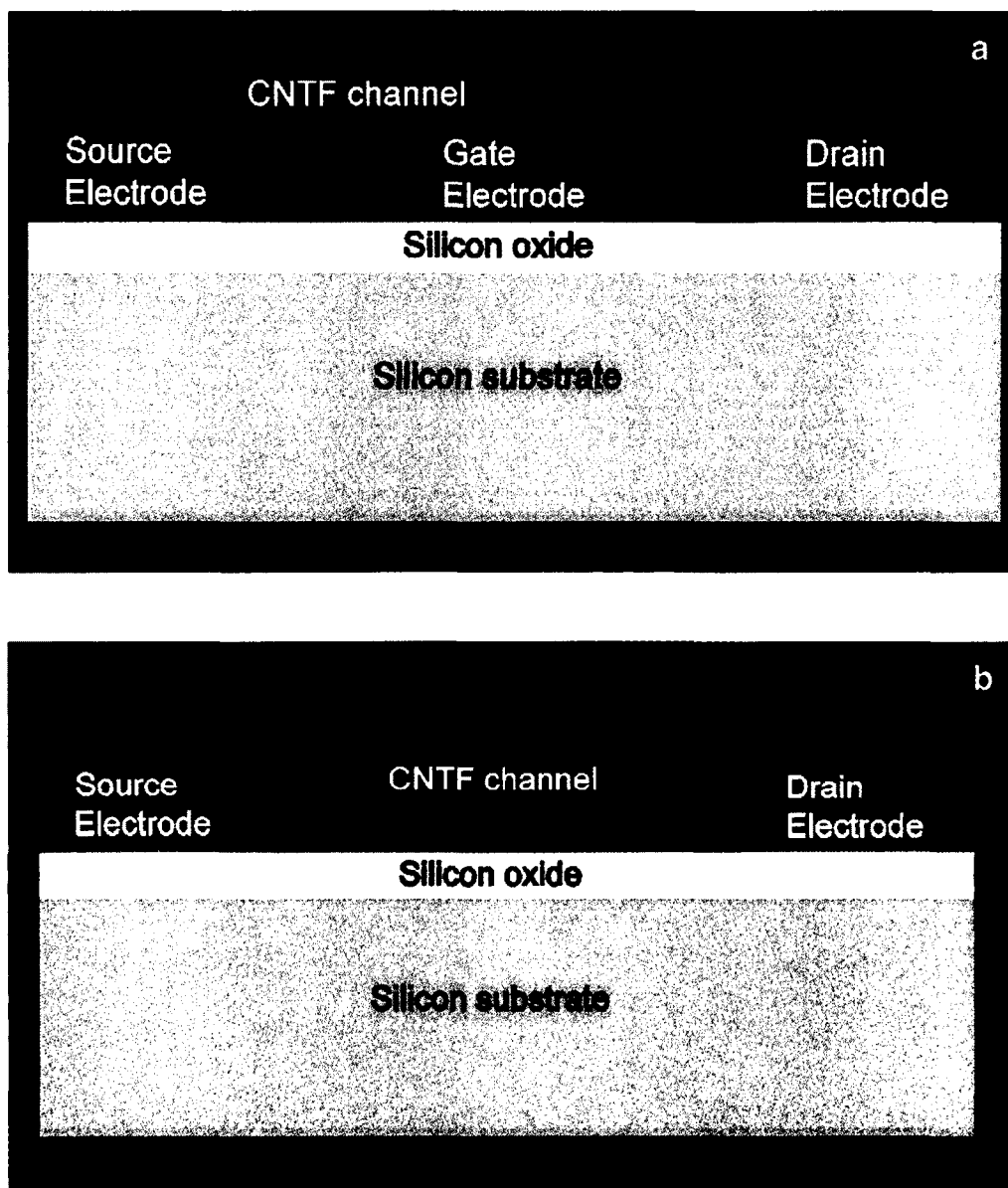


Figure 10-2: a) Schematic cross-sectional view of type I device and b) schematic cross-sectional view of type II device. The type I device has three electrodes: source, drain, and gate, while the type II device has only the source and drain electrodes.

10.2 Materials

The materials and equipment needed in this project are divided based on the research cycle: fabrication, characterization, and finally, biomolecule detection.

10.2.1 Materials Used for Fabrication

The device fabrication in this project uses photolithography techniques in conjunction with LBL self-assembly. The following is a list of wafer cleaning chemicals, photoresists, photoresist developer, and other chemicals used to fabricate the device.

10.2.1.1 Silicon Wafers

The silicon wafers were purchased from Silicon Valley Microelectronics, Inc. Some of the important wafer specifications are: diameter: 100+/-0.5 mm, orientation: <1-0-0>+/-1°, type/dopant: N/As, resistivity: 0.002-0.004 ohm-cm, and film: 2000 Å +/-5% thermal oxide.

10.2.1.2 Ammonium Hydroxide

Ammonium hydroxide assay 28-30 w/w% was purchased from Fisher Scientific.

10.2.1.3 Hydrogen Peroxide

Hydrogen peroxide, 30% solution, was purchased from EMD Millipore. Ammonium hydroxide and hydrogen peroxide were used to clean the organic impurities on the silicon wafer.

10.2.1.4 Shipley S1813

Shipley S1813 is a positive photoresist; upon exposure to light, the interaction between the molecules is weakened, which makes it easy to strip off the exposed resist with the help of a developer.

10.2.1.5 LOR 3B

Lift-off resist, LOR 3B, was purchased from MicroChem. LOR 3B when used in conjunction with a photoresist to create a bilayer can facilitate in a high-yield metal-lift off process.

10.2.1.6 MF-319

MF-319 was purchased from DOW Chemical. MF-319 is used to develop patterns exposed on Shipley 1813 photoresist; it is also capable of developing LOR 3B.

10.2.1.7 Remover PG

Remover PG was purchased from MicroChem. Remover PG is a solvent stripper designed to remove photoresists efficiently and completely. It was also used in the lift-off process as a lift-off solvent.

10.2.1.8 Nitric Acid

Nitric acid, ACS reagent 70%, was purchased from Sigma-Aldrich.

10.2.1.9 Sulphuric Acid

Sulphuric acid, ACS reagent 95-98%, was purchased from Sigma-Aldrich.

10.2.1.10 Membrane Filter

Membrane filter made of mixed cellulose ester and pore diameter 0.2 microns was purchased from Whatman GmbH. This filter was used to filter out the acid treated SWCNTs from the acidic solution.

10.2.1.11 SWCNTs Dispersion in DI Water

The SWCNTs were purchased from Carbon Solutions, Inc. A good dispersion of SWCNTs in DI water is very important for LBL assembly. To achieve this, 100 mg of these tubes were treated with a mixture of nitric acid and sulphuric acid (1:3 ratios) at 70° C for 30-45 minutes on a hot plate. The tubes were then filtered out from the acid mixture using a vacuum filtration setup with the membrane filter. The tubes were then further washed several times with DI water using the same vacuum filtration setup but changing the membrane filter. The filtered tubes were then added to 100 mL of DI water and

agitated in an ultra-sonic agitator for 1 hour to produce a final dispersion of 1 mg/mL. The pH of the final SWCNTs solution was adjusted to around eight by adding small volumes of diluted NH_4OH . The acid treatment functionalizes the SWCNT with a carboxyl group as shown in Figure 10-3, and imparts a negative charge on the tubes when dispersed in DI water. The charge on the SWCNT was measured using a zeta potential analyzer, and at $\text{pH} = 8$ the charge on the SWCNT was around -60 mV.

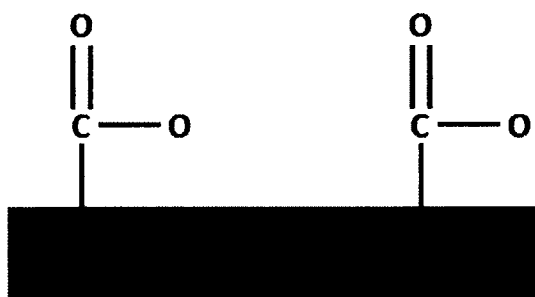


Figure 10-3: Functionalized SWCNT with carboxyl group [173].

10.2.1.12 Poly (diallyldimethyl ammonium chloride) solution

Poly (diallyldimethyl ammonium chloride) (PDDA) with structural formula as shown in Figure 10-4, average M_w 200,000-350,000 (medium molecular weight), 20 wt. % in H_2O was purchased from Sigma-Aldrich. PDDA acts as the polycation needed during LBL self-assembly.

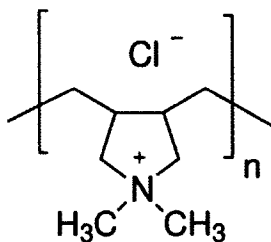


Figure 10-4: Structural formula for PDDA [184].

10.2.1.13 Poly (sodium 4-styrenesulfonate)

Poly (sodium 4-styrenesulfonate) (PSS) powder with structural formula as shown in Figure 10-5, average Mw ~70,000, was purchased from Sigma-Aldrich. PSS acts as the polyanion in LBL assembly.

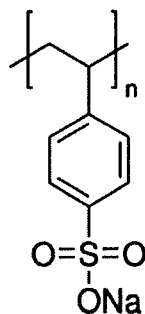


Figure 10-5: Structural formula for PSS [185].

10.2.1.14 Sodium Chloride

Sodium chloride was purchased from Sigma Aldrich. When NaCl is added to PSS, it helps to shorten the recovery regime during LBL self-assembly [183].

10.2.1.15 Other Chemicals

Acetone and Isopropyl alcohol are used to strip-off resist debris at the end of the metal lift-off process and LBL assembly. Deionized (DI) water is used for rinsing the wafer at various times during the entire fabrication.

10.2.2 Materials Needed for Biomolecule Detection

10.2.2.1 1-Ethyl-3-[3-dimethylaminopropyl]carbodiimide hydrochloride (EDC)

EDC is a water-soluble zero-length carbodiimide cross-linker that activates carboxyl groups for spontaneous reaction with primary amines and facilitates the coupling between them. EDC reacts with a carboxyl to form an amine-reactive *O*-acylisourea intermediate, but if this intermediate does not encounter an amine, it will

hydrolyze and regenerate the carboxyl group. EDC was purchased from Thermo Scientific, and 10 mg of EDC was added to 1 mL of DI water.

10.2.2.2 Protein A

Protein A is a protein found in the cell wall of the bacterium *Staphylococcus aureus*. Protein A binds to immunoglobulin G (IgG) with high affinity. Four out of the five domains in protein A tend to bind with the Fc region of IgG molecule. Protein A was purchased from Thermo Scientific.

10.2.2.3 Immunoglobulin G (IgG)

An antibody is a Y-shaped protein as shown in Figure 10-6 that binds highly specifically with its corresponding antigen. In this work, rabbit IgG was purchased from Sigma-Aldrich.

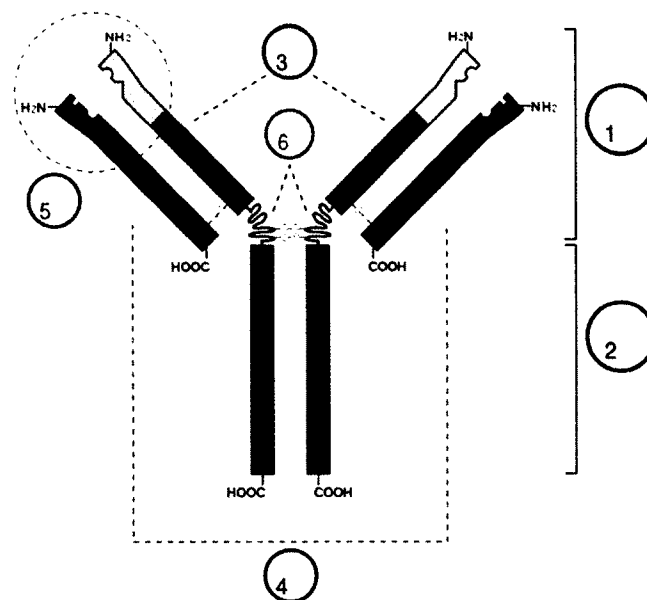


Figure 10-6: Structure of IgG where 1) Fab region, 2) Fc region, 3) heavy chain, 4) light chain, 5) antigen binding sites, 6) hinge regions [140].

10.2.2.4 Sea Block

Sea Block blocking buffer was used to prevent non-specific binding of the IgG on the sensor surface. Sea Block buffer was purchased from Thermo Scientific.

10.3 Equipment

10.3.1 Equipment Needed for Fabrication

10.3.1.1 Hot Plate

The hot plate was used to dry the wafer after the initial cleaning step. The soft-bake required for the photoresist and LOR 3B are also done on a hot plate.

10.3.1.2 Spin Coater

The spin coater (manufactured by Cost Effective Equipment) was used to coat uniform thickness of photoresist and LOR 3B on the wafer.

10.3.1.3 UV Light Source and Mask Aligner

SUSS MicroTec mask aligner was used to align the mask and the wafer; the wafer was then exposed with a UV light source.

10.3.1.4 E-beam Evaporator

The E-beam evaporator from CHA industry was used to deposit chromium (Cr) and gold (Au) for the contacts.

10.3.1.5 Optical Microscope

An optical microscope was used during various stages of fabrication to inspect the patterns on the wafer. The microscope used is Olympus Vannox AHMT3.

10.3.1.6 Vacuum Pump

Vacuum pump in conjunction with membrane filter was used to carry out vacuum filtration of acid treated SWCNTs.

10.3.1.7 Ultra-sonic Agitator

The ultra-sonic agitator (Branson 2510) was used to agitate the final SWCNTs solution. The agitation helps to get a well-dispersed SWCNTs solution.

10.3.2 Equipment Needed for Characterization and Protein Detection

The device characterization and protein detection was carried out on a Keithley probe station. We used a zeta-potential measuring device to investigate the charge on the functionalized SWCNTs; it was also used to investigate the charge on the protein A and IgG at different pH values.

10.3.3 Other Equipment

A micropipette is useful in dispensing the desired amount of PBS, protein A, and IgG during various stages of the project. A handheld pH meter is also useful in investigating the pH value of the SWCNTs solution.

CHAPTER 11

FET BASED BIOSENSOR: FABRICATION

The FET based biosensor was fabricated with a combination of conventional top-down photolithography methods and LBL self-assembly.

11.1 Fabricating the Source and Drain Contact Electrodes

Since both the type I and type II devices require the source and drain contact electrodes, it was logical to begin fabricating these contacts first. All the devices were fabricated on a single 100 mm, p-type <100> silicon substrate. The silicon wafer has a 200 nm thick layer of thermally grown oxide. This oxide ensures that the devices fabricated on the wafer are not electrically shunted at any point during the characterization or testing phase.

Fabrication of the source and drain contact electrodes began with cleaning the silicon wafer. The organic debris on the wafer was cleaned by immersing the wafer in an aqueous mixture of ammonium hydroxide, hydrogen peroxide, and DI water (ratio of 1: 1: 10, respectively) for 20 minutes at a temperature of 75° C. After 20 minutes the wafer was taken out of the cleaning solution and first immersed in a bath of DI water for five minutes, followed by a thorough rinse under running DI water for one minute. The wafer was dried by blowing nitrogen and then placed over the hot plate at 115° C for five minutes to ensure it was completely dry. As shown in Figure 11-1, to create a bilayer of

LOR and S1813 resist, first a 600 nm thick layer of LOR 3B was uniformly coated on the wafer using a spin coater. The wafer was then soft baked at 180° C for three minutes on a hot plate. After a five minute cool down, a one-micron thick layer of resist S1813 was coated on the wafer. It was then soft-baked on the hot plate at 115° C for 90 s, followed by a five minute cool down.

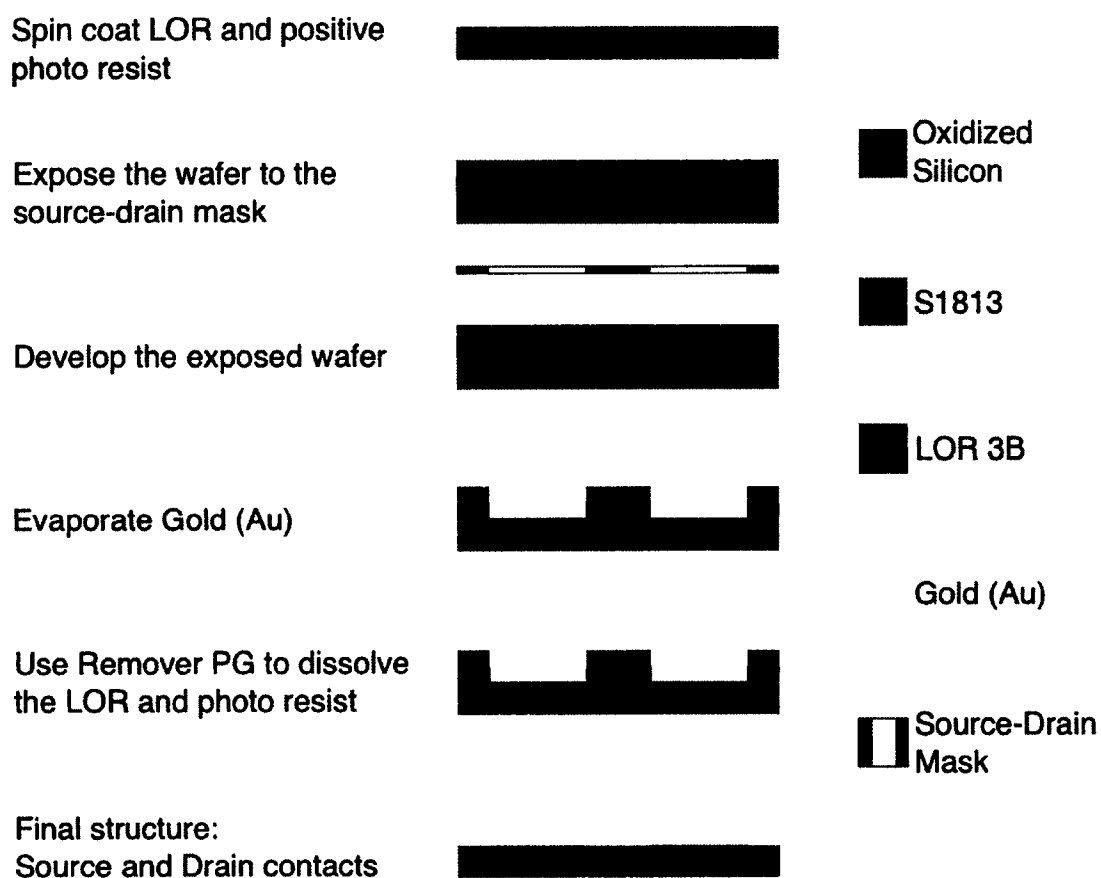


Figure 11-1: Process flow to fabricate source and drain contacts for type I and type II devices.

To transfer the pattern of the source and drain contact electrodes on the wafer, the source-drain mask was loaded into the mask aligner and then the wafer was exposed for 11 s. The exposed wafer was developed in MF-319 developer solution for 60 s and the

quality of the pattern was inspected under an Olympus microscope. The undercut in the LOR 3B layer is very important for the lift-off process, as a good undercut ensures easy metal lift-off. The developed wafer was then loaded into an E-beam evaporator to deposit 100 nm of Au. To enhance the adhesion of Au on silicon oxide, a 50 nm thick layer of Cr was deposited prior to the deposition of Au.

To perform the final metal lift-off step, the wafer was dipped in a bath of the Remover PG solution heated to 60° C for three to four hours. A dip in the second bath greatly helped to remove the unwanted metal layer completely. After inspecting the wafer under the microscope, the final step was to clean the wafer in IPA and then rinse with DI water.

11.2 Fabricating the Gate Electrode

The gate contact electrode for the type I device was fabricated using the metal lift-off technique. To create a bilayer of LOR and S1813 resist, first a 600 nm thick layer of LOR 3B was uniformly coated on the wafer with a spin coater. The wafer was then soft baked at 180° C for three minutes on a hot plate. After a five minute cool down, a one-micrometer thick layer of resist S1813 was coated on the wafer. The wafer was then soft-baked on a hot plate at 115° C for 90 s, followed by a five minute cool down.

To transfer the gate pattern on the wafer, the gate mask was loaded into the mask aligner and then the exposed for 11 s. The exposed wafer was developed in MF-319 developer solution for 60 s and the quality of the pattern was inspected under an Olympus microscope. The developed wafer was then loaded into an E-beam evaporator to deposit 150 nm of Al.

To perform the final metal lift-off step, the wafer was dipped into a bath of the Remover PG solution heated to 60° C for three to four hours. A dip in the second bath greatly helped to remove the unwanted metal layer completely. After inspecting the wafer under the microscope, the final step was to clean the wafer in IPA and then to rinse with DI water.

11.3 Fabricating the Channel

A combination of photolithography and LBL assembly was used to fabricate the channel for type I and type II devices. The entire process flow for type II device is shown in Figure 11-2, and the same process was used to fabricate the channel for the type I device. The fabrication began with transferring the channel pattern on the wafer. A one-micrometer thick layer of positive photoresist (S1813) was spin coated on the wafer and pre-baked on a hot plate at 115° C for 90 s. The wafer was then exposed to the channel mask and developed in the MF 319 solution for 60 s followed by a rinse with DI water. Next the channel was assembled on the patterned wafer using LBL approach.

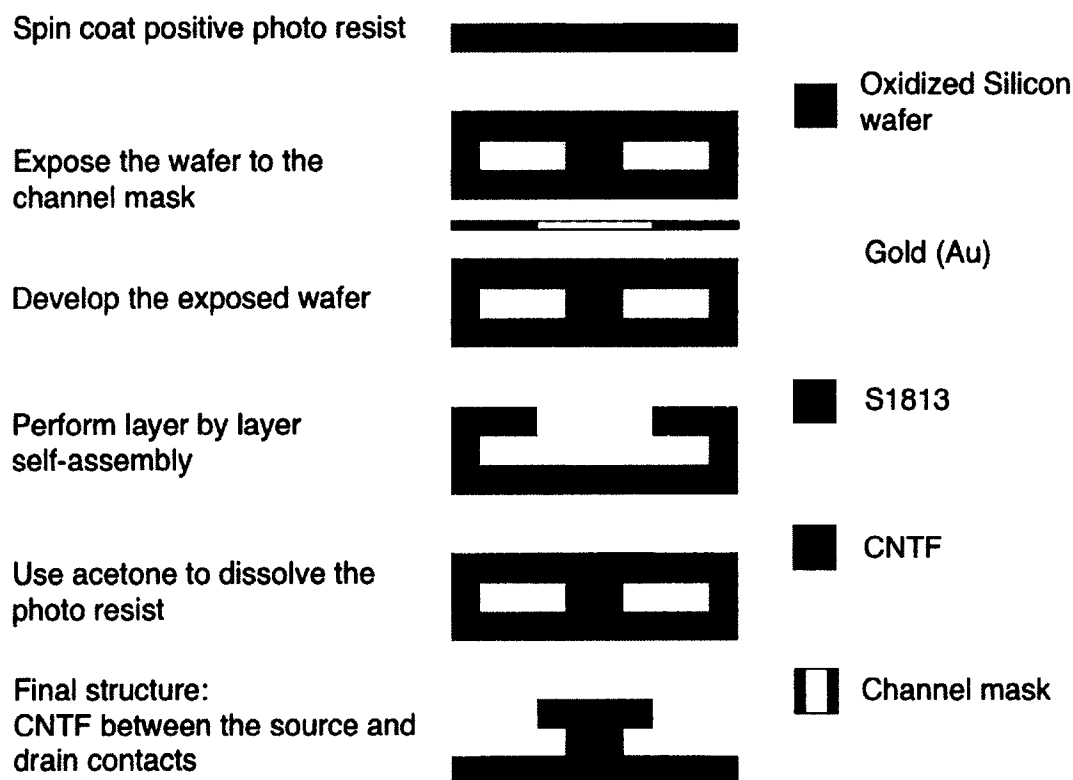


Figure 11-2: Process flow to assemble the channel in between the source and drain for type II device.

For the LBL assembly, polyelectrolyte solutions were prepared by adding 1.4 wt% of PDDA and 0.3 wt% of PSS in DI water. To improve the ionic strength, 0.5 M NaCl was added to the PDDA and PSS solutions. First, a precursor layer was assembled by alternately immersing the wafer in the aqueous solution of PDDA and PSS in a sequence of [PDDA (10 minutes) + PSS (10 minutes)]₂. The subscript indicates the number of cycles; one cycle includes a 10-minute incubation in the PDDA solution, a 30 s rinse in DI water, and 20 s air dry followed by a 10-minute incubation in the PSS solution, a 30 s rinse in DI water, and 20 s air dry.

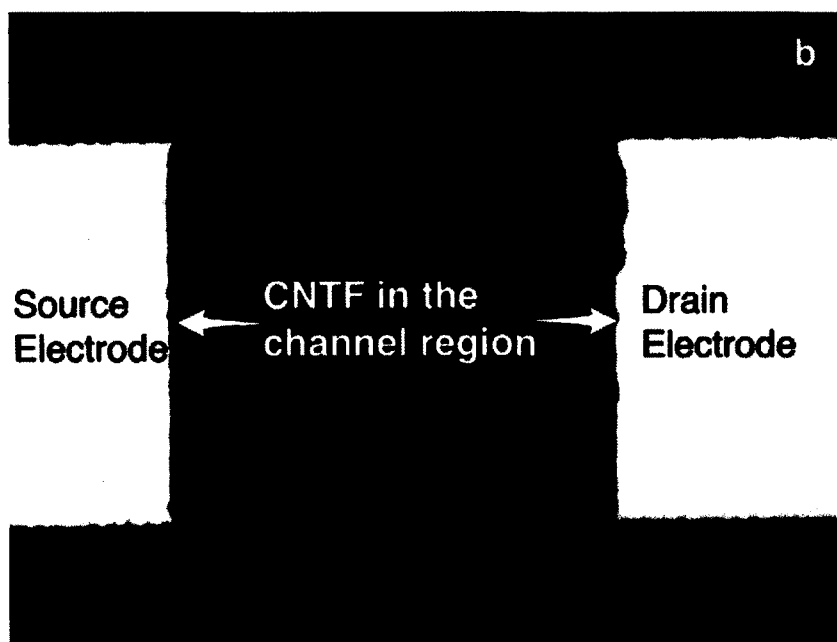
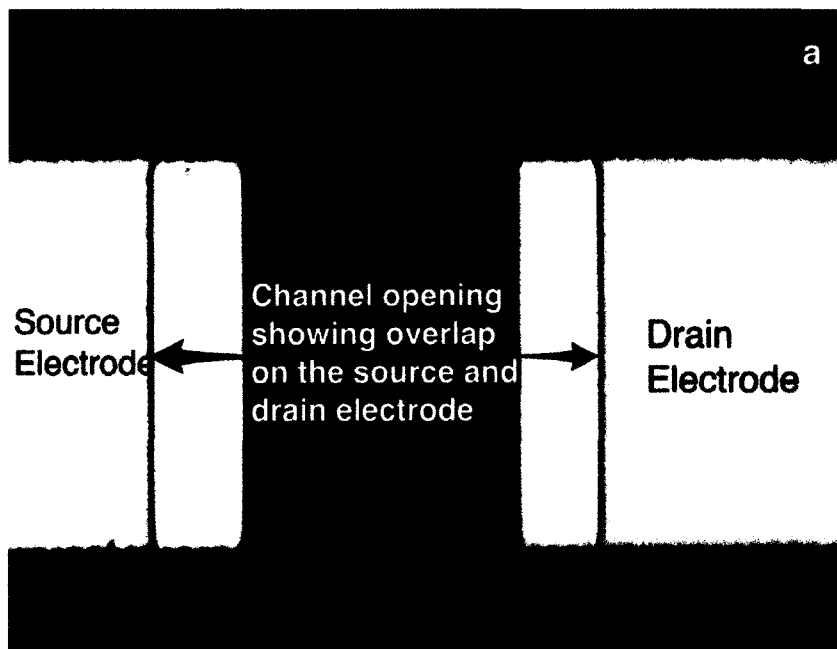
The functional reliability of a SWCNT based FET fabricated by LBL assembly is much higher if the numbers of assembled layers are more than four [186]. Following the

precursor assembly, the wafer was then alternatively immersed in the aqueous solution of PDDA and SWCNTs dispersion in a sequence of [PDDA (10 minutes) + SWCNTs solution (10 minutes)]₁₀. After completing the 10th cycle, the wafer was immersed in an acetone bath to lift-off the unwanted CNTF layer and then rinsed with IPA and DI water. To improve the current density of the channel, the wafer was annealed at 115° C for 20 hours in a vacuum. The annealing helps to remove water molecules trapped in the film and makes quantum mechanical tunneling easier [174].

The thickness of the CNTF was measured using a Quartz Crystal Microbalance (QCM, USI System, Japan). The precursor layers and the subsequent layers of SWCNTs were assembled on the QCM resonator by following the previously mentioned LBL assembly protocol. The relationship between the thickness (d) and frequency shift (ΔF) was given by [187]:

$$d(\text{nm}) = -0.022 \times \Delta F (\text{Hz}). \quad \text{Eq. 11-1}$$

For the 9-MHz resonator with an effective area of $0.16 \pm 0.01 \text{ cm}^2$, the final film thickness was $\sim 95 \text{ nm}$. The optical micrographs of the devices before and after LBL assembly are shown in Figure 11-3. The SEM image of the CNTF with 10 layers is shown in Figure 11-4.



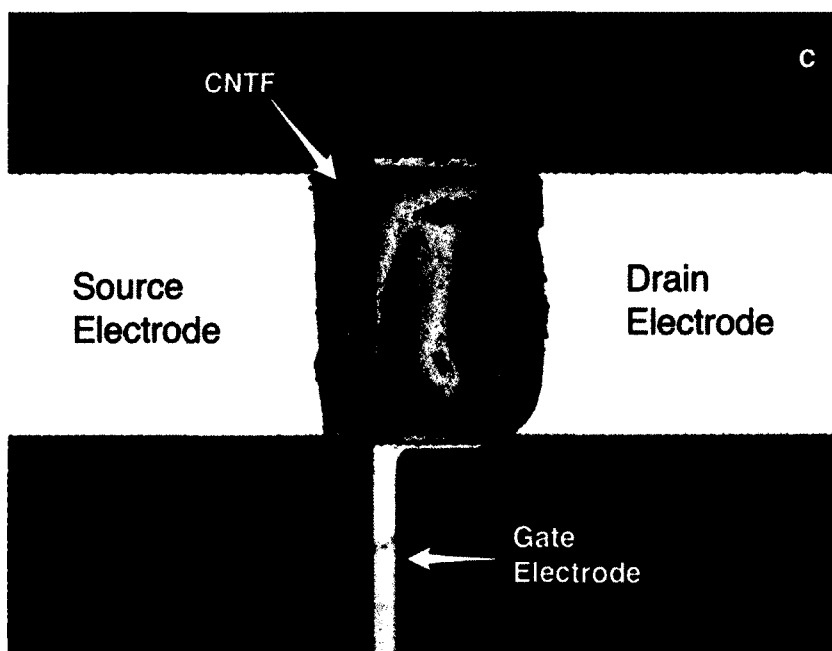


Figure 11-3: a) Optical micrograph of type II device before LBL assembly and b) optical image of type II device after LBL assembly. The channel length is $100\ \mu\text{m}$, the width is $150\ \mu\text{m}$ and the channel overlap on the source and drain electrode is $20\ \mu\text{m}$, and the source and drain electrodes are made of Au. c) Optical image of type I device after LBL assembly, the source and drain electrodes are made of Au while the gate electrode is made of Al.

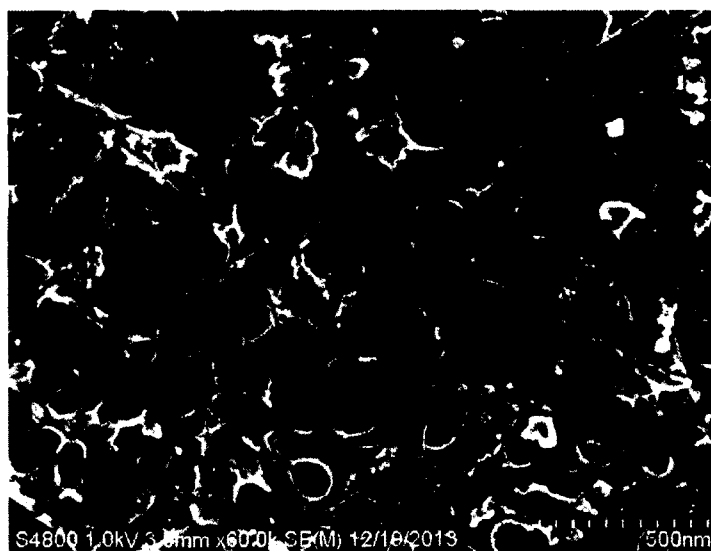
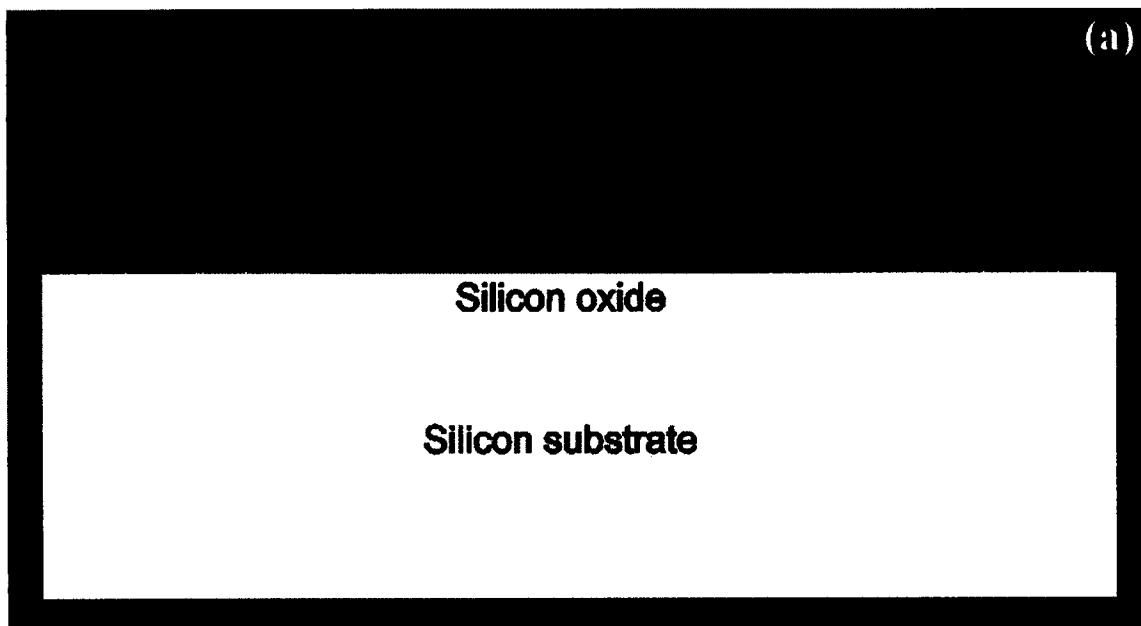


Figure 11-4: SEM image of the CNTF; the CNTF has 10 layers.

11.4 Passivizing the Source and Drain Contacts

As discussed in Section 9.5.2, the sensing in an immunosensor based on individual SWCNT is attributed to Schottky Barrier modulation and Electrostatic gating. To eliminate the influence of contacts during bio sensing, the source and drain contacts were passivized. For the type II device, once the channel was assembled between the source and drain contacts, a one-micrometer thick layer of S1813 was spin coated on the wafer and then baked at 115° C for 90 s. To open a window that exposes only the channel, the same gate mask used for type I device was utilized. After exposing the wafer to the gate mask and developing it in MF 319, the wafer was then hard-baked at 115° C for 60 s. The schematic cross-sectional view of the passivized type II device is shown in Figure 11-5a, the optical graph of the actual passivized type II device is shown in Figure 11-5b.



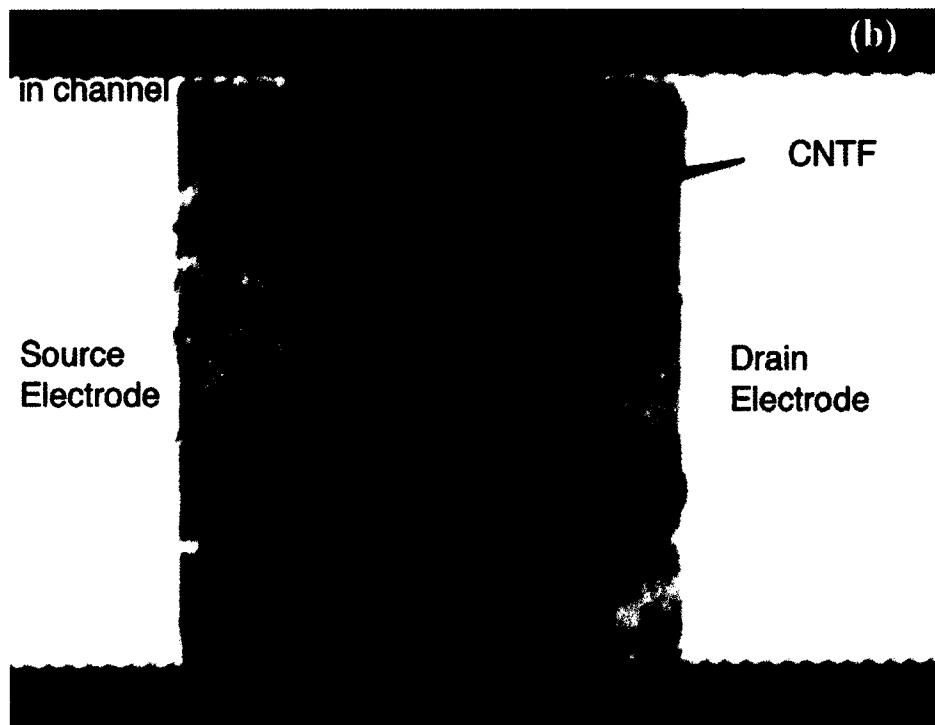


Figure 11-5: a) Schematic cross-sectional view of a passivized type II device b) optical top view image of actual fabricated device (bottom) showing the passivized contacts and a window in the middle exposing the microwire channel only.

Finally, the wafer was diced into individual devices ($\sim 2 \text{ cm} \times 2 \text{ cm}$) as shown in Figure 11-6a, to use them for sensing bio molecules. A PDMS based fluidic channel can be incorporated with the device to facilitate the flow of IgG as shown in Figure 11-6b.

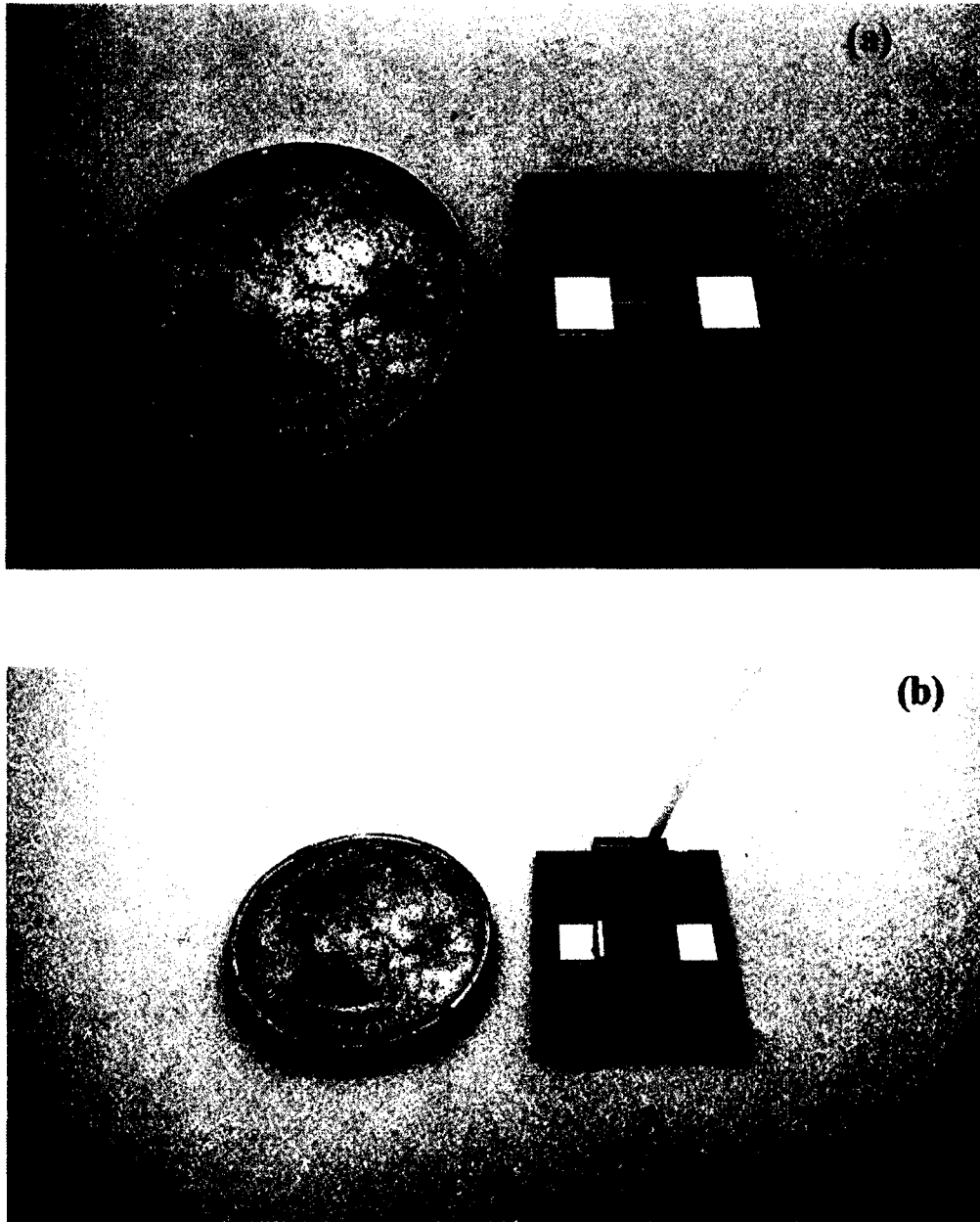


Figure 11-6: a) Picture on the top shows an individual device. The size is ~ 2 cm x ~ 2 cm b) the device with a fluidic channel and tube connection to facilitate IgG flow.

CHAPTER 12

FET BASED BIOSENSOR: EXPERIMENTAL PROTOCOL, RESULTS AND DISCUSSION

12.1 Performance of the Device as an FET

Before the device was used as a biosensor to detect biomolecules, it was logical to test its performance as a transistor. An FET based on individual SWCNT showed a p-type behavior [117] and the same p-type behavior was seen in the FET fabricated by the LBL assembly of SWCNTs [186]. As mentioned earlier, the type I device was specifically fabricated to verify the FET behavior of the device. The transfer characteristic of an FET is a plot of drain current (I_d) variation in response to the change in gate to source voltage (V_{gs}); for a p-type device the drain current decreases with an increase in V_{gs} . The transfer characteristic of the type I device was plotted by sweeping V_{gs} from -6 V to 6 V and recording the corresponding I_d , while maintaining a constant drain to source voltage ($V_{ds} = 4$ V). The output characteristic of the device is shown in Figure 12-1a. As shown in Figure 12-1b, the drain current started to decrease with the increase in the V_{gs} , and hence, showed a p-type behavior. The majority carriers in a CNT are holes. The application of negative gate voltage led to an accumulation of majority carriers in the channel and hence the I_d increased. The p-type behavior was consistently

observed in all the fabricated devices and this reliability can be attributed to the relatively large number of assembled layers.

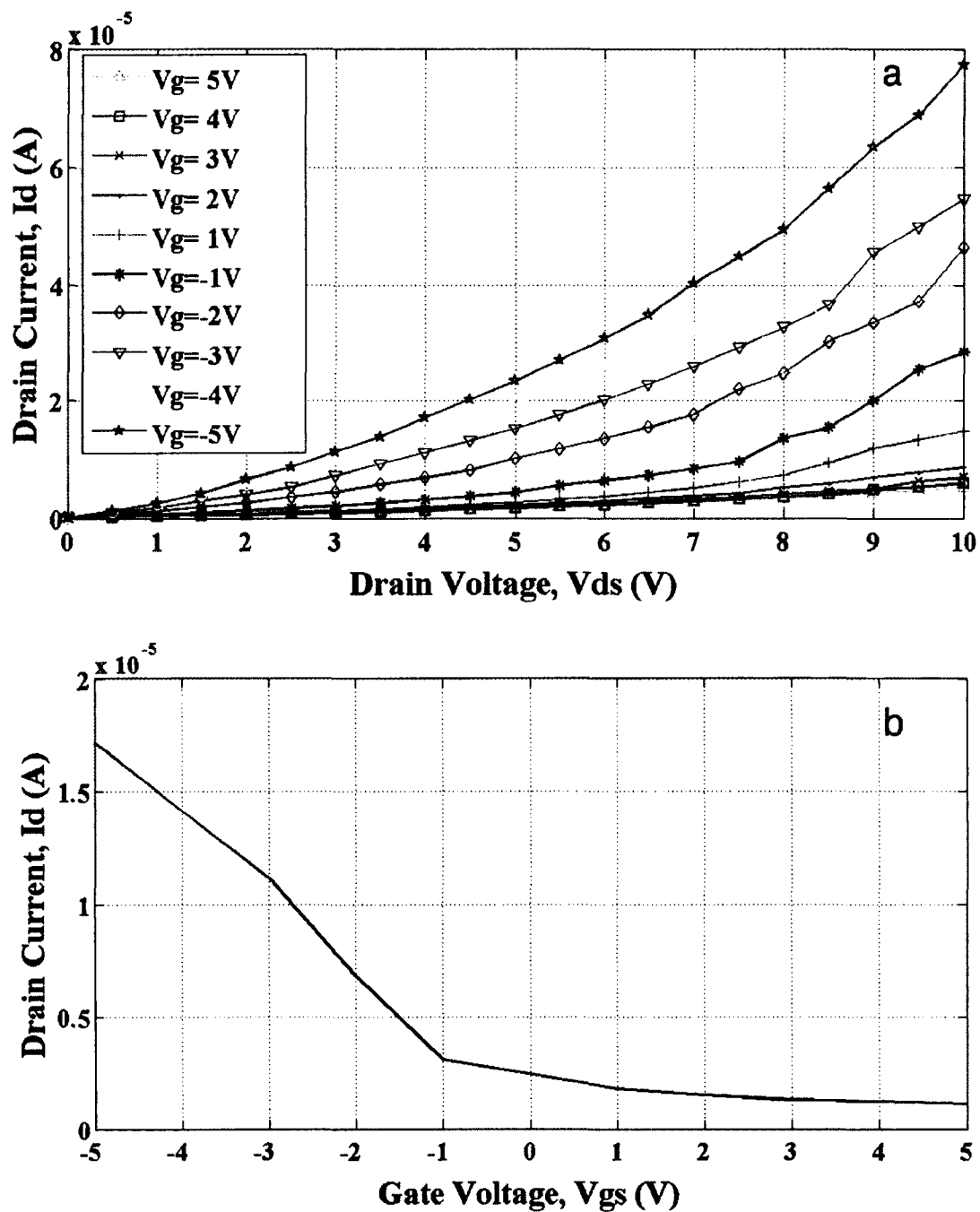


Figure 12-1: a) Output characteristic b) transfer characteristic of type I device for drain to source voltage, $V_{ds} = 4$ V. The device gate length is $100 \mu\text{m}$ and gate width is $100 \mu\text{m}$.

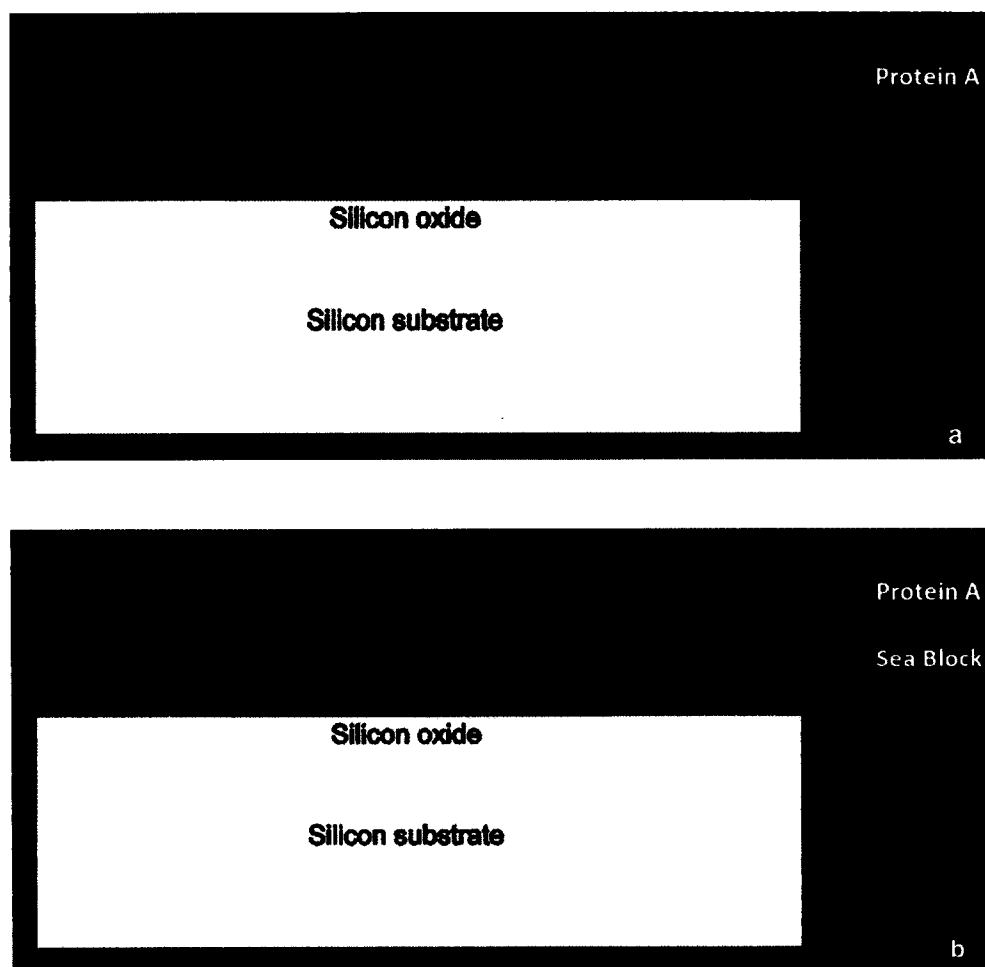
12.2 Experiment Protocol

For biosensing experiments, only type II devices were used. To prepare the device for the experiments, first the Protein A (PA) and IgG were reconstituted in 0.01 M of PBS solution at a pH of 7.4. Next, to immobilize PA on the channel, the device with passivated contacts was treated with the EDC solution for 15 minutes at room temperature and then rinsed with 0.01 M PBS solution. Following the rinse, the device was immediately incubated in 1 mg/mL solution of PA for two hours at room temperature.

The EDC reacts with a carboxyl group on the SWCNT to form an amine-reactive *O*-acylisourea intermediate that spontaneously reacts with primary amines in the PA and facilitates the coupling between them. The device was then rinsed with PBS to wash off excess PA, followed by a one-hour incubation in the sea block solution prepared by adding one part sea block to five parts of 0.01 M PBS. The sea block ensures the unoccupied spaces left after PA incubation is not available for further non-specific IgG bonding on the channel surface. After incubating the device in the sea block for one-hour, the device was rinsed with 0.01 M PBS and blown dry.

All the electrical measurements were performed by applying a $V_{ds} = 10$ mV and recording the drain current in the presence of the 0.01 M PBS solution. First, the reference drain current value (current value without any IgG introduced) was recorded by dropping a 10- μ L volume of 0.01 M PBS directly on the device. After recording the reference current, the device was blown dry and 10- μ L volume of the lowest IgG (IgG1) concentration was dropped on the device and incubated for 15 minutes, followed by a PBS rinse and dry. To record the change in drain current caused by the PA-IgG1

interaction, a 10- μ L volume of 0.01 M PBS was dropped on the device and the drain current was recorded. The 10- μ L drop of PBS present on the device was blown dry and then a 10- μ L volume of the next higher concentration of the IgG (IgG2) was added and incubated for 15 minutes, followed by another PBS rinse and dry. Again, the change in current caused by PA-IgG2 interaction was recorded in the presence of a 10- μ L drop of 0.01 M PBS solution. After the PBS drop was dried, the device was ready for the next higher concentration of IgG. The schematic representation of the experiment protocol is shown in Figure 12-2.



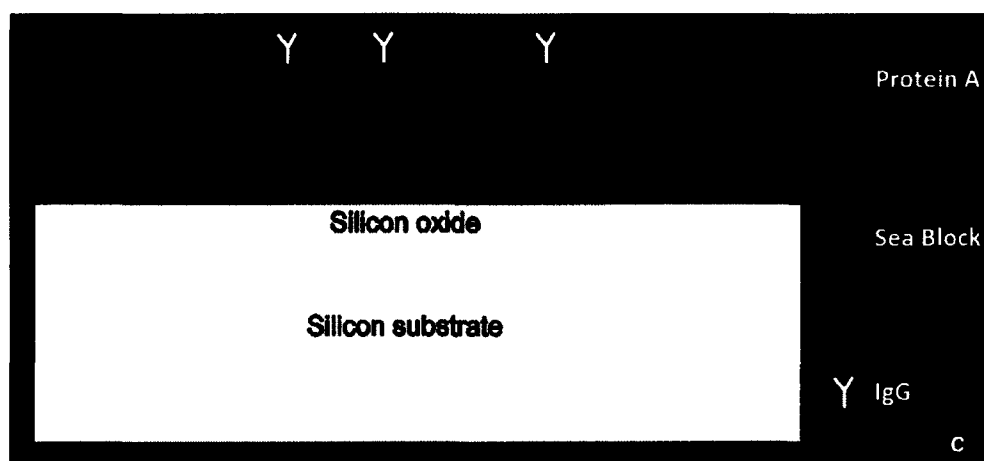


Figure 12-2: Schematic representation of the protocol a) after Protein A immobilization on CNTF surface b) after blocking unoccupied spaces with sea block c) specific bio-affinity interaction between Protein A and IgG.

12.3 Performance of the Device as a Biosensor

After incubating the device with PA and then using the sea block to block all the other unoccupied areas left after PA incubation, the device was connected to the Keithley probe station. As mentioned earlier, a $V_{ds} = 10$ mV was applied in between the drain and the source, and the reference drain current was recorded after dropping 10- μ L of 0.01 M PBS solution directly on to the device. As shown in Figure 12-3, the drain current reaches an almost steady reference value of ~ 0.57 μ A. The device was then exposed to IgG starting with the lowest IgG concentration. A 10- μ L volume of 1 pg/mL IgG concentration was dropped directly on to the device and allowed to incubate for 15 minutes. The device was then rinsed with 0.01 M PBS and dried. The interaction between PA and IgG is highly specific, where the Fc region of the IgG binds specifically with the PA. To record the change in the drain current due to the PA-IgG interaction, a $V_{ds} = 10$ mV was applied to the device and a 10- μ L volume of 0.01 M PBS solution was dropped

directly on to the device. The IgG was reconstituted in 0.01 M PBS at pH 7.4, and at this pH the measured zeta potential of the IgG was around -11 mV. The specific binding between PA-IgG on the surface of the channel in the presence of a 0.01 M PBS droplet was then equivalent to applying a negative voltage to the channel. Based on the transfer characteristics of the type I device as shown in Figure 12-1, the drain current will increase with increasing values of negative gate voltages. For the type II device exposed to the lowest IgG concentration (~ 1 pg/mL), the drain current also increased by ~ 300 nA. Further exposure to higher concentrations of IgG showed a consistent increase in the drain current value.

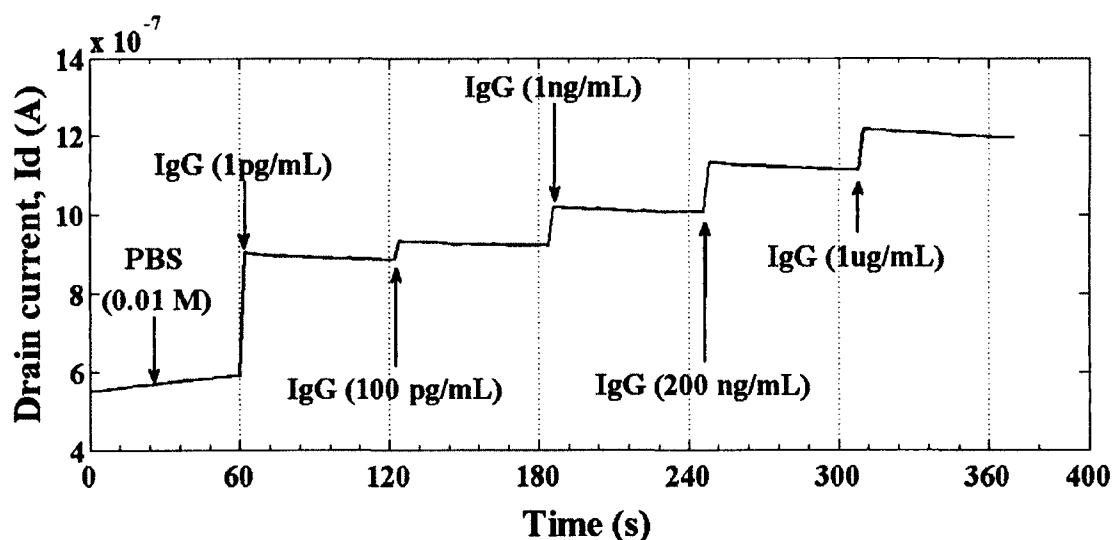


Figure 12-3: Drain current variation in response to various IgG concentrations.

The average value of the drain current for different concentration of IgG is shown in Figure 12-4. The absence of a gate bias for type II device means it operates closer to the threshold voltage ($V_T = 0V$) where the relationship between the drain current and the applied gate voltage is non-linear. The initial reference current (current in presence of PBS only) is for a device without an applied gate voltage. The change in the drain current

after the addition of 1pg/mL of IgG is ~300 nA, (Figure 12-3). This can be attributed to the fact that the addition of IgG shifts the operating point into the non-linear region, which causes a big change in drain current. The change in the drain current after the addition of 100 pg/mL of IgG is ~ 45 nA. The change in the drain current after the addition of 1 ng/mL is ~ 95 nA, and the change in the drain current after the addition of 200 ng/mL is ~115 nA. Further addition of IgG (1 μ g/mL) changes the drain current by only ~ 80 nA. Once all the available Protein A on the substrate interacts with the added IgG, the change in current is expected to drop which is what we observed when IgG (1 μ g/mL) is added.

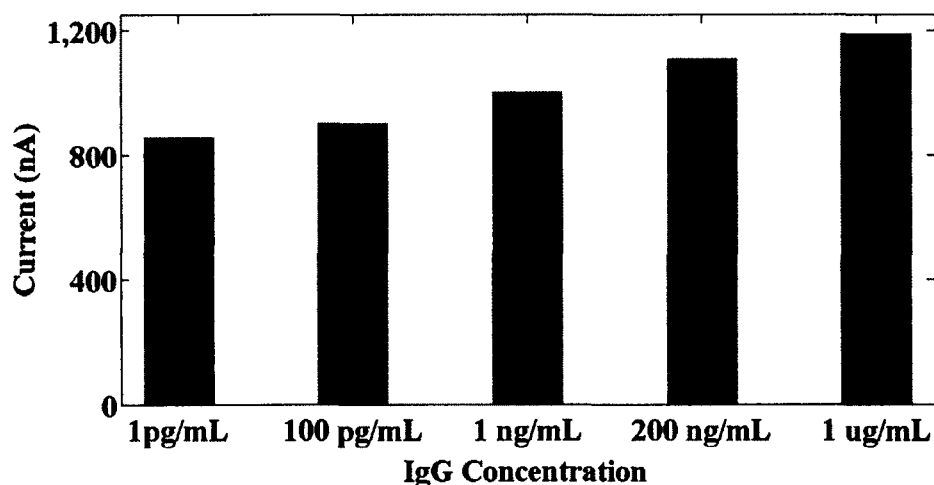


Figure 12-4: Average drain current values for different concentrations of IgG (three devices were used during the experiment).

CHAPTER 13

FET BASED BIOSENSOR: CONCLUSIONS AND FUTURE WORK

13.1 Conclusions

To avoid the complications encountered in the fabrication of biosensors based on a single CNT, the biosensor was fabricated out of carbon nanotube thin film. The FET based biosensor was fabricated using a combination of photolithography and Layer-by-Layer self-assembly. Device characterization confirmed that the fabricated device behaves like a p-type transistor. Experiments done to investigate the response of the device to Protein A-IgG interaction indicated that the device could detect IgG concentrations that are as low as 1 pg/mL.

13.2 Future Work

The response of the device could be improved by avoiding the acid treatment done on the CNTs. This treatment helped to disperse CNTs in water, but it does affect the electrical properties of the tubes. The device offers a platform to design sensors for detecting cancer markers

REFERENCES

- [1] Z. Gong, H. Zhao, T. Zhang, F. Nie, P. Pathak, K. Cui, Z. Wang, S. Wong, and L. Que, “Drug effects analysis on cells using a high throughput microfluidic chip,” *Biomed. Microdevices*, vol. 13, no. 1, pp. 215–219, Feb. 2011.
- [2] F. Denizot and R. Lang, “Rapid colorimetric assay for cell growth and survival,” *J. Immunol. Methods*, vol. 89, no. 2, pp. 271–277, 1986.
- [3] Z. Gong, F. Nie, T. Zhang, P. Pathak, Z. Wang, K. Cui, H. Zhao, S. Wong, and L. Que, “High throughput analysis of drug effects on single breast cancer cells using droplet-microfluidic devices,” in *2010 IEEE 23rd International Conference on Micro Electro Mechanical Systems (MEMS)*, 2010, pp. 1015–1018.
- [4] “Cell Membrane,” 2011. [Online]. Available: http://en.wikipedia.org/wiki/File:Cell_membrane_detailed_diagram_en.svg.
- [5] D. Häussinger, “The role of cellular hydration in the regulation of cell function.,” *Biochem. J.*, vol. 313, pp. 697–710, Feb. 1996.
- [6] S. Z. Hua and T. Pennell, “A microfluidic chip for real-time studies of the volume of single cells.,” *Lab Chip*, vol. 9, no. 2, pp. 251–6, Jan. 2009.
- [7] S. Penmetsa, K. Nagrajan, Z. Gong, D. Mills, and L. Que, “Biological cell controllable patch-clamp microchip,” *Appl. Phys. Lett.*, vol. 97, no. 26, p. 263702, Dec. 2010.
- [8] X. Li, “Microfluidic System for Planar Patch-Clamp Electrode Arrays
Microfluidic System for Planar Patch-Clamp Electrode Arrays,” Yale University, 2006.
- [9] B. Matthews and J. W. Judy, “Design and Fabrication of a Micromachined Planar Patch-Clamp Substrate With Integrated Microfluidics for Single-Cell Measurements,” *J. Microelectromechanical Syst.*, vol. 15, no. 1, pp. 214–222, Feb. 2006.

- [10] J. M. Nagarah, E. Paek, Y. Luo, P. Wang, G. S. Hwang, and J. R. Heath, "Batch fabrication of high-performance planar patch-clamp devices in quartz.," *Adv. Mater.*, vol. 22, no. 41, pp. 4622–7, Nov. 2010.
- [11] C. Ionescu-Zanetti, R. M. Shaw, J. Seo, Y.-N. Jan, L. Y. Jan, and L. P. Lee, "Mammalian electrophysiology on a microfluidic platform.," *Proc. Natl. Acad. Sci. U. S. A.*, vol. 102, no. 26, pp. 9112–7, Jun. 2005.
- [12] P. Pathak, H. Zhao, Z. Gong, F. Nie, T. Zhang, K. Cui, Z. Wang, S. T. C. Wong, and L. Que, "Real-time monitoring of cell viability using direct electrical measurement with a patch-clamp microchip.," *Biomed. Microdevices*, vol. 13, no. 5, pp. 949–53, Oct. 2011.
- [13] "Animal_cell_structure_en." [Online]. Available: http://en.wikipedia.org/wiki/File:Animal_cell_structure_en.svg.
- [14] A. L. Hodgkin and A. F. Huxley, "A quantitative description of membrane current and its application to conduction and excitation in nerve.," *J. Physiol.*, vol. 117, no. 4, pp. 500–544, Feb. 1952.
- [15] S. B. Hladky and D. A. Haydon, "Ion transfer across lipid membranes in the presence of gramicidin A.," *Biochim. Biophys. Acta - Biomembr.*, vol. 274, no. 2, pp. 294–312, 1972.
- [16] "Ion_channel_gating." [Online]. Available: <http://www.zoology.ubc.ca/%7Egardner/F21-08.GIF>.
- [17] B. A. Niemeyer, L. Mery, C. Zawar, A. Suckow, F. Monje, L. A. Pardo, W. Stuhmer, V. Flockerzi, and M. Hoth, "Ion channels in health and disease. 83rd Boehringer Ingelheim Fonds International Titisee Conference.," *EMBO Rep.*, vol. 2, no. 7, pp. 568–73, Jul. 2001.
- [18] R. Felix, "Channelopathies: ion channel defects linked to heritable clinical disorders.," *J. Med. Genet.*, vol. 37, no. 10, pp. 729–40, Oct. 2000.
- [19] M. S. Chorghade, Ed., "Drug Discovery and Development," 14-Apr-2006. [Online]. Available: http://www.innovation.org/drug_discovery/objects/pdf/RD_Brochure.pdf.
- [20] J. Xu, X. Wang, B. Ensign, M. Li, L. Wu, A. Guia, and J. Xu, "Ion-channel assay technologies: quo vadis?," *Drug Discov. Today*, vol. 6, no. 24, pp. 1278–1287, 2001.
- [21] "Patch_clamp." [Online]. Available: http://en.wikipedia.org/wiki/File:Patch_clamp.svg.

- [22] A. Demuro and I. Parker, “‘Optical patch-clamping’: single-channel recording by imaging Ca²⁺ flux through individual muscle acetylcholine receptor channels,” *J. Gen. Physiol.*, vol. 126, no. 3, pp. 179–92, Sep. 2005.
- [23] J. Denyer, J. Worley, B. Cox, G. Allenby, and Martyn Banks, “HTS approaches to voltage-gated ion channel drug discovery,” *Drug Discov. Today*, vol. 3, no. 7, pp. 323–332, 1998.
- [24] E. NEHER and B. SAKMANN, “Single-channel currents recorded from membrane of denervated frog muscle fibres,” *Nature*, vol. 260, no. 5554, pp. 799–802, Apr. 1976.
- [25] E. Neher, B. Sakmann, and J. H. Steinbach, “The extracellular patch clamp: A method for resolving currents through individual open channels in biological membranes,” *Pflugers Arch. Eur. J. Physiol.*, vol. 375, no. 2, pp. 219–228, Jul. 1978.
- [26] O. P. Hamill, A. Marty, E. Neher, B. Sakmann, and F. J. Sigworth, “Improved patch-clamp techniques for high-resolution current recording from cells and cell-free membrane patches,” *Pflugers Arch. Eur. J. Physiol. Arch. Eur. J. Physiol.*, vol. 391, no. 2, pp. 85–100, Aug. 1981.
- [27] F. J. Sigworth and K. G. Klemic, “Microchip Technology in Ion-Channel Research,” *IEEE Trans. Nanobioscience*, vol. 4, no. 1, pp. 121–127, Mar. 2005.
- [28] “Patch_clamp_configuration.” [Online]. Available: <http://www.leica-microsystems.com/science-lab/the-patch-clamp-technique/>.
- [29] M. Fejtl, U. Czubayko, A. Hümmer, T. Krauter, and A. Lepple-Wienhues, “Flip-the-tip: automated patch clamping based on glass electrodes,” *Methods Mol. Biol.*, vol. 403, pp. 71–85, Jan. 2007.
- [30] N. Fertig, A. Tilke, R. H. Blick, J. P. Kotthaus, J. C. Behrends, and G. ten Bruggencate, “Stable integration of isolated cell membrane patches in a nanomachined aperture,” *Appl. Phys. Lett.*, vol. 77, no. 8, p. 1218, Aug. 2000.
- [31] P. Chen, W. Zhang, J. Zhou, P. Wang, L. Xiao, and M. Yang, “Development of planar patch clamp technology and its application in the analysis of cellular electrophysiology,” *Prog. Nat. Sci.*, vol. 19, no. 2, pp. 153–160, 2009.
- [32] N. Fertig, M. Klau, M. George, R. H. Blick, and J. C. Behrends, “Activity of single ion channel proteins detected with a planar microstructure,” *Appl. Phys. Lett.*, vol. 81, no. 25, p. 4865, Dec. 2002.

- [33] N. Fertig, C. Meyer, R. Blick, C. Trautmann, and J. Behrends, "Microstructured glass chip for ion-channel electrophysiology," *Phys. Rev. E*, vol. 64, no. 4, p. 040901, Sep. 2001.
- [34] Y. Xia and G. M. Whitesides, "Soft Lithography," *Angew. Chemie Int. Ed.*, vol. 37, no. 5, pp. 550–575, Mar. 1998.
- [35] K. G. Klemic, J. F. Klemic, and F. J. Sigworth, "An air-molding technique for fabricating PDMS planar patch-clamp electrodes.," *Pflugers Arch.*, vol. 449, no. 6, pp. 564–72, Mar. 2005.
- [36] J. Seo, C. Ionescu-Zanetti, J. Diamond, R. Lal, and L. P. Lee, "Integrated multiple patch-clamp array chip via lateral cell trapping junctions," *Appl. Phys. Lett.*, vol. 84, no. 11, p. 1973, Mar. 2004.
- [37] "Measuring Cell Viability / Cytotoxicity." [Online]. Available: https://www.dojindo.com/Protocol/Cell_Proliferation_Protocol_Colorimetric.pdf.
- [38] F. Denizot and R. Lang, "Rapid colorimetric assay for cell growth and survival. Modifications to the tetrazolium dye procedure giving improved sensitivity and reliability.," *J. Immunol. Methods*, vol. 89, no. 2, pp. 271–7, May 1986.
- [39] "Measuring Cell Viability / Cytotoxicity: Cell Counting Kit-F." [Online]. Available: https://www.dojindo.com/Protocol/Cell_Proliferation_Protocol_Fluorometric.pdf.
- [40] S. Penmetsa, K. Nagrajan, Z. Gong, D. Mills, and L. Que, "A PATCH-CLAMP DEVICE WITH CELL SORTING AND POSITIONING FUNCTIONS Institute for Micromanufacturing , Louisiana Tech University , Ruston , Louisiana , USA School of Biological Science , Louisiana Tech University , Ruston , Louisiana , USA ABSTRACT," pp. 81–84, 2009.
- [41] D. Palmieri, Q. R. Smith, P. R. Lockman, J. Bronder, B. Gril, A. F. Chambers, R. J. Weil, and P. S. Steeg, "Brain metastases of breast cancer.," *Breast Dis.*, vol. 26, pp. 139–47.
- [42] "SU-8 2000 Permanent Epoxy Negative Photoresist PROCESSING GUIDELINES FOR," 2000. [Online]. Available: <http://www.microchem.com/pdf/SU-82000DataSheet2025thru2075Ver4.pdf>.
- [43] "LOR and PMGI Resists." [Online]. Available: <http://www.microchem.com/pdf/RevPMGI-Resists-data-sheetV-rhcredit-100311.pdf>.

- [44] W. Zheng, R. H. Spencer, and L. Kiss, "High throughput assay technologies for ion channel drug discovery.," *Assay Drug Dev. Technol.*, vol. 2, no. 5, pp. 543–52, Oct. 2004.
- [45] L. Kang, B. G. Chung, R. Langer, and A. Khademhosseini, "Microfluidics for drug discovery and development: From target selection to product lifecycle management," *Drug Discov. Today*, vol. 13, no. 1, pp. 1–13, 2008.
- [46] K. Balasubramanian, "Challenges in the use of 1D nanostructures for on-chip biosensing and diagnostics: a review.," *Biosens. Bioelectron.*, vol. 26, no. 4, pp. 1195–204, Dec. 2010.
- [47] J. J. Gooding, R. Wibowo, J. Liu, W. Yang, D. Losic, S. Orbons, F. J. Mearns, J. G. Shapter, and D. B. Hibbert, "Protein electrochemistry using aligned carbon nanotube arrays.," *J. Am. Chem. Soc.*, vol. 125, no. 30, pp. 9006–7, Jul. 2003.
- [48] O. Lazcka, F. J. Del Campo, and F. X. Muñoz, "Pathogen detection: A perspective of traditional methods and biosensors," *Biosens. Bioelectron.*, vol. 22, no. 7, pp. 1205–1217, 2007.
- [49] V. Gubala, L. F. Harris, A. J. Ricco, M. X. Tan, and D. E. Williams, "Point of care diagnostics: status and future.," *Anal. Chem.*, vol. 84, no. 2, pp. 487–515, Jan. 2012.
- [50] R. S. YALOW and S. A. BERSON, "Immunoassay of endogenous plasma insulin in man.," *J. Clin. Invest.*, vol. 39, pp. 1157–75, Jul. 1960.
- [51] E. Engvall and P. Perlmann, "Enzyme-linked immunosorbent assay (ELISA). Quantitative assay of immunoglobulin G.," *Immunochemistry*, vol. 8, no. 9, pp. 871–4, Sep. 1971.
- [52] A. L. Ghindilis, P. Atanasov, M. Wilkins, and E. Wilkins, "Immunosensors: electrochemical sensing and other engineering approaches," *Biosens. Bioelectron.*, vol. 13, no. 1, pp. 113–131, 1998.
- [53] R. J. Meagher, A. V Hatch, R. F. Renzi, and A. K. Singh, "An integrated microfluidic platform for sensitive and rapid detection of biological toxins.," *Lab Chip*, vol. 8, no. 12, pp. 2046–53, Dec. 2008.
- [54] W. R. Heineman and W. B. Jensen, "Leland C. Clark Jr. (1918–2005)," 2006.
- [55] C. L. Morgan, D. J. Newman, and C. P. Price, "Immunosensors: technology and opportunities in laboratory medicine.," *Clin. Chem.*, vol. 42, no. 2, pp. 193–209, Feb. 1996.

- [56] S. Ko and S. A. Grant, "Development of a novel FRET method for detection of *Listeria* or *Salmonella*," *Sensors Actuators B Chem.*, vol. 96, no. 1, pp. 372–378, 2003.
- [57] N. Hildebrandt, L. J. Charbonnière, M. Beck, R. F. Ziessel, and H.-G. Löhmannsröben, "Quantum dots as efficient energy acceptors in a time-resolved fluoroimmunoassay," *Angew. Chem. Int. Ed. Engl.*, vol. 44, no. 46, pp. 7612–5, Nov. 2005.
- [58] T. Zhang, P. Pathak, S. Karandikar, R. Giorno, and L. Que, "A polymer nanostructured Fabry-Perot interferometer based biosensor," *Biosens. Bioelectron.*, vol. 30, no. 1, pp. 128–32, Dec. 2011.
- [59] E. Yablonovitch, "Inhibited Spontaneous Emission in Solid-State Physics and Electronics," *Phys. Rev. Lett.*, vol. 58, no. 20, p. 2059, May 1987.
- [60] S. John, "Strong localization of photons in certain disordered dielectric superlattices," *Phys. Rev. Lett.*, vol. 58, no. 23, p. 2486, Jun. 1987.
- [61] E. Yablonovitch, "Photonic Crystals: What's in a Name?," *Optics and Photonics News*, vol. 18, no. 3, pp. 12–13, Mar-2007.
- [62] E. Choi, Y. Choi, Y. H. P. Nejad, K. Shin, and J. Park, "Label-free specific detection of immunoglobulin G antibody using nanoporous hydrogel photonic crystals," *Sensors Actuators B Chem.*, vol. 180, pp. 107–113, 2013.
- [63] A. A. Suleiman and G. G. Guilbault, "Piezoelectric (PZ) Immunosensors and Their Applications," *Anal. Lett.*, vol. 24, no. 8, pp. 1283–1292, Aug. 1991.
- [64] L. Wang, C. Wu, Z. Hu, Y. Zhang, R. Li, and P. Wang, "Sensing *Escherichia coli* O157:H7 via frequency shift through a self-assembled monolayer based QCM immunosensor," *J. Zhejiang Univ. Sci. B*, vol. 9, no. 2, pp. 121–31, Feb. 2008.
- [65] E. . Olsen, S. . Pathirana, A. . Samoylov, J. . Barbaree, B. . Chin, W. . Neely, and V. Vodyanoy, "Specific and selective biosensor for *Salmonella* and its detection in the environment," *J. Microbiol. Methods*, vol. 53, no. 2, pp. 273–285, 2003.
- [66] C. M. A. Brett, E. J. Cains, F. Ricci, G. Adornetto, and G. Palleschi, "A review of experimental aspects of electrochemical immunosensors," *Electrochim. Acta*, vol. 84, pp. 74–83, 2012.
- [67] J. Katrlík, R. Brandšteter, J. Švorc, M. Rosenberg, and S. Miertuš, "Mediator type of glucose microbial biosensor based on *Aspergillus niger*," *Anal. Chim. Acta*, vol. 356, no. 2, pp. 217–224, 1997.

- [68] W. Oungpipat, P. W. Alexander, and P. Southwell-Keely, "A reagentless amperometric biosensor for hydrogen peroxide determination based on asparagus tissue and ferrocene mediation," *Anal. Chim. Acta*, vol. 309, no. 1, pp. 35–45, 1995.
- [69] P. Bergveld, "Development of an Ion-Sensitive Solid-State Device for Neurophysiological Measurements," *IEEE Trans. Biomed. Eng.*, vol. BME-17, no. 1, pp. 70–71, Jan. 1970.
- [70] L. Yang and R. Bashir, "Electrical/electrochemical impedance for rapid detection of foodborne pathogenic bacteria," *Biotechnol. Adv.*, vol. 26, no. 2, pp. 135–150, Mar. 2008.
- [71] S. M. Radke and E. C. Alocilja, "A high density microelectrode array biosensor for detection of E. coli O157:H7," *Biosensors and Bioelectronics*, vol. 20, no. 8, pp. 1662–1667, 2005.
- [72] L. Esaki, "The evolution of nanoscale quantum effects in semiconductor physics," *Nanostructured Mater.*, vol. 12, no. 1, pp. 1–8, 1999.
- [73] P. Alivisatos, "The use of nanocrystals in biological detection.," *Nat. Biotechnol.*, vol. 22, no. 1, pp. 47–52, Jan. 2004.
- [74] A. K. Wanekaya, W. Chen, N. V. Myung, and A. Mulchandani, "Nanowire-Based Electrochemical Biosensors," *Electroanalysis*, vol. 18, no. 6, pp. 533–550, Mar. 2006.
- [75] J. Kim, M. Junkin, D.-H. Kim, S. Kwon, Y. S. Shin, P. K. Wong, and B. K. Gale, "Applications, techniques, and microfluidic interfacing for nanoscale biosensing," *Microfluid. Nanofluidics*, vol. 7, no. 2, pp. 149–167, Apr. 2009.
- [76] D. J. Maxwell, J. R. Taylor, and S. Nie, "Self-Assembled Nanoparticle Probes for Recognition and Detection of Biomolecules," *J. Am. Chem. Soc.*, vol. 124, no. 32, pp. 9606–9612, Aug. 2002.
- [77] H. Cai, C. Xu, P. He, and Y. Fang, "Colloid Au-enhanced DNA immobilization for the electrochemical detection of sequence-specific DNA," *J. Electroanal. Chem.*, vol. 510, no. 1, pp. 78–85, 2001.
- [78] I. Safarík and M. Safaríková, "Use of magnetic techniques for the isolation of cells.," *J. Chromatogr. B. Biomed. Sci. Appl.*, vol. 722, no. 1–2, pp. 33–53, Feb. 1999.
- [79] J. Richardson, P. Hawkins, and R. Luxton, "The use of coated paramagnetic particles as a physical label in a magneto-immunoassay.," *Biosens. Bioelectron.*, vol. 16, no. 9–12, pp. 989–93, Dec. 2001.

- [80] G. Zheng, F. Patolsky, Y. Cui, W. U. Wang, and C. M. Lieber, "Multiplexed electrical detection of cancer markers with nanowire sensor arrays.," *Nat. Biotechnol.*, vol. 23, no. 10, pp. 1294–301, Oct. 2005.
- [81] X. Duan, Y. Huang, Y. Cui, J. Wang, and C. M. Lieber, "Indium phosphide nanowires as building blocks for nanoscale electronic and optoelectronic devices.," *Nature*, vol. 409, no. 6816, pp. 66–9, Jan. 2001.
- [82] L. Zaraska, G. D. Sulka, and M. Jaskuła, "Porous anodic alumina membranes formed by anodization of AA1050 alloy as templates for fabrication of metallic nanowire arrays," *Surf. Coatings Technol.*, vol. 205, no. 7, pp. 2432–2437, 2010.
- [83] S. Samanman, C. Thammakhet, P. Kanatharana, C. Buranachai, and P. Thavarungkul, "Novel template-assisted fabrication of porous gold nanowire arrays using a conductive-layer-free anodic alumina oxide membrane," *Electrochim. Acta*, vol. 102, pp. 342–350, 2013.
- [84] S. Roy and Z. Gao, "Nanostructure-based electrical biosensors," *Nano Today*, vol. 4, no. 4, pp. 318–334, 2009.
- [85] G. Shen, P.-C. Chen, K. Ryu, and C. Zhou, "Devices and chemical sensing applications of metal oxide nanowires," *J. Mater. Chem.*, vol. 19, no. 7, p. 828, Feb. 2009.
- [86] J. R. Heath, "Superlattice nanowire pattern transfer (SNAP).," *Acc. Chem. Res.*, vol. 41, no. 12, pp. 1609–17, Dec. 2008.
- [87] A. Choi, K. Kim, H.-I. Jung, and S. Y. Lee, "ZnO nanowire biosensors for detection of biomolecular interactions in enhancement mode," *Sensors Actuators B Chem.*, vol. 148, no. 2, pp. 577–582, Jul. 2010.
- [88] J. Hahm and C. M. Lieber, "Direct Ultrasensitive Electrical Detection of DNA and DNA Sequence Variations Using Nanowire Nanosensors," *Nano Lett.*, vol. 4, no. 1, pp. 51–54, Jan. 2004.
- [89] Z. Gao, A. Agarwal, A. D. Trigg, N. Singh, C. Fang, C.-H. Tung, Y. Fan, K. D. Buddharaju, and J. Kong, "Silicon nanowire arrays for label-free detection of DNA.," *Anal. Chem.*, vol. 79, no. 9, pp. 3291–7, May 2007.
- [90] W. U. Wang, C. Chen, K. Lin, Y. Fang, and C. M. Lieber, "Label-free detection of small-molecule-protein interactions by using nanowire nanosensors.," *Proc. Natl. Acad. Sci. U. S. A.*, vol. 102, no. 9, pp. 3208–12, Mar. 2005.

- [91] E. Stern, J. F. Klemic, D. A. Routenberg, P. N. Wyrembak, D. B. Turner-Evans, A. D. Hamilton, D. A. LaVan, T. M. Fahmy, and M. A. Reed, "Label-free immunodetection with CMOS-compatible semiconducting nanowires.," *Nature*, vol. 445, no. 7127, pp. 519–22, Feb. 2007.
- [92] A. Qureshi, W. P. Kang, J. L. Davidson, and Y. Gurbuz, "Review on carbon-derived, solid-state, micro and nano sensors for electrochemical sensing applications," *Diam. Relat. Mater.*, vol. 18, no. 12, pp. 1401–1420, 2009.
- [93] C. W. Marquardt, S. Blatt, F. Hennrich, H. v. Loehneysen, and R. Krupke, "Probing dielectrophoretic force fields with metallic carbon nanotubes," *Appl. Phys. Lett.*, vol. 89, no. 18, p. 183117, Nov. 2006.
- [94] J. Kong, H. T. Soh, A. M. Cassell, C. F. Quate, and H. Dai, "Synthesis of individual single-walled carbon nanotubes on patterned silicon wafers," *Nature*, vol. 395, no. 6705, pp. 878–881, Oct. 1998.
- [95] A. Star, E. Tu, J. Niemann, J.-C. P. Gabriel, C. S. Joiner, and C. Valcke, "Label-free detection of DNA hybridization using carbon nanotube network field-effect transistors.," *Proc. Natl. Acad. Sci. U. S. A.*, vol. 103, no. 4, pp. 921–6, Jan. 2006.
- [96] K. F. Chong, K. P. Loh, S. R. K. Vedula, C. T. Lim, H. Sternschulte, D. Steinmüller, F.-S. Sheu, and Y. L. Zhong, "Cell adhesion properties on photochemically functionalized diamond.," *Langmuir*, vol. 23, no. 10, pp. 5615–21, May 2007.
- [97] L. Tang, C. Tsai, W. W. Gerberich, L. Kruckeberg, and D. R. Kania, "Biocompatibility of chemical-vapour-deposited diamond," *Biomaterials*, vol. 16, no. 6, pp. 483–488, 1995.
- [98] C. E. Nebel, B. Rezek, D. Shin, H. Uetsuka, and N. Yang, "Diamond for biosensor applications," *J. Phys. D: Appl. Phys.*, vol. 40, no. 20, pp. 6443–6466, Oct. 2007.
- [99] W. Yang, O. Auciello, J. E. Butler, W. Cai, J. A. Carlisle, J. E. Gerbi, D. M. Gruen, T. Knickerbocker, T. L. Lasseter, J. N. Russell, L. M. Smith, and R. J. Hamers, "DNA-modified nanocrystalline diamond thin-films as stable, biologically active substrates.," *Nat. Mater.*, vol. 1, no. 4, pp. 253–7, Dec. 2002.
- [100] H. W. Kroto, J. R. Heath, S. C. O'Brien, R. F. Curl, and R. E. Smalley, "C₆₀: Buckminsterfullerene," *Nature*, vol. 318, no. 6042, pp. 162–163, Nov. 1985.
- [101] S. Iijima, "Helical microtubules of graphitic carbon," *Nature*, vol. 354, no. 6348, pp. 56–58, Nov. 1991.

- [102] “Buckyball,” 2001. [Online]. Available: <http://www.godunov.com/Bucky/fullerene.html>.
- [103] R. Saito, M. Fujita, G. Dresselhaus, and M. S. Dresselhaus, “Electronic structure of chiral graphene tubules,” *Appl. Phys. Lett.*, vol. 60, no. 18, p. 2204, May 1992.
- [104] R. Saito, M. Fujita, G. Dresselhaus, and M. Dresselhaus, “Electronic structure of graphene tubules based on C60,” *Phys. Rev. B*, vol. 46, no. 3, pp. 1804–1811, Jul. 1992.
- [105] T. W. Odom, J.-L. Huang, P. Kim, and C. M. Lieber, “Atomic structure and electronic properties of single-walled carbon nanotubes,” *Nature*, vol. 391, no. 6662, pp. 62–64, Jan. 1998.
- [106] C. L. Kane and E. J. Mele, “Size, Shape, and Low Energy Electronic Structure of Carbon Nanotubes,” *Phys. Rev. Lett.*, vol. 78, no. 10, pp. 1932–1935, Mar. 1997.
- [107] J. Kong, E. Yenilmez, T. Tomblor, W. Kim, H. Dai, R. Laughlin, L. Liu, C. Jayanthi, and S. Wu, “Quantum Interference and Ballistic Transmission in Nanotube Electron Waveguides,” *Phys. Rev. Lett.*, vol. 87, no. 10, p. 106801, Aug. 2001.
- [108] W. Liang, M. Bockrath, D. Bozovic, J. H. Hafner, M. Tinkham, and H. Park, “Fabry - Perot interference in a nanotube electron waveguide,” *Nature*, vol. 411, no. 6838, pp. 665–9, Jun. 2001.
- [109] J. R. North, “Immunosensors: Antibody-based biosensors,” *Trends Biotechnol.*, vol. 3, no. 7, pp. 180–186, 1985.
- [110] C. B. Jacobs, M. J. Peairs, and B. J. Venton, “Review: Carbon nanotube based electrochemical sensors for biomolecules,” *Anal. Chim. Acta*, vol. 662, no. 2, pp. 105–127, 2010.
- [111] K. D. Wise, J. B. Angell, and A. Starr, “An Integrated-Circuit Approach to Extracellular Microelectrodes,” *IEEE Trans. Biomed. Eng.*, vol. BME-17, no. 3, pp. 238–247, Jul. 1970.
- [112] P. Bergveld, “Development of an Ion-Sensitive Solid-State Device for Neurophysiological Measurements,” *IEEE Trans. Biomed. Eng.*, vol. BME-17, no. 1, pp. 70–71, Jan. 1970.
- [113] P. Bergveld, “Thirty years of ISFETOLOGY: What happened in the past 30 years and what may happen in the next 30 years,” *Sensors Actuators B Chem.*, vol. 88, no. 1, pp. 1–20, Jan. 2003.

- [114] S. J. Tans, M. H. Devoret, H. Dai, A. Thess, R. E. Smalley, L. J. Geerligs, and C. Dekker, "Individual single-wall carbon nanotubes as quantum wires," *Nature*, vol. 386, no. 6624, pp. 474–477, Apr. 1997.
- [115] S. J. Tans, A. R. M. Verschueren, and C. Dekker, "Room-temperature transistor based on a single carbon nanotube," *Nature*, vol. 393, no. 6680, pp. 49–52, May 1998.
- [116] A. Thess, R. Lee, P. Nikolaev, H. Dai, P. Petit, J. Robert, C. Xu, Y. H. Lee, S. G. Kim, A. G. Rinzler, D. T. Colbert, G. E. Scuseria, D. Tomanek, J. E. Fischer, and R. E. Smalley, "Crystalline Ropes of Metallic Carbon Nanotubes," *Science (80-.)*, vol. 273, no. 5274, pp. 483–487, Jul. 1996.
- [117] R. Martel, T. Schmidt, H. R. Shea, T. Hertel, and P. Avouris, "Single- and multi-wall carbon nanotube field-effect transistors," *Appl. Phys. Lett.*, vol. 73, no. 17, p. 2447, Oct. 1998.
- [118] M. Freitag, M. Radosavljevic, Y. Zhou, A. T. Johnson, and W. F. Smith, "Controlled creation of a carbon nanotube diode by a scanned gate," *Appl. Phys. Lett.*, vol. 79, no. 20, p. 3326, Nov. 2001.
- [119] V. Derycke, R. Martel, J. Appenzeller, and P. Avouris, "Controlling doping and carrier injection in carbon nanotube transistors," *Appl. Phys. Lett.*, vol. 80, no. 15, p. 2773, Apr. 2002.
- [120] R. Martel, V. Derycke, C. Lavoie, J. Appenzeller, K. Chan, J. Tersoff, and P. Avouris, "Ambipolar Electrical Transport in Semiconducting Single-Wall Carbon Nanotubes," *Phys. Rev. Lett.*, vol. 87, no. 25, p. 256805, Dec. 2001.
- [121] J. Kong, "Nanotube Molecular Wires as Chemical Sensors," *Science (80-.)*, vol. 287, no. 5453, pp. 622–625, Jan. 2000.
- [122] P. G. Collins, "Extreme Oxygen Sensitivity of Electronic Properties of Carbon Nanotubes," *Science (80-.)*, vol. 287, no. 5459, pp. 1801–1804, Mar. 2000.
- [123] M. Shim, N. W. Shi Kam, R. J. Chen, Y. Li, and H. Dai, "Functionalization of Carbon Nanotubes for Biocompatibility and Biomolecular Recognition," *Nano Lett.*, vol. 2, no. 4, pp. 285–288, Apr. 2002.
- [124] "Schottky_barrier." [Online]. Available: http://en.wikipedia.org/wiki/File:Schottky_barrier_zero_bias.svg.
- [125] B. L. Allen, P. D. Kichambare, and A. Star, "Carbon Nanotube Field-Effect-Transistor-Based Biosensors," *Adv. Mater.*, vol. 19, no. 11, pp. 1439–1451, Jun. 2007.

- [126] R. J. Chen, S. Bangsaruntip, K. A. Drouvalakis, N. W. S. Kam, M. Shim, Y. Li, W. Kim, P. J. Utz, and H. Dai, "Noncovalent functionalization of carbon nanotubes for highly specific electronic biosensors.," *Proc. Natl. Acad. Sci. U. S. A.*, vol. 100, no. 9, pp. 4984–9, Apr. 2003.
- [127] A. Star, J.-C. P. Gabriel, K. Bradley, and G. Grüner, "Electronic Detection of Specific Protein Binding Using Nanotube FET Devices," *Nano Lett.*, vol. 3, no. 4, pp. 459–463, Apr. 2003.
- [128] R. J. Chen, H. C. Choi, S. Bangsaruntip, E. Yenilmez, X. Tang, Q. Wang, Y.-L. Chang, and H. Dai, "An investigation of the mechanisms of electronic sensing of protein adsorption on carbon nanotube devices.," *J. Am. Chem. Soc.*, vol. 126, no. 5, pp. 1563–8, Feb. 2004.
- [129] H. R. Byon and H. C. Choi, "Network single-walled carbon nanotube-field effect transistors (SWNT-FETs) with increased Schottky contact area for highly sensitive biosensor applications.," *J. Am. Chem. Soc.*, vol. 128, no. 7, pp. 2188–9, Feb. 2006.
- [130] X. Tang, S. Bansaruntip, N. Nakayama, E. Yenilmez, Y.-L. Chang, and Q. Wang, "Carbon nanotube DNA sensor and sensing mechanism.," *Nano Lett.*, vol. 6, no. 8, pp. 1632–6, Aug. 2006.
- [131] E. L. Gui, L.-J. Li, K. Zhang, Y. Xu, X. Dong, X. Ho, P. S. Lee, J. Kasim, Z. X. Shen, J. A. Rogers, and S. G. Mhaisalkar, "DNA sensing by field-effect transistors based on networks of carbon nanotubes.," *J. Am. Chem. Soc.*, vol. 129, no. 46, pp. 14427–32, Nov. 2007.
- [132] I. Heller, A. M. Janssens, J. Männik, E. D. Minot, S. G. Lemay, and C. Dekker, "Identifying the mechanism of biosensing with carbon nanotube transistors.," *Nano Lett.*, vol. 8, no. 2, pp. 591–5, Feb. 2008.
- [133] E. Stern, R. Wagner, F. J. Sigworth, R. Breaker, T. M. Fahmy, and M. A. Reed, "Importance of the Debye screening length on nanowire field effect transistor sensors.," *Nano Lett.*, vol. 7, no. 11, pp. 3405–9, Nov. 2007.
- [134] S. Sorgenfrei, C.-Y. Chiu, M. Johnston, C. Nuckolls, and K. L. Shepard, "Debye screening in single-molecule carbon nanotube field-effect sensors.," *Nano Lett.*, vol. 11, no. 9, pp. 3739–43, Sep. 2011.
- [135] F. Patolsky, G. Zheng, and C. M. Lieber, "Nanowire-Based Biosensors," *Anal. Chem.*, vol. 78, no. 13, pp. 4260–4269, Jul. 2006.
- [136] F. Patolsky, G. Zheng, and C. M. Lieber, "Fabrication of silicon nanowire devices for ultrasensitive, label-free, real-time detection of biological and chemical species.," *Nat. Protoc.*, vol. 1, no. 4, pp. 1711–24, Jan. 2006.

- [137] R. B. M. Schasfoort, P. Bergveld, R. P. H. Kooyman, and J. Greve, "Possibilities and limitations of direct detection of protein charges by means of an immunological field-effect transistor," *Anal. Chim. Acta*, vol. 238, pp. 323–329, 1990.
- [138] E. Steen Redeker, D. T. Ta, D. Cortens, B. Billen, W. J. Guedens, and P. Adriaensens, "Protein Engineering For Directed Immobilization.," *Bioconjug. Chem.*, vol. 24, no. 11, pp. 1761–1777, Oct. 2013.
- [139] F. Rusmini, Z. Zhong, and J. Feijen, "Protein immobilization strategies for protein biochips.," *Biomacromolecules*, vol. 8, no. 6, pp. 1775–89, Jun. 2007.
- [140] "IgG," 2011. [Online]. Available: http://upload.wikimedia.org/wikipedia/commons/thumb/1/19/Immunoglobulin_basic_unit.svg/1000px-Immunoglobulin_basic_unit.svg.png.
- [141] L. Hu, D. S. Hecht, and G. Grüner, "Carbon nanotube thin films: fabrication, properties, and applications.," *Chem. Rev.*, vol. 110, no. 10, pp. 5790–844, Oct. 2010.
- [142] M. Yu, H. H. Funke, J. L. Falconer, and R. D. Noble, "High density, vertically-aligned carbon nanotube membranes.," *Nano Lett.*, vol. 9, no. 1, pp. 225–9, Jan. 2009.
- [143] A. C. Ferrari, V. Skákalová, P.-W. Chiu, A. Bachtold, D. Golberg, A. B. Kaiser, and S. Roth, "Modelling conduction in carbon nanotube networks with different thickness, chemical treatment and irradiation," *Phys. E Low-dimensional Syst. Nanostructures*, vol. 40, no. 7, pp. 2311–2318, 2008.
- [144] E. Bekyarova, M. E. Itkis, N. Cabrera, B. Zhao, A. Yu, J. Gao, and R. C. Haddon, "Electronic properties of single-walled carbon nanotube networks.," *J. Am. Chem. Soc.*, vol. 127, no. 16, pp. 5990–5, Apr. 2005.
- [145] M. Kaempgen, C. K. Chan, J. Ma, Y. Cui, and G. Gruner, "Printable thin film supercapacitors using single-walled carbon nanotubes.," *Nano Lett.*, vol. 9, no. 5, pp. 1872–6, May 2009.
- [146] E. Artukovic, M. Kaempgen, D. S. Hecht, S. Roth, and G. Grüner, "Transparent and flexible carbon nanotube transistors.," *Nano Lett.*, vol. 5, no. 4, pp. 757–60, Apr. 2005.
- [147] H. E. Unalan, G. Fanchini, A. Kanwal, A. Du Pasquier, and M. Chhowalla, "Design criteria for transparent single-wall carbon nanotube thin-film transistors.," *Nano Lett.*, vol. 6, no. 4, pp. 677–82, Apr. 2006.

- [148] P. Ramesh, M. E. Itkis, J. M. Tang, and R. C. Haddon, "SWNT–MWNT Hybrid Architecture for Proton Exchange Membrane Fuel Cell Cathodes," *J. Phys. Chem. C*, vol. 112, no. 24, pp. 9089–9094, Jun. 2008.
- [149] R. K. Das, B. Liu, J. R. Reynolds, and A. G. Rinzler, "Engineered macroporosity in single-wall carbon nanotube films.," *Nano Lett.*, vol. 9, no. 2, pp. 677–83, Feb. 2009.
- [150] J. Li, L. Hu, L. Wang, Y. Zhou, G. Grüner, and T. J. Marks, "Organic light-emitting diodes having carbon nanotube anodes.," *Nano Lett.*, vol. 6, no. 11, pp. 2472–7, Nov. 2006.
- [151] G. Gruner, "Carbon nanotube films for transparent and plastic electronics," *J. Mater. Chem.*, vol. 16, no. 35, p. 3533, Sep. 2006.
- [152] V. C. Moore, M. S. Strano, E. H. Haroz, R. H. Hauge, R. E. Smalley, J. Schmidt, and Y. Talmon, "Individually Suspended Single-Walled Carbon Nanotubes in Various Surfactants," *Nano Lett.*, vol. 3, no. 10, pp. 1379–1382, Oct. 2003.
- [153] M. F. Islam, E. Rojas, D. M. Bergey, A. T. Johnson, and A. G. Yodh, "High Weight Fraction Surfactant Solubilization of Single-Wall Carbon Nanotubes in Water," *Nano Lett.*, vol. 3, no. 2, pp. 269–273, Feb. 2003.
- [154] J.-Y. Hwang, A. Nish, J. Doig, S. Douven, C.-W. Chen, L.-C. Chen, and R. J. Nicholas, "Polymer structure and solvent effects on the selective dispersion of single-walled carbon nanotubes.," *J. Am. Chem. Soc.*, vol. 130, no. 11, pp. 3543–53, Mar. 2008.
- [155] D. R. Kauffman and A. Star, "Chemically induced potential barriers at the carbon nanotube-metal nanoparticle interface.," *Nano Lett.*, vol. 7, no. 7, pp. 1863–8, Jul. 2007.
- [156] J. L. Bahr, E. T. Mickelson, M. J. Bronikowski, R. E. Smalley, and J. M. Tour, "Dissolution of small diameter single-wall carbon nanotubes in organic solvents?," *Chem. Commun.*, no. 2, pp. 193–194, Jan. 2001.
- [157] K. Fu and Y.-P. Sun, "Dispersion and solubilization of carbon nanotubes.," *J. Nanosci. Nanotechnol.*, vol. 3, no. 5, pp. 351–64, Oct. 2003.
- [158] V. Krstic, G. S. Duesberg, J. Muster, M. Burghard, and S. Roth, "Langmuir–Blodgett Films of Matrix-Diluted Single-Walled Carbon Nanotubes," *Chem. Mater.*, vol. 10, no. 9, pp. 2338–2340, Sep. 1998.
- [159] F. Liang, A. K. Sadana, A. Peera, J. Chattopadhyay, Z. Gu, R. H. Hauge, and W. E. Billups, "A Convenient Route to Functionalized Carbon Nanotubes," *Nano Lett.*, vol. 4, no. 7, pp. 1257–1260, Jul. 2004.

- [160] L. Seemann, A. Stemmer, and N. Naujoks, "Local surface charges direct the deposition of carbon nanotubes and fullerenes into nanoscale patterns.," *Nano Lett.*, vol. 7, no. 10, pp. 3007–12, Oct. 2007.
- [161] P. V Kamat, K. G. Thomas, S. Barazzouk, G. Girishkumar, K. Vinodgopal, and D. Meisel, "Self-assembled linear bundles of single wall carbon nanotubes and their alignment and deposition as a film in a dc field.," *J. Am. Chem. Soc.*, vol. 126, no. 34, pp. 10757–62, Sep. 2004.
- [162] R. Krupke, S. Linden, M. Rapp, and F. Hennrich, "Thin Films of Metallic Carbon Nanotubes Prepared by Dielectrophoresis," *Adv. Mater.*, vol. 18, no. 11, pp. 1468–1470, Jun. 2006.
- [163] B. Dan, G. C. Irvin, and M. Pasquali, "Continuous and scalable fabrication of transparent conducting carbon nanotube films.," *ACS Nano*, vol. 3, no. 4, pp. 835–43, Apr. 2009.
- [164] L. Hu, G. Gruner, J. Jenkins, and C.-J. Kim, "Flash dry deposition of nanoscale material thin films," *J. Mater. Chem.*, vol. 19, no. 32, p. 5845, Aug. 2009.
- [165] H. B. Peng, T. G. Ristorph, G. M. Schurmann, G. M. King, J. Yoon, V. Narayanamurti, and J. A. Golovchenko, "Patterned growth of single-walled carbon nanotube arrays from a vapor-deposited Fe catalyst," *Appl. Phys. Lett.*, vol. 83, no. 20, p. 4238, Nov. 2003.
- [166] X. Xu and G. R. Brandes, "A method for fabricating large-area, patterned, carbon nanotube field emitters," *Appl. Phys. Lett.*, vol. 74, no. 17, p. 2549, Apr. 1999.
- [167] C. Lim, D.-H. Min, and S.-B. Lee, "Direct patterning of carbon nanotube network devices by selective vacuum filtration," *Appl. Phys. Lett.*, vol. 91, no. 24, p. 243117, Dec. 2007.
- [168] P. Beecher, P. Servati, A. Rozhin, A. Colli, V. Scardaci, S. Pisana, T. Hasan, A. J. Flewitt, J. Robertson, G. W. Hsieh, F. M. Li, A. Nathan, A. C. Ferrari, and W. I. Milne, "Ink-jet printing of carbon nanotube thin film transistors," *J. Appl. Phys.*, vol. 102, no. 4, p. 043710, Aug. 2007.
- [169] G.-W. Hsieh, F. M. Li, P. Beecher, A. Nathan, Y. Wu, B. S. Ong, and W. I. Milne, "High performance nanocomposite thin film transistors with bilayer carbon nanotube-polythiophene active channel by ink-jet printing," *J. Appl. Phys.*, vol. 106, no. 12, p. 123706, Dec. 2009.
- [170] A. Behnam, Y. Choi, L. Noriega, Z. Wu, I. Kravchenko, A. G. Rinzler, and A. Ural, "Nanolithographic patterning of transparent, conductive single-walled carbon nanotube films by inductively coupled plasma reactive ion etching," *J. Vac. Sci. Technol. B Microelectron. Nanom. Struct.*, vol. 25, no. 2, p. 348, Feb. 2007.

- [171] J. Chae, X. Ho, J. A. Rogers, and K. Jain, "Patterning of single walled carbon nanotubes using a low-fluence excimer laser photoablation process," *Appl. Phys. Lett.*, vol. 92, no. 17, p. 173115, May 2008.
- [172] C. Bertoni, V. Skákalová, and S. Roth, "Layer-by-layer deposition of ultra-thin films of carbon nanotubes," *Phys. E Low-dimensional Syst. Nanostructures*, vol. 40, no. 7, pp. 2257–2262, May 2008.
- [173] S. W. Lee, B.-S. Kim, S. Chen, Y. Shao-Horn, and P. T. Hammond, "Layer-by-layer assembly of all carbon nanotube ultrathin films for electrochemical applications.," *J. Am. Chem. Soc.*, vol. 131, no. 2, pp. 671–9, Jan. 2009.
- [174] K. U. Lee, Y. H. Cho, M. C. Petty, and B. T. Ahn, "Electrical conductivity of single-wall carbon nanotube film deposited by electrostatic layer-by-layer assembly with the aid of polyelectrolytes," *Carbon N. Y.*, vol. 47, no. 2, pp. 475–481, Feb. 2009.
- [175] M. A. Meitl, Y. Zhou, A. Gaur, S. Jeon, M. L. Usrey, M. S. Strano, and J. A. Rogers, "Solution Casting and Transfer Printing Single-Walled Carbon Nanotube Films," *Nano Lett.*, vol. 4, no. 9, pp. 1643–1647, Sep. 2004.
- [176] J. Hone, M. C. Llaguno, N. M. Nemes, A. T. Johnson, J. E. Fischer, D. A. Walters, M. J. Casavant, J. Schmidt, and R. E. Smalley, "Electrical and thermal transport properties of magnetically aligned single wall carbon nanotube films," *Appl. Phys. Lett.*, vol. 77, no. 5, p. 666, Jul. 2000.
- [177] G. Decher, J. D. Hong, and J. Schmitt, "Buildup of ultrathin multilayer films by a self-assembly process: III. Consecutively alternating adsorption of anionic and cationic polyelectrolytes on charged surfaces," *Thin Solid Films*, vol. 210, pp. 831–835, 1992.
- [178] G. Decher, "Fuzzy Nanoassemblies: Toward Layered Polymeric Multicomposites," *Science (80-.)*, vol. 277, no. 5330, pp. 1232–1237, Aug. 1997.
- [179] G. Decher, B. Lehr, K. Lowack, Y. Lvov, and J. Schmitt, "New nanocomposite films for biosensors: layer-by-layer adsorbed films of polyelectrolytes, proteins or DNA," *Biosens. Bioelectron.*, vol. 9, no. 9, pp. 677–684, 1994.
- [180] Y. Lvov, K. Ariga, M. Onda, I. Ichinose, and T. Kunitake, "Alternate Assembly of Ordered Multilayers of SiO₂ and Other Nanoparticles and Polyions," *Langmuir*, vol. 13, no. 23, pp. 6195–6203, Nov. 1997.
- [181] Y. Lvov, K. Ariga, I. Ichinose, and T. Kunitake, "Assembly of Multicomponent Protein Films by Means of Electrostatic Layer-by-Layer Adsorption," *J. Am. Chem. Soc.*, vol. 117, no. 22, pp. 6117–6123, Jun. 1995.

- [182] S. Hirsjärvi, Y. Qiao, A. Royere, J. Bibette, and J.-P. Benoit, "Layer-by-layer surface modification of lipid nanocapsules," *Eur. J. Pharm. Biopharm.*, vol. 76, no. 2, pp. 200–207, 2010.
- [183] C. Peng, Y. S. Thio, and R. A. Gerhardt, "Effect of precursor-layer surface charge on the layer-by-layer assembly of polyelectrolyte/nanoparticle multilayers.," *Langmuir*, vol. 28, no. 1, pp. 84–91, Jan. 2012.
- [184] "PDDA." [Online]. Available:
<http://www.sigmaaldrich.com/catalog/product/aldrich/409022?lang=en®ion=US>.
- [185] "PSS." [Online]. Available:
<http://www.sigmaaldrich.com/catalog/product/aldrich/243051?lang=en®ion=US>.
- [186] W. Xue and T. Cui, "Thin-film transistors with controllable mobilities based on layer-by-layer self-assembled carbon nanotube composites," *Solid. State. Electron.*, vol. 53, no. 9, pp. 1050–1055, Sep. 2009.
- [187] T. Cui, F. Hua, and Y. Lvov, "FET Fabricated by Layer-by-Layer Nanoassembly," *IEEE Trans. Electron Devices*, vol. 51, no. 3, pp. 503–506, Mar. 2004.